

Initial steps of the Fischer-Tropsch synthesis on Fe(100): The role of hydrogen

THESIS

presented for the degree of
Doctor of Philosophy at the
University of Cape Town

by

Pieter van Helden



Centre for Catalysis Research
Department of Chemical Engineering
University of Cape Town
Private Bag
Rondebosch, 7701
South Africa

The copyright of this thesis vests in the author. No quotation from it or information derived from it is to be published without full acknowledgement of the source. The thesis is to be used for private study or non-commercial research purposes only.

Published by the University of Cape Town (UCT) in terms of the non-exclusive license granted to UCT by the author.

This thesis is approved by the promoters:

Prof. E. van Steen

Pieter van Helden

Initial steps of the Fischer-Tropsch synthesis on Fe(100):

The role of hydrogen

ISBN 978-0-620-43010-4

Keywords:

*Fischer-Tropsch / Iron / Adsorption / Hydrogen /
Coadsorption / CO dissociation*

Copyright © 2008 by Pieter van Helden

All rights reserved. No part of this book may be reproduced, in any form or by any means, without permission in writing from the author.

The work described in this thesis has been carried out at the Catalysis Research Unit, Department of Chemical Engineering, University of Cape Town, South Africa. This work is part of the Fe focus area of the 'Fischer-Tropsch molecular modelling' research project, which is financially supported by SASOL.

This document was compiled on August 21, 2009
by L^AT_EX 2_ε provided by MiK_TE_X 2.7

University of Cape Town

'Timor domini principium scientiae sapientiam'
— PROVERBS 1:7a

Contents

Synopsis	iii
List of Figures	vi
List of Tables	x
1 General Introduction	1
1.1 Fischer-Tropsch Synthesis	1
1.2 Aim of this study	8
1.3 Outline of thesis	9
Bibliography	10
2 Method and model verification	13
2.1 Introduction	13
2.2 Computational chemistry methods	13
2.3 General computational method	20
2.4 Bulk iron model verification	20
2.5 Conclusions	27
Bibliography	27
3 Hydrogen and CO adsorption models	31
3.1 Introduction	31
3.2 Computational method	34
3.3 Results and discussion	35
3.4 Equilibrium surface coverage	38
3.5 Conclusions	48
Bibliography	48
4 Hydrogen dissociation on precovered surfaces	51
4.1 Introduction	51
4.2 Methods and models	53
4.3 Results	55
4.4 Discussion	65

4.5	Conclusions	68
	Bibliography	69
5	Coadsorption of CO and H on Fe(100)	71
5.1	Introduction	71
5.2	Method and models	72
5.3	Results and discussion	75
5.4	Conclusions	90
	Bibliography	90
6	Hydrogen assisted CO dissociation	93
6.1	Introduction	93
6.2	Computational method	95
6.3	Results	95
6.4	Discussion	98
6.5	Conclusions	102
	Bibliography	103
7	General Conclusions	105
A	Glossary	109
B	Derivation of CO adsorption equilibrium conditions	113
B.1	Gas phase description	113
B.2	Adsorbed phase description	114
C	Localised Thermodynamics	119
D	Intermediates for CO hydrogenation on Fe(100)	123
D.1	Introduction	123
D.2	Method and models	123
D.3	Results	125
D.4	Pathways for CO hydrogenation	128
D.5	Conclusions	132
	Bibliography	133
	List of Publications	134
	Acknowledgements	137
	Curriculum Vitae	139

Synopsis

IN this thesis the role of hydrogen in the initial steps of the Fischer-Tropsch reaction on the model Fe(100) surface is explored. The Fischer-Tropsch reaction is a industrially applied catalytic process in which synthesis gas (H_2 and CO produced from coal or natural gas) is converted to a wide range of long chain hydrocarbons. Although various microscopic mechanisms have been proposed, the fundamental role of hydrogen in the initialisation steps of these reaction mechanisms is still uncertain.

This study aims to address a number of key questions with regard to the role of hydrogen in the initiation of this reaction. The addressed topics include various aspects regarding the adsorption of both H_2 and CO gases, as well as considerations with regard to their respective dissociation reactions.

Firstly the employed theoretical methods are discussed, after which the model setup and verifications are illustrated (Chapter 2). Density functional theory (DFT) was employed to do the quantum chemical calculations described in this thesis. To be able to obtain useful knowledge from these calculations, a model was set up for the Fe(100) surface by starting with an extensive bulk α -iron model and surface verification study.

The resulting RPBE surface model was employed in the following chapter to describe the separate adsorption of hydrogen and CO on the Fe(100) surface. After calculating the structures and energies for range of coverages for both H and CO, we applied these values in statistical thermodynamic models for the adsorption equilibria. This enables an analysis of these equilibria at relevant Fischer-Tropsch conditions ($500 \text{ K} < T < 650 \text{ K}$ and $P > 1 \text{ bar}$). The resulting models were used to consider the equilibrium surface coverage of hydrogen at a range of temperatures and pressures. From these models it is concluded that there will be a strong driving force to fill up the whole Fe(100) surface with hydrogen at Fischer-Tropsch conditions, which corresponds to a hydrogen saturation coverage of around $\theta_H = 1.00 \text{ ML}$. Using a similar statistical thermodynamic model for the equilibrium surface coverage of CO it is shown that at Fischer-Tropsch conditions the CO adsorption equilibrium is shifted towards saturation coverage, which lies between 0.5 and 0.65 ML. This saturation coverage of CO is lower than that of hydrogen. Therefore we expect that, upon the adsorption

of CO on Fe(100), almost half of the hollow sites will still be open at Fischer-Tropsch conditions.

We proceeded to study the dissociation process of H₂ on the Fe(100) surface (Chapter 4). The dissociation of H₂ was considered on a clean Fe(100) surface, as well as on CO and C precovered Fe(100) surfaces. The presence of CO and C will block several sites for hydrogen adsorption. At the same time it will increase the various hydrogen dissociation barriers. At CO and C coverages of up to 0.25 ML the main contributors to the barrier increases are the CO-H and C-H repulsions. The proposed *off-symmetry* sites will play an important role to dissociate the approaching hydrogen molecules in these cases. At higher coverages of 0.5 ML of CO and C we show that the dissociation barriers increased to at least three times larger values than that of the clean surface. At these coverages adsorption site blockage will also occur. We show that the increase of the dissociation barriers is mainly due to the change in the local electronic environment. This can be seen in a relation between the change in the system's Fermi level and the increase in the dissociation barriers. These very large increases in the dissociation barriers would result in a significant decrease in the rate constant of the dissociative adsorption process. With an already low pre-exponential factor this process becomes a very slow reaction step and can, in the case of a very highly CO or C covered Fe(100) surface, be rate determining.

The model Fe(100) surface was also used to study the coadsorption of CO and hydrogen (Chapter 5). Various coverages of CO and hydrogen were considered with resulting H:CO surface ratios ranging from 0.25 to 4. Electrostatic repulsive interactions were shown to exist between the adsorbed CO and H, as well as an electronic interaction between the adsorbed CO and H orbitals. This electronic interaction can have a stabilising effect on the coadsorbed geometry. A number of of the considered geometries at both $\theta_{CO} = 0.25$ ML and $\theta_{CO} = 0.5$ ML are stable in a mixed coadsorbed state as opposed to alternative of island formation. This is due to the relative instability of the corresponding compressed H and, in particular, CO islands. At the relevant Fischer-Tropsch temperatures H and undissociated CO will be in a mixed coadsorbed state on the surface. For these mixed states the optimal surface H:CO ratios for $\theta_{CO} = 0.5$ ML and $\theta_{CO} = 0.25$ ML are 1 and 3, respectively.

Once H and CO are coadsorbed, they might react with each other. We calculated the addition of H to CO to form 'HCO' and 'COH' species and show that, although both are endothermic reactions, these species are stable with regard to the gas phase. The 'HCO' species is the most stable of the two and it can dissociate to form coadsorbed CH and O. In Chapter 6 this H assisted CO dissociation reaction was compared to the normal direct CO dissociation. We found that the H assisted CO dissociation can play

an important role in creating the Fischer-Tropsch surface species. The direct CO dissociation mechanism will be the major contributor to the effective CO scission rate at low initial H and CO coverages. If the H coverage increases the H assisted mechanism will become more prominent. Both these mechanisms will contribute significantly to the CO scission rate at $\theta_{CO} = 0.5$ ML. The dominant CO scission mechanism depends strongly on the initial H coverage. It is proposed that H assisted CO dissociation is a possible CO scission pathway on Fe(100). At Fischer-Tropsch temperatures the scission of CO on the Fe(100) surface will probably take place via a combination of the direct CO dissociation and the H assisted CO dissociation mechanisms to produce a combination of C, CH and O surface species. We therefore show that CO dissociation can take place on the Fe(100) surface under Fischer-Tropsch conditions, irrespective of the H concentration.

The results presented in this thesis seem to broadly favour the mechanisms for Fischer-Tropsch in which CO first needs to dissociate to be able to form the chain growth initiators and monomers. We conclude by pointing out that despite some limitations of this model, we have made a step towards understanding the role that H plays in the initiation of the Fischer-Tropsch reaction.

List of Figures

1.1	Representation of the 'alkyl' mechanism.	4
1.2	Representation of the 'alkenyl' mechanism.	4
1.3	Representation of the 'CO-insertion' mechanism.	4
1.4	Representation of the 'enol' mechanism.	4
1.5	The configurations of the three low index iron surfaces.	7
2.1	Flow charts of the SCF cycle and the geometrical optimization cycle used to calculate energies and structures with DFT.	18
2.2	Potential energy surface indicating the effect of k-point meshes and cut-off energies.	22
2.3	The effect of Fe(110) surface creation on the surface energy and magnetic moment using PW91.	28
2.4	Surface energies of Fe(110), Fe(100) and Fe(111) as a function of the slab thickness.	28
3.1	Bonding of CO to typical iron atom orbitals and the accompanying change in the DOS.	33
3.2	A comparison of the calculated RPBE CO adsorption energies with the PW91 literature values.	37
3.3	Interpolation of the calculated atomic binding energies of hydrogen on Fe(100) by using various fitting functions.	39
3.4	The predicted hydrogen equilibrium surface coverage as a function of temperature using combinations of interpolation fits and models.	42
3.5	Interpolation of the calculated molecular binding energies of CO on Fe(100) by using various fitting functions.	45
3.6	The predicted equilibrium CO surface coverage as a function of the temperature using the proposed interpolation fits.	46
4.1	PES for H ₂ dissociation on a clean Fe(100) surface with H ₂ on top, on top rotated by 45° and on the bridge site.	59

4.2	PES for H ₂ dissociation on a $\theta_{CO} = 0.25$ ML precovered Fe(100) surface with H ₂ adsorption on top and on top rotated by 45°	59
4.3	PES for H ₂ dissociation on a $\theta_{CO} = 0.25$ ML precovered Fe(100) surface with H ₂ rotated by 45°. The H ₂ centre of mass is slightly moved away from the high symmetry on top site.	59
4.4	PES for H ₂ dissociation on a $\theta_{CO} = 0.5$ ML precovered Fe(100) surface with H ₂ on top and on top rotated by 45°	60
4.5	PES for H ₂ dissociation on a $\theta_C = 0.25$ ML precovered Fe(100) surface with H ₂ on top and rotated by 45°	61
4.6	PES for H ₂ dissociation on a $\theta_C = 0.25$ ML precovered Fe(100) surface with H ₂ rotated by 45°. The H ₂ centre of mass is slightly moved away from the high symmetry on top site.	62
4.7	PES for H ₂ dissociation on a $\theta_{CO} = 0.5$ ML precovered Fe(100) surface with H ₂ on top and on top rotated by 45°	63
4.8	Spin resolved DOS plots of the d-bands of the surface Fe atoms for clean and precovered Fe(100) surfaces.	66
4.9	The H ₂ dissociation barriers on the on top rotated by 45° site as a function of the change in the Fermi level.	66
5.1	Top view of the coadsorption geometries on Fe(100) with $\theta_{CO} = 1$ ML. . .	77
5.2	Top view of the coadsorption geometries on Fe(100) with $\theta_{CO} = 0.5$ ML. .	78
5.3	Top view of the coadsorption geometries on Fe(100) with $\theta_{CO} = 0.25$ ML with H in four-fold hollow sites.	81
5.4	Top view of the coadsorption geometries on Fe(100) with $\theta_{CO} = 0.25$ ML with H on other sites.	81
5.5	LDOS of the orbitals of CO in purely adsorbed CO and in the coadsorption geometries of 4-A, 4-B and 4-G.	85
5.6	LDOS of the orbitals of H in purely adsorbed H and in the coadsorption geometries of 4-A, 4-B and 4-G.	86
5.7	LDOS of the orbitals of CO and H in purely adsorbed CO and in coadsorption geometry 4-I.	86
5.8	Trends in the free energy of the surface mixing process for coadsorption at $\theta_{CO} = 0.5$ ML and $\theta_{CO} = 0.25$ ML.	89
6.1	Direct CO dissociation pathway on Fe(100) at $\theta_{CO} = 0.25$ ML including the <i>cis</i> and <i>trans</i> product structures.	94
6.2	Structures of the 'COH' and 'HCO' species at $\theta = 0.25$ ML.	97
6.3	H assisted CO dissociation pathway on Fe(100) at $\theta_{CO} = 0.25$ ML	99

6.4	Comparison of the PES of the zero-point corrected direct CO dissociation and the 'HCO' dissociation pathways at $\theta_{CO} = 0.25$ ML.	99
6.5	Percentage contribution of the 'HCO' dissociation mechanism to the total CO scission rate at 300°C with an initial $\theta_{CO} = 0.25$ ML.	101
6.6	Percentage contribution of the 'HCO' dissociation mechanism to the total CO scission rate at 300°C with an initial $\theta_{CO} = 0.5$ ML.	102
D.1	Formation energies for species formed by sequential addition of H.	126
D.2	Comparison of structure <i>G</i> at $\theta_{CO} = 0.25$ ML and $\theta_{CO} = 0.5$ ML.	126
D.3	Top and side views of the structure of <i>C</i> at $\theta_{CO} = 0.5$ ML.	126
D.4	The structure of the adsorbed methoxy group at an initial $\theta_{CO} = 0.5$ ML.	127
D.5	Comparison of the energy values of intermediates in the 'alkyl' mechanism for CH_4 formation at an initial $\theta_{CO} = 0.25$ ML in the present work to literature values.	129
D.6	Energy values of the intermediates in the CH_3OH formation pathway.	130
D.7	Comparison of the lowest energy direct hydrogenation pathways at an initial $\theta_{CO} = 0.25$ ML and $\theta_{CO} = 0.5$ ML.	131
D.8	Comparison of the direct CO dissociation pathway to the lowest energy direct hydrogenation pathways at an initial $\theta_{CO} = 0.25$ ML.	131

List of Tables

1.1	Comparison of the calculated CO dissociation energies for the three low miller index Fe surfaces.	7
2.1	Chronological summary of the calculated properties of bulk α -Fe.	24
2.2	Variation of the calculated bulk characteristics with different pseudopotentials.	25
2.3	Summary of the optimised cutoff energies, k-meshes and surface energies for Fe surfaces.	28
3.1	Calculated adsorption energies of H on Fe(100).	37
3.2	Calculated adsorption energies of CO on Fe(100).	37
3.3	Summary of function fitting parameters for the interpolation of H adsorption energies.	39
3.4	Summary of function fitting parameters for the interpolation of CO adsorption energies.	45
4.1	Summary of the calculated barriers for H ₂ dissociation on clean and pre-covered Fe(100).	64
4.2	Calculated charges and Fermi level energies for the clean and precovered Fe(100) surfaces.	66
5.1	Calculated coadsorption energies, heats of mixing, CO bond lengths and angles for the considered coadsorption geometries on the Fe(100) surface at different initial CO coverages.	82
5.2	Mulliken Charges at $\theta_{CO} = 0.25$ ML	83
5.3	Vibrational frequencies and zero-point vibrational energies (ZPVE) of a selected number of geometries.	88

University of Cape Town

Chapter 1

General Introduction

The last thing one knows in constructing a work is what to put first.

— BLAISE PASCAL

1.1 Fischer-Tropsch Synthesis

IN the 1920's two chemists at the Kaiser Wilhelm Institute for Coal Research in Germany, Franz Fischer and Hans Tropsch, patented a chemical synthesis reaction in which hydrocarbons were obtained from a reaction between hydrogen and carbon monoxide over a metal catalyst. This reaction, which is now called the Fischer-Tropsch (FT) synthesis, has become quite prominent in recent times. This is due to the fact that it provides a route to the production of hydrocarbon fuel from a feedstock other than crude oil. Its renewed popularity is largely driven by the limited reserves of crude oil and the accompanying high oil prices, as well as some environmental demands [1]. The possibilities of this technology can be seen in the fact that it can be used to convert the large reserves of coal and natural gas to higher value hydrocarbons. These are respectively known as coal-to-liquids (CTL) and gas-to-liquids (GTL) technologies [2]. This technology may become quite useful in countries with large coal reserves, like China and the USA.

Currently, the Fischer-Tropsch synthesis reaction industrially applied by SASOL and PetroSA in South Africa (CTL and GTL), Shell in Malaysia and the new Oryx GTL plant in Qatar. These companies use the Fischer-Tropsch synthesis to obtain a very wide spectrum of hydrocarbons through the reaction between hydrogen and carbon monoxide (synthesis gas) which is obtained from gasifying coal or reforming natural gas [2, 3]. This reaction takes place over a metal based Fischer-Tropsch catalyst. Water and carbon dioxide are produced as by-products.

The metal catalysts that are able to perform the Fischer-Tropsch synthesis reaction are based on Ni, Ru, Co and Fe. Of these metals, Fe and Co based catalysts are applied industrially (and have attracted quite a lot of research attention).

1.1.1 Fischer-Tropsch Mechanisms

We can regard the Fischer-Tropsch reaction as a type of polymerization reaction. A reaction of this type can be divided into three important sections:

1. Initiation
2. Chain growth
3. Termination

In the first section of the Fischer-Tropsch reaction (initiation) the adsorption of synthesis gas (hydrogen and carbon monoxide) is responsible for the formation of precursor surface species. Various precursor surface species, ranging from atomic species to elaborate surfaces complexes, have been proposed. These surface species can react to form the monomers and chain initiators which are required to start and maintain the Fischer-Tropsch polymerization reaction. In the second section (chain growth) the specific surface monomers polymerise to form the long hydrocarbon chains. The third section (termination) is comprised of the termination of a hydrocarbon chain to form an adsorbed product. This product can subsequently desorb from the surface.

Over the 80 years of its history, the microscopic details of the mechanisms of these steps in the Fischer-Tropsch synthesis has been an issue of some controversy. A number of possible mechanisms has been proposed for this reaction. The 'alkyl', the 'alkenyl', the 'CO-insertion' and the 'enol' mechanisms are the four most prominent proposed mechanisms.

1.1.1.1 The 'Alkyl' mechanism

The 'alkyl' mechanism has its roots in the 'carbide' mechanism which was the first proposed Fischer-Tropsch mechanism [4, 5]. The 'alkyl' mechanism found favour after experimental work done by Van Barneveld and Ponc [6, 7], and Brady and Petit [8, 9], and at present it is a widely accepted mechanism [10]. In this mechanism, illustrated in Figure 1.1, the surface carbon and hydrogen species are generated via dissociative adsorption of CO and H₂. The oxygen atoms are somehow removed by hydrogen to form water. This water formation process is obviously a multi-step reaction involving the hydrogenation of the O atoms. The surface carbon is sequentially hydrogenated

to form surface-CH, -CH₂ and -CH₃ species. The surface-CH₃ is regarded as the chain growth initiator. Taking surface-CH₂ as the monomer, a polymerization reaction takes place in which the -CH₂ species are inserted into the hydrocarbon chain. The formation of a hydrocarbon product from a polymer chain takes place either via β -hydrogen abstraction to yield an α -olefin or via hydrogenation that would produce a n-paraffin. It has also been postulated that the cleaving of the surface-chain bond by a surface-OH species could lead to the formation of alcohols [10]. This mechanism assumes the scission of the CO bond. It is not mentioned if this would take place via a direct dissociation of the CO bond or if the scission of the CO bond takes place after an initial hydrogenation of the adsorbed CO. Another factor which is relatively unclear, is where the hydrogen, which is responsible for the hydrogenation steps, are located. It seems as if this mechanism assumes that hydrogen atoms are freely available on the surface.

1.1.1.2 The 'Alkenyl' mechanism

The 'alkenyl' mechanism (Figure 1.2) [11, 12] is similar to the 'alkyl' mechanism in the initiation step, since CH and CH₂ species are formed. The difference is that, according to this mechanism, the chain initiator is a vinyl species (-CH=CH₂). The chain growth in this reaction proceeds by the insertion of a methylene (CH₂) and the subsequent isomerisation to give rise to a longer alkenyl species. The termination takes place through the addition of a hydrogen atom to result in an α -olefin. This mechanism lacks the ability to fully describe the Fischer-Tropsch products, since it does not explain paraffin and alcohol formation. Similar to the 'alkyl' mechanism the initiation steps include the scission of the CO bond and water formation. The origin and availability of the hydrogen is once again not clearly defined.

1.1.1.3 The 'CO-insertion' mechanism

The 'CO-insertion' mechanism [13–15] is in some steps very similar to the well known CO-insertion (alkyl migration) step found in homogeneous organometallic catalysis mechanisms [16]. This mechanism can be seen in Figure 1.3. In this mechanism the monomer is molecularly adsorbed CO. The chain initiator is obtained by the hydrogenation of a CO molecule to form a methyl (CH₃) species. Chain growth proceeds via insertion of a CO molecule into the alkyl chain. The subsequent elimination of the O atom by hydrogen results in a longer surface alkyl chain. The termination of the chain growth can follow various pathways resulting in either olefins and paraffins, or aldehydes and alcohols, depending on the level of the hydrogenation of the inserted

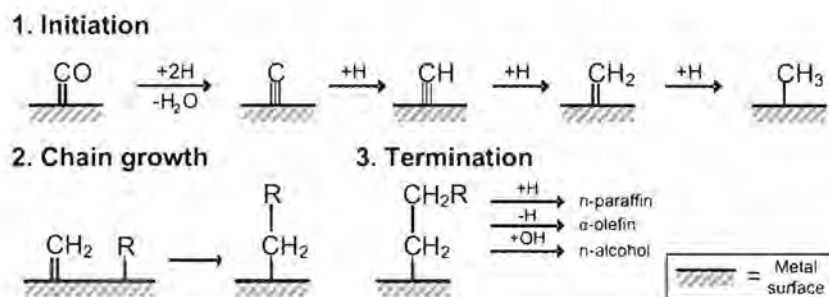


Figure 1.1: Representation of the 'alkyl' mechanism. Adapted from ref. [10]

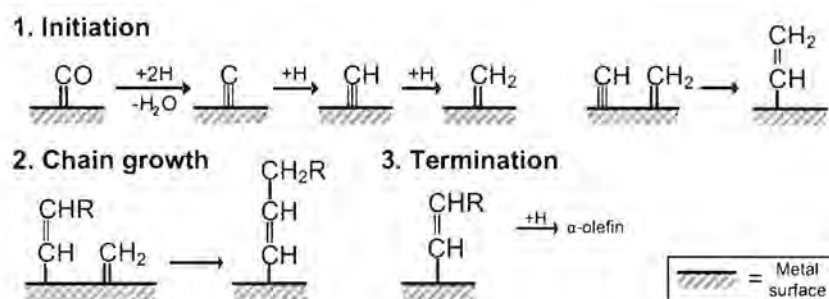


Figure 1.2: Representation of the 'alkenyl' mechanism. Adapted from ref. [10]

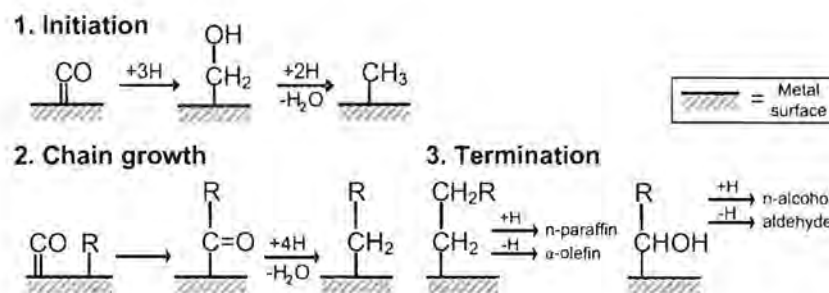


Figure 1.3: Representation of the 'CO-insertion' mechanism. Adapted from ref. [10]

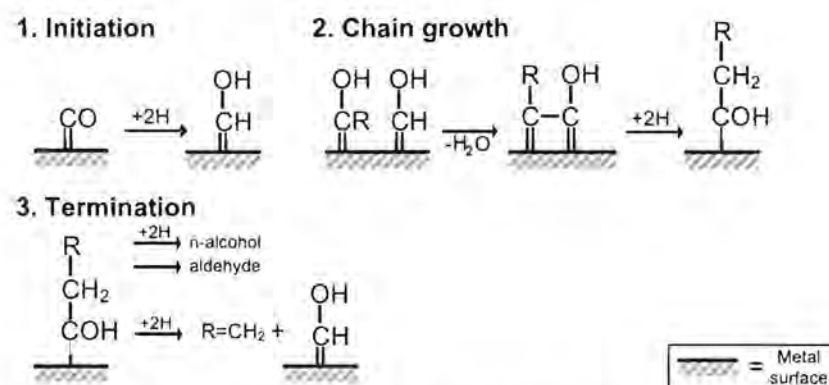


Figure 1.4: Representation of the 'enol' mechanism. Adapted from ref. [10]

CO. In this mechanism it is assumed that scission of the CO bond does not take place until the adsorbed CO molecule is partially hydrogenated. As with the previous two mechanisms the origin and availability of the hydrogen is not clearly defined.

1.1.1.4 The 'Enol' mechanism

The 'enol' mechanism can be seen in Figure 1.4. This mechanism is proposed to involve a relatively large 'enol' surface species [17]. Adsorbed CO is partially hydrogenated to form an 'enol' species which is the supposed chain initiator and monomer. The chain grows via an enol-condensation reaction and the subsequent hydrogenation to form a surface species in the form of -CHROH . Termination can once again proceed along various pathways to yield oxygenate products, as well as α -olefins. In this mechanism the CO bond stays intact until the chain growth step. The formation of these large 'enol' surface species requires a number of hydrogenation steps which are once again lumped together. Once again the origin and availability of the hydrogen atoms that are involved in these steps are not clearly defined.

1.1.2 Mechanistic considerations

When we consider all of the above mechanisms it is clear that they have a number of aspects in common. Firstly, it is clear that in these mechanisms the chain growth takes place by a step-wise procedure and the termination largely seems to determine the chemical nature of the final product. Another important similarity can be seen when we compare the initiation steps. If we consider the initiation reaction in these four mechanisms (Figures 1.1 – 1.4), it is clear that these cannot simply be one or two step reactions. These initiation steps will contain a number of fundamental surface and gas-surface reactions, which directly involve hydrogen. These fundamental steps include the adsorption of CO and hydrogen gases, hydrogen dissociation, as well as the possibility of reactions like CO dissociation or hydrogen assisted CO dissociation, water formation and multi-step partial CO hydrogenation. In the initiation steps a certain level of initial hydrogenation of either the surface carbon or the adsorbed CO molecule can be seen. The exact mechanism of these steps are not explicitly mentioned in these mechanisms. The first two mechanisms require that the CO bond be split. It is not stated if this happens by a direct dissociation of CO or by a step which includes a partially hydrogenated CO. The following two mechanisms assume that the CO bond stays intact. To be able to discern between the intact CO type and the split CO type mechanisms, it is necessary to understand the interactions between the adsorbed hydrogen and CO. Another similarity between the four discussed mechanisms is that

distinct surface effects are neglected. These include the effects of the surface geometry, structured adsorbate overlayers, as well as coadsorption effects.

In the general representation of these mechanisms the surface hydrogen is assumed to be freely available and independent of the other adsorbed species. The hydrogen atoms cannot be completely independent and the initial interaction of these hydrogen atoms with the other adsorbed species, such as CO, are therefore very important. This is particularly the case in the initiation steps of all of these proposed reaction mechanisms. These initiation steps include the coadsorption of CO and hydrogen gases. Furthermore, the possibility of reactions like hydrogen assisted CO dissociation, water formation and multi-step partial CO hydrogenation also involve the interactions between adsorbed CO and hydrogen. It is these initial fundamental reaction steps, involving hydrogen, that draws our particular interest in this thesis.

These fundamental surface reaction mechanisms can be studied in two general ways. The first is by surface science experiments. For this one usually needs high quality single crystals and ultra high vacuum conditions. The second method is to study the fundamental surface reactions by first principle theoretical methods (calculational chemistry). By utilizing these theoretical calculations we can develop models that describe catalyst surfaces. These model catalyst surfaces can be used to directly study the Fischer-Tropsch mechanism at a molecular level by calculating the surface reaction intermediates and the subsequent transition states for the fundamental reactions.

1.1.3 Iron Surfaces and Catalysis

In this thesis we are particularly interested in iron Fischer-Tropsch catalysts and therefore there will be numerous references to iron surfaces. This term (Fe surfaces) would be considered as the collective for the three low index bcc Fe surfaces Fe(100), Fe(110) and Fe(111). The geometries of these three surface configurations are illustrated in Figure 1.5. Fe(110) is the most dense Fe surface configuration, while Fe(111) is the least dense of the three surfaces. Both the Fe(110) and Fe(100) surfaces are available in relative abundance on small Fe nanocrystals [18]. The Fe(100) is a slightly more open surface than the Fe(110), which is generally regarded as being more reactive for certain types of reactions. This has been shown to be the case for the direct CO dissociation reaction (which is an important step in the 'alkyl' and 'alkenyl' mechanisms). The Fe(100) surface has the lowest calculated CO dissociation transition state energy barrier of these three low miller index Fe surfaces (see Table 1.1). Therefore the Fe(100) surface stands out as a typical model surface for studying the effects of hydrogen on

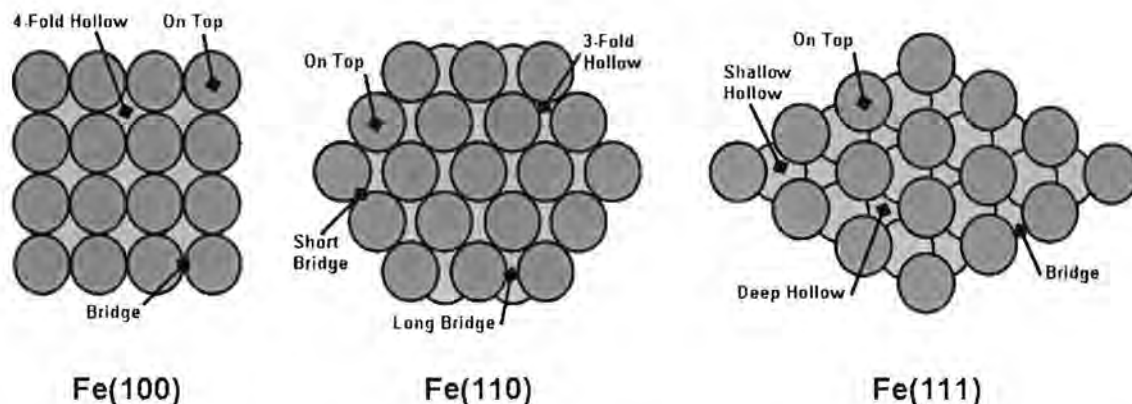


Figure 1.5: The configurations of the three low index iron surfaces. The dark circles represent the top layer of iron atoms and the lighter circles the first subsurface layers.

Table 1.1: Comparison of the calculated CO dissociation energies ($E_a^{CO_{diss}}$) in eV for the three low miller index Fe surfaces.

Surface	$E_a^{CO_{diss}}$	Functional	Ref.
Fe(110)	1.52	PBE	[21]
	1.83	RPBE	[21]
	1.77	PKZP	[21]
	1.52	PW91	[22]
Fe(100)	1.06	PW91	[23]
	1.11	PW91	[24]
	1.28	RPBE	Present work
Fe(111)	1.73	RPBE	[25]

CO in the Fischer-Tropsch synthesis. We will use this Fe(100) surface as our model catalyst surface to study some particular aspects of the role of hydrogen in the initiation steps of the Fischer-Tropsch reaction.

On this model surface we can now study various catalytic reaction steps. Catalytic surface reactions mostly take place via the Langmuir-Hinshelwood mechanism in which the surface species have energetically equilibrated with the surface. These equilibrated surface species can interact and react with each other whilst on the catalyst surface. Another class of surface reactions are the Eley-Rideal type reactions. These reactions involve the formation of an adsorbed product molecule on the surface by a reactant species from the gas phase. This might produce new surface species that can desorb or react further [19, 20]. In this work the reactions of hydrogen, via both of these types of catalytic surface reactions, will be considered.

1.2 Aim of this study

ἀνάγκη πρὸς τὴν ἐπιζητούμενην ἐπιστήμην ἐπελθεῖν ἡμᾶς πρῶτον
περὶ ὧν ἀπορήσαι δεῖ πρῶτον

— ARISTOTLE – METAPHYSICS B, i ¹

The literature on the Fischer-Tropsch synthesis is quite vast [26]. The selected introductory review presented here shows that there are still some areas in which the fundamental understanding of these processes are lacking. This is particularly clear from the initiation steps of the mentioned mechanisms in which freely available adsorbed hydrogen atoms are assumed.

Thus, the basic fundamental question we want to address is: *What is the specific role of hydrogen in Fischer-Tropsch initiation?* The goal of this work is therefore to proceed towards deepening our understanding of the specific role that hydrogen plays in the initial Fischer-Tropsch reaction steps. To shed some light on this broad question we proposed a number of key questions that will form the basis of this thesis:

- *How does hydrogen and CO adsorb on this model surface?*

For any surface reaction to start, we first need to get the relevant surface species on to the surface. The very first step of any catalytic reaction is usually the adsorption of the reagents. It is therefore a necessity to study the adsorption of CO and hydrogen on the model Fe(100) surface. If we want to gain understanding of the initiating reactions of the Fischer-Tropsch reaction the particular way each of these two gases adsorbs on their own is therefore of great importance.

- *Will the hydrogen adsorption process be affected by preadsorbed reactant species like CO?*

In the above mentioned mechanisms the assumption exists that atomic hydrogen is almost freely available. This implies that the process of dissociation of hydrogen on the surface must proceed with a very low activation barrier. This may be the case on a clean surface, but since CO is also present in the synthesis gas we expect adsorbed CO (and its dissociation products) to have an influence on the dissociation of H₂ on the Fe(100) surface. If the influence of these preadsorbed species are large then the mechanistic assumption of the freely available surface hydrogen cannot hold.

¹A possible translation (by Hugh Tredennick): "It is necessary, with a view to the science which we are investigating, that we first describe the questions which should first be discussed."

- *Will adsorbed hydrogen and CO be able to mix on the Fe(100) surface?*

Since CO and H₂ are both components of the Fischer-Tropsch synthesis gas we expect them to somehow be simultaneously present on the catalyst surface. This is an absolute necessity for the 'CO-insertion' and 'enol' mechanisms. It is therefore important to understand the coadsorption of hydrogen and CO on the Fe(100) surface. We expect hydrogen and CO to be able to coadsorb on this relatively open surface and we will therefore consider the coadsorption effects of these two species.

- *What influence does adsorbed hydrogen have on the dissociation of CO on this model surface?*

One of the main aims of this project is to postulate CO dissociation pathways under the influence of adsorbed hydrogen. As we have shown, certain surface species need to be present to be able to start the Fischer-Tropsch catalysis reaction. It is expected that the dissociation of CO by assistance of hydrogen could provide an alternative pathway to the formation of initiator and monomer species typical of a Fischer-Tropsch mechanisms such as the 'alkyl' mechanism [27].

- *What is the influence of the CO surface coverage on these hydrogen processes?*

The modes of CO adsorption usually differ with regard to the metal surface used. This is mainly due to the fact that the available CO adsorption modes on a surface are usually coverage dependent and that CO molecules can have strong lateral interactions. In this regard we expect that the surface coverage of the various species can influence the particular processes that we would like to consider. It is therefore of importance to include the effects of coverage in this study. We aim to consider both a high and a low CO coverage throughout the study. By considering all the relevant processes at various coverages of CO, we will be able to explore the effects that arise due to changes in the surface coverage.

1.3 Outline of thesis

This thesis is a theoretical view of aspects of the role that hydrogen plays in the initiation steps of the Fischer-Tropsch mechanism on Fe(100). It is divided into a number of chapters in which the relevant background will be discussed and the key questions will be addressed.

In this chapter we gave a brief overview of the context, aim and scope of this thesis.

In the following chapter we will discuss the general theoretical method, as well as some details on the model verification and specific analytical methods that was used.

In Chapter 3 a general discussion on the separate adsorption of hydrogen and CO is presented. We will show how the calculated adsorption energies can be used to calculate the adsorption equilibrium conditions of these two gases on the Fe(100) surface under realistic Fischer-Tropsch conditions.

Chapter 4 consists of the description and discussion of the calculated mechanisms of H₂ dissociation on a clean Fe(100) surface. This includes the effects that preadsorbed CO and C has on the H₂ adsorption mechanism, as well as a discussion on the origins thereof.

The next chapter deals with the equilibrium geometries and stabilities of H and CO when they are coadsorbed on the Fe(100) surface. This chapter includes a discussion on some of the coadsorption effects that can be expected between these two adsorbates on the surface. We will show that CO and H will be in a mixed coadsorption state, even at high CO coverages.

Since the arrival of H and CO on the surface was described in the previous chapters, Chapter 6 describes the effect adsorbed hydrogen atoms have on the CO dissociation process. In this chapter we describe the possibility of a direct hydrogenation of the CO and the subsequent mechanism of hydrogen assisted CO dissociation.

We conclude with a general discussion on the role hydrogen plays in the initial steps of the Fischer-Tropsch reaction based on the model Fe(100) surface (Chapter 7).

Bibliography

- [1] Dry, M. E. *Applied Catalysis A* **1999**, *189*, 185–190.
- [2] Steynberg, A. P. In *Fischer-Tropsch Technology*; Steynberg, A., Dry, M., Eds., Vol. 152 of *Studies in Surface Science and Catalysis*; Elsevier, 2004; pages 1–59.
- [3] Dry, M. E. In *Fischer-Tropsch Technology*; Steynberg, A., Dry, M., Eds., Vol. 152 of *Studies in Surface Science and Catalysis*; Elsevier, 2004; pages 533–600.
- [4] Fischer, F.; Tropsch, H. *Brennstoff-Chemie* **1926**, *7*, 97.
- [5] Craxford, S. R.; Rideal, E. *Brennstoff-Chemie* **1939**, *20*, 263.
- [6] Ponec, V.; Van Barneveld, W. A. *Industrial Engineering Chemistry Product Research and Development* **1979**, *18*, 268–271.
- [7] Van Barneveld, W. A. A.; Ponec, V. *Journal of Catalysis* **1984**, *88*, 382–387.
- [8] Brady III, R. C.; Pettit, R. *Journal of the American Chemical Society* **1980**, *102*, 6181–6182.
- [9] Brady III, R. C.; Pettit, R. *Journal of the American Chemical Society* **1981**, *103*, 1287–1289.

- [10] Claeys, M.; Van Steen, E. In *Fischer-Tropsch Technology*; Steynberg, A., Dry, M., Eds., Vol. 152 of *Studies in Surface Science and Catalysis*; Elsevier, 2004; pages 601–680.
- [11] Maitlis, P. M.; Long, H. C.; Quyoun, R.; Turner, M. L.; Zhi-Qiang, W. *Chemical Communications* **1996**, *1*, 1–8.
- [12] Maitlis, P. M.; Quyoun, R.; Long, H. C.; Turner, M. L. *Applied Catalysis, A: General* **1999**, *186*, 363–374.
- [13] Sternberg, A.; Wender, J. *Proceedings of the International Conference on Coordination Chemistry* **1959**, page 53.
- [14] Roginski, S. *Proceedings of the 3rd Congress on Catalysis* **1965**, page 939.
- [15] Pichler, H.; Schulz, H. *Chemie Ingenieur Technik* **1970**, *42*, 1162–1174.
- [16] Miessler, G. L.; Tarr, D. A. *Inorganic chemistry*; Prentice-Hall, Inc., 2 ed., 1999.
- [17] Storch, H. H.; Golubic, N.; Anderson, R. B. *The Fischer-Tropsch and Related Synthesis*; John Wiley & Sons: New York, 1951.
- [18] Błoński, P.; Kiejna, A. *Surface Science* **2007**, *601*, 123–133.
- [19] Clark, A. *The theory of adsorption and catalysis*, Vol. 18 of *Physical Chemistry: A series of Monographs*; Academic Press: New York, 1970.
- [20] Whitten, J. L.; Yang, H. *Surface Science Reports* **1996**, *24*, 55–124.
- [21] Jiang, D. E.; Carter, E. A. *Surface Science* **2004**, *570*, 167–177.
- [22] Gokhale, A. A.; Mavrikakis, M. *Preprint Paper - American Chemical Society, Division of Fuel Chemistry* **2005**, *50*, 149.
- [23] Sorescu, D. C.; Thompson, D. L.; Hurley, M. M.; Chabalowski, C. F. *Physical Review B* **2002**, *66*, 035416/1–035416/13.
- [24] Bromfield, T. C.; Curulla Ferré, D.; Niemantsverdriet, J. W. *ChemPhysChem* **2005**, *6*, 254–260.
- [25] Huo, C.-F.; Ren, J.; Li, Y.-W.; Wang, J.; Jiao, H. *Journal of Catalysis* **2007**, *249*, 174–184.
- [26] A useful resource for more historical literature related to the FT synthesis can be found at: <http://www.fischer-tropsch.org>.
- [27] Van Steen, E.; Schulz, H. *Applied Catalysis A* **1999**, *186*, 309–320.

Chapter 2

Method and model verification

Theoretical chemistry is a peculiar subject. It is based on an equation that can hardly ever be solved.

— PATRICK WILLIAM FOWLER – ‘ORBITAL UPDATE’
Nature, 343, (1990) 222

2.1 Introduction

USUALLY catalysis research is considered to be empirical in nature, but in the last decades theoretical methods have been applied to elucidate some of the highly complex mechanisms of catalysis chemistry. In this regard the methods of atomistic computational chemistry have been of great advantage. Currently computational methods are very widely used to complement and understand experimental observations, as well as in the development of predictive theories. These types of computational chemical methods are widely applied in various fields of research including chemistry, physics, life sciences and engineering. The theoretical modelling of iron and iron surfaces in particular have received quite some interest in the past. The academic and industrial importance of modelling the iron system can be seen in solid state physics [1], surface science [2], Fischer-Tropsch synthesis [3–7] and the steel industry [8].

2.2 Computational chemistry methods

In general we can divide the available atomic scale computational methods into two groups. The first group uses force fields to describe the interatomic interactions. These force fields are usually empirically parameterised. These type of models are useful in

describing geometrical structures, intermolecular interactions and energy trends, and can be used to calculate systems with many atoms. The force field approach does not attempt to solve the Schrödinger equation and is therefore usually not used to study chemical bond changes.

The second group of computational methods do not employ empirical methods. These first principle methods are designed to calculate the electronic structure of the considered system. By using quantum mechanics, the electronic structure of various chemical systems can be approximated. Since the energies and properties of catalytic systems are highly dependent on their electronic structure, quantum mechanical methods play an important role describing catalysis chemistry. There are various approaches in this group, including Hartree Fock (HF), recent post-HF *ab initio* methods and Density Functional Theory (DFT). Density functional theory (DFT) is one of the most useful methods to study catalysis theoretically, since it is a widely used theory which can describe systems with a high concentration of electrons, such as metals [9]. In this thesis we mainly aim to describe the chemical bonding and reactivity on an iron surface. The DFT method is therefore a very useful theoretical approach to study this system and can be used to decipher the complexities of such systems.

2.2.1 Density functional theory

The main aim in first principle methods, like DFT, is to solve the time-independent Schrödinger equation [10] for the system under consideration. First principle calculation methods are derived from the full Hamiltonian operator (\hat{H}) in the Schrödinger equation:

$$\hat{H}\Psi = E\Psi \quad (2.1)$$

with

$$\hat{H} = \frac{-\hbar}{2m}\nabla^2 + V \quad (2.2)$$

where E represents the energy of the particle or system, Ψ is the wavefunction of the particle or system, V describes the potential, ∇^2 is the second derivative operator and \hbar is Planck's constant divided by 2π [9]. The Hamiltonian operator contains kinetic and potential energy operators that act on the wavefunction of the system. Since this equation can only be exactly solved for a limited number of systems, approximations are needed to calculate the remaining systems.

There are two main approximations which are generally applied to chemical systems. The first is the Born-Oppenheimer approximation [11] in which we assume that the electronic and nuclear wavefunctions are independent due to the large mass mismatch. This decouples the nuclear and electronic movements and in most chemical

systems the nuclei can be considered as point charges. To calculate the energy of a system now only requires the solution of the electronic wavefunction.

The second approximation concerns the electron-electron interaction. To describe a multi-electron system the electrons are considered as moving within the field of the other electrons. To be able to solve these systems an iterative procedure to converge the electronic structure has to be followed. This procedure results in what is called the self-consistent field (SCF).

DFT, developed by Kohn, Hohenberg and Sham [12, 13], is used to give a quantum chemical description of systems with a high concentration of electrons. According to the Hohenberg-Kohn theorems a one-to-one mapping exists between the ground state wavefunction of a many-particle system and the ground state electron density. The ground-state energy of a system is therefore uniquely dependent on its electron density, ρ . The power of DFT is evident for large systems, since it replaces the many-body wavefunction of the electrons with the basic quantity of the electron density. The many-body wavefunction depends on $3N$ spatial variables for the N electrons. In DFT the electron density is a function of only three variables and is therefore practically simpler to solve.

In DFT the total energy of a chemical system, $E(\rho)$, can be expanded as:

$$E(\rho) = U(\rho) + T(\rho) + E_{xc}(\rho) \quad (2.3)$$

where U represents the Coulombic interaction energy, T the kinetic energy and E_{xc} the exchange-correlation energy contribution [9]. The first two terms can be expressed exactly, but there is no exact expression for E_{xc} . Different DFT exchange-correlation functionals are used to estimate the E_{xc} term.

The local density approximation (LDA) was developed as a first approach to the exchange-correlation problem. In the LDA approach the exchange-correlation energy is expressed as

$$E_{xc}^{LDA}(\rho) = \int d^3\mathbf{r} \rho(\mathbf{r}) \mu_{xc}^{LDA}(\rho) \quad (2.4)$$

where $\mu_{xc}^{LDA}(\rho)$ is the LDA exchange-correlation potential as a functional of the charge density (ρ). The LDA exchange-correlation potential contribution for a point with a specific electron density is set to that of a homogeneous free electron gas with the same electron density. To calculate magnetic systems, electron spin has been included in this approach by calculating the exchange-correlation for each spin component. When applied, the LDA approach generally leads to overbinding effects in chemical bonds [14] and in some cases (like for iron) the prediction of the incorrect magnetic state [15, 16]. To improve on this over-simplification, non-local gradient effects have been included.

This resulted in what is known as the generalised gradient approximation (GGA). In this approach the effect of both the electron density and the electron density gradient is included to map the exchange-correlation. In general the GGA exchange-correlation energy (E_{xc}^{GGA}) is expressed as

$$E_{xc}^{GGA}(\rho) = \int d^3\mathbf{r} \rho(\mathbf{r}) \mu_{xc}^{GGA}(\rho, \nabla\rho) \quad (2.5)$$

where μ_{xc}^{GGA} is the GGA exchange-correlation potential which includes both the local density (ρ) and a functional describing the non-local effects of the electron density gradient ($\nabla\rho$). The information obtained from the gradient of the electron density can be included in this expression in many ways. As a consequence of this, a large number of specific GGA exchange-correlation functionals arose. Among these are the widely used functionals such as BP [17], PW91 [18], PBE [19], BLYP [20] and RPBE [21].

In the DFT application used in this work, wavefunctions of the systems under consideration need to be solved within a 3D periodic unit cell. Bloch's theorem [22] states that a discrete plane-wave basis set can be used to construct these electronic wavefunctions in the periodic cell. Bloch waves ($\psi_{nk}(\mathbf{r})$) are usually expressed as the product of a periodic function ($u_{nk}(\mathbf{r})$) and modulating function ($e^{i\mathbf{k}\cdot\mathbf{r}}$):

$$\psi_{nk}(\mathbf{r}) = e^{i\mathbf{k}\cdot\mathbf{r}} u_{nk}(\mathbf{r}) \quad (2.6)$$

Because the Kohn-Sham potential converges rapidly, the contribution of the plane waves with small kinetic energies are more important than those with large kinetic energies. This allows for a truncation of the basis set at a chosen basis set cutoff energy. This energy is chosen in such a way that the error in the computed total energy and its derivatives is negligible.

A disadvantage of the planewave approach is that the number of planewaves that are needed to describe the wavefunction is determined by the largest curvature of the wavefunction. This becomes a serious problem for the core electrons of heavier elements. The wavefunctions of these electrons have rapid oscillations because of the strong ion-electron interaction potential. These oscillations would require extremely large planewave basis sets to solve accurately, and the computational cost then becomes prohibitively large. To overcome this problem a pseudopotential representation of the atoms can be used. This approach was first applied to solids by Hellmann [23, 24]. Since the valence electrons are the main contributors to the chemical bonding, the non-valence or "core" electrons can be considered as being in fixed states. A pseudopotential is thus constructed to represent the potential of the nucleus and the fixed "core" electrons [25, 26]. These pseudopotentials are created in

such a way that the pseudopotential and the resulting charge density matches the respective all-electron potential and charge density beyond a certain cutoff radius (r_c). When the norms of the resulting pseudo-wavefunction and the original wavefunction are the same up to this cutoff radius, the pseudopotential is referred to as norm-conserving [27, 28]. Pseudopotentials are usually smoother than the original potential and result in simpler wavefunctions, which in turn requires a smaller planewave basis set to solve. The smaller the basis set that can be used, the "softer" the pseudopotential is considered to be. The use of pseudopotentials offers the advantage that relativistic effects of the core electrons can be included, allowing the system to be solved non-relativistically.

For many first-row and transition metals the basis sets that are required still remain quite large within this approach. Vanderbilt [29] showed that when the norm-conservation requirement is relaxed an even smaller basis set can be used to obtain the same accuracy. These are referred to as ultrasoft pseudopotentials because the plane wave basis set cutoff energies required for these potentials are much lower than those required by norm conserving pseudopotentials. These ultrasoft pseudopotentials have been shown to be quite accurate and transferable for transition metals such as iron [1].

Although DFT has been used since the 1970's, there are still some difficulties inherent to the current applications of DFT. Some weak intermolecular interactions, like Van der Waal's forces are not described correctly (e.g. noble gas atoms interacting with a surface) [30]. Another weakness is strongly correlated systems. These systems include insulators and semi-conductors in which the calculation of the band gap is incorrectly calculated (for an example see ref. [31]). It has also been shown that on some metal surfaces the slightly incorrect energy of the antibonding orbital of the CO molecule can lead to incorrect site preferences [32]. Electronically excited states are also not accurately described, because the current electron density mapping used in DFT is only valid for the electronic ground state [33]. Some developments to overcome these problems are presently under investigation. These include corrections done by altered functionals or by including additive correction terms.

In DFT calculations the Schrödinger equation is solved in terms of the electron density by an iterative procedure. This procedure starts from initial "guess" wavefunctions which is usually created by the basic linear combination of typical atomic orbitals. From this a new wavefunction is constructed by calculating each electron's wavefunction (using a numerical basis set). This step is iterated to produce a self-consistent field (SCF) within a specified energy tolerance. The electron density calculated by this method is used to evaluate the system energy. A flow chart of this SCF cycle can be

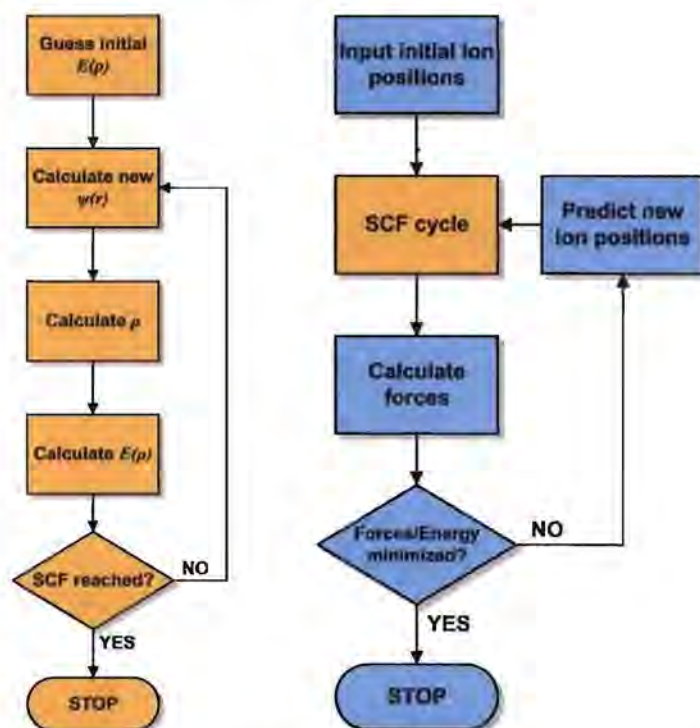


Figure 2.1: Flow charts of the SCF cycle (left) and the geometrical optimization cycle (right) used to calculate energies and structures with DFT.

seen in Figure 2.1. To calculate the equilibrium geometry of a system the positions of the nuclei are optimised by minimising the forces on the ions (Figure 2.1). The forces are calculated by taking the first derivative of the energy (calculated with the SCF cycle for each geometry) with regard to the ionic positions.

2.2.2 Surface modelling approaches

Different surface molecular modelling approaches exist which employ DFT. The most preferred methods are cluster, embedded cluster and periodic slab calculations [34].

Finite size cluster calculations are done by explicitly calculating all the atoms of a small cluster of atoms. The geometry of such a cluster is usually chosen to represent the geometry of a certain surface or surface site. A cluster model has limitations in that it only has an artificial surface plane effect. An energy gap between HOMO and LUMO is always present when using clusters. A real metal surface has a continuous band at the Fermi level. Magnetic moments of a finite cluster may also differ considerably from that of a slab or the real surface. Upon optimisation of these clusters, structures might be produced which are unrelated to an extended surface [35]. Another limitation of this model is that the calculation time scales with the increase in the basis set size to the order of N^3 (where N is the number of atoms), limiting the calculations to clusters with only a very small number of atoms.

In the periodic slab approach a surface is considered to be a slab of finite thickness which extends infinitely into the other two dimensions. Applying periodic boundary conditions reproduces this infinity and allows us to calculate a much smaller number of atoms. Such a unit cell representation can be used to represent large flat and stepped surfaces and even mimic nanocrystal edges [36]. This allows the band theory for periodic systems to be exploited. Periodic systems also permit surface coverage effects to be explored [37].

By using periodic boundary conditions the system wavefunction also becomes periodic. Using radially expressed basis functions to solve this wavefunction can be quite time consuming and therefore a periodic plane wave basis set is used. The direct Cartesian space in which the system is expressed is transformed to reciprocal space. The kinetic energy operator is diagonal when using a plane wave representation in reciprocal space. In the same way the potential operator is diagonal in real space. Fast Fourier Transforms are used to transform between these two space representations. This is done since a smaller set of plane waves is needed to describe the system when calculating the wavefunctions in reciprocal space. Using a smaller plane wave basis set significantly increases the speed of the calculations.

The core electron wavefunctions usually have strong oscillations which would require a very large plane wave basis set to be solved. By the application of the pseudopotential approximation [38] the potential of the nucleus and the effects of the motion of the non-valence electrons of the atom is replaced by an effective potential, or pseudopotential. The Coulombic potential in the Hamiltonian of the Schrödinger equation is therefore replaced by an effective potential. This allows us to calculate the pseudo-wavefunction which is a representation of only the valence electrons. A smaller plane wave basis set is therefore required to solve these wavefunctions.

The periodic slab DFT method can be applied to a specific molecular geometry to calculate the following information [34, 37]:

- Total system energy
- Equilibrium geometry (after optimisation)
- Orbitals or band structure
- Total wavefunction
- Charge distributions and electronic densities
- Dipole moments
- Adsorption energy

- Vibrational frequencies (these can be used to calculate the zero-point vibrational energy corrections and estimate the thermodynamic properties (see Appendix C))

2.3 General computational method

The DFT quantum chemical calculations¹ in this study were done using the Cambridge Sequential Total Energy Package (CASTEP) [39] as applied in the Materials Studio software package [40]. The program solves the Kohn-Sham equations self-consistently within periodic boundary conditions and the pseudopotential approximation using a plane wave basis set. The general gradient approximation (GGA), using the PW91 [18], PBE [19] and RPBE [21] functionals was used to calculate the electron exchange-correlation contribution. A Gaussian smearing method was applied to the electron distribution at the Fermi level to improve the SCF convergence. The ion-electron interactions were described by ultrasoft pseudopotentials as included in the CASTEP suite [40]. The Monkhorst-Pack scheme [41] was used to perform the Brillouin zone sampling.

Geometry optimisations were performed by using the BFGS [42] method as implemented in CASTEP.

2.4 Bulk iron model verification

In applying this calculational approach we are faced with conflicting demands: The calculation must be set up in a way that describes the surface and adsorbate's interaction with the surface, as accurately as possible. However, it must be considered that computational time is strongly dependent on the number of atoms present and the calculational setup parameters [34]. The optimisation of the calculational parameters is therefore very important in establishing a model that can be used to study a broad range of possible systems. Although this model should have a very good accuracy compared to experiments, it must also be able to finish the calculations within a reasonable amount of time. Since the structural and electronic properties of the surfaces and the surface reactions depend on the chosen bulk model, it is of the utmost importance to obtain a very accurate bulk model, which is fully converged with regard to the modelling parameters.

¹All calculations were performed on a 64-bit x86 computer cluster using the Rocks V cluster operating system. Compute node specification: 2 × dual core AMD Opteron 275 @ 2.2GHz CPU with 8GB RAM.

2.4.1 Verification method

There are a number of optimisation parameters that need consideration when building a bulk and surface DFT model. These are the exchange-correlation functional, the pseudopotentials used to represent the electron-ion interaction, the special k-points for Brillouin zone integration, the plane-wave cutoff energy, the applied electron smearing, the vacuum spacing and slab thickness [43]. In optimizing these parameters, the accuracy of the model of bulk iron can be evaluated by comparing calculated values like the bulk modulus, the magnetic moment and the lattice parameters, to the experimental values. For surface models (strongly dependent on the chosen bulk structure) surface energies can be used to verify the model.

The bulk modulus (B) and equilibrium lattice parameters (a) were calculated by fitting the calculated energies and lattice parameters to the Birch-Murnaghan equation [44, 45].

By calculating the surface energy we can estimate the accuracy of the representation of the surface, since it can be compared to experimental values. Surface energies (E_{surf}) per atom for the p(1×1) iron surfaces were calculated by

$$E_{surf} = \frac{(E_{slab} - N \cdot E_{bulk})}{2} \quad (2.7)$$

and the surface energy normalised to the surface area (γ_s) by

$$\gamma_s = \frac{(E_{slab} - N \cdot E_{bulk})}{2A} \quad (2.8)$$

where E_{slab} and E_{bulk} are the total energies of the slab and the bulk respectively, N represents the number of iron atoms in the slab and A represents the surface area of the slab unit cell.

The models that will be discussed in the following sections are the bulk and the surface slab models, as well as the optimised gas phase molecules.

2.4.2 Bulk Calculations

In this section we describe the verification of various model parameters of the bulk Fe system. The parameters we consider are the cutoff energy, k-points, smearing, exchange-correlation functional and the pseudopotentials.

2.4.2.2 Smearing

Smearing of the electrons at the Fermi level is applied to speed up the SCF convergence. In this process the electron occupation at the Fermi level is allowed to be smeared over the bands at the Fermi level. These partial band occupancies simulate the effect of the electronic state of a metal at a temperature higher than 0 K. This effectively adds some electronic entropic energy to the system. The energy that is calculated has to be extrapolated to $\sigma \rightarrow 0$ eV to get the 0 K energy value. The optimum σ value that has been chosen to be used during further calculations was 0.1 eV.

2.4.2.3 Exchange-correlation functional

A very important parameter is the exchange-correlation functional. The exchange-correlation functional is used to approximate the exchange and correlation electron-electron interactions. Varying this parameter yields different energies, geometries and magnetic properties for the bulk iron system.

Table 2.1 shows the comparison of our present calculations to the experimental values and some calculated values from literature. It can be seen that initially (before approximately 2003) the important characteristic that was calculated was the lattice parameter, although the bulk modulus and magnetic moment was not far off for most of these calculations. After 2003 it seems as if the focus shifted to predicting the magnetic moments correctly while slightly sacrificing accuracy with regard to the lattice parameter (averaging around 2.83 Å).

Our calculations seem to give similar values to those after 2003 when the PW91 and PBE functionals were used in CASTEP. Our CASTEP RPBE calculations give results with quite accurate lattice parameters and bulk moduli. In this case the magnetic moments are overestimated by a mere 0.1 μ_B .

Although all these results seem quite accurate with regard to the methods employed, the observed trend towards predicting the magnetic moments correctly, while sacrificing the accuracy in the lattice parameter (geometry), must be considered. Since this study is the first step toward studying the adsorption on iron surfaces, the influence of both geometry and electronics must be as accurate as possible to avoid invalidating the adsorption model. If the geometry is incorrect, the adsorption overlayer geometry will also be incorrect. The energies that will be calculated could therefore become suspect if there are strong lateral interactions between adsorbed species. Then again, the electronic occupation of iron would be very important in predicting the adsorption geometries and energies. If the electronic character is too far off, it could also lead to incorrect geometries and either overbinding or underbinding of the cho-

Table 2.1: Chronological summary of the calculated properties of bulk α -Fe.

Author	Year	Package	Functional ^a	a (Å)	B (GPa)	M (μ_B)
Exp. [46, 47]				2.866	168	2.22
Ref.[15]	1991		PW91	2.880	182	2.18
Ref.[48]	1992		PW91	2.835	176	2.24
Ref.[49]	1996		PW91	2.858	169	2.32
Ref.[1]	1997		PW91	2.860	155	2.32
Ref.[50]	1999		FLAPW	2.253	172	2.17
Ref.[51]	1999		PAW	2.850	151	2.32
				2.830	174	2.20
Ref.[52]	2002	VASP	PW91	2.869	140	2.37
Ref.[4]	2002	VASP	US-PW91	2.865	160	2.33
Ref.[53]	2002	VASP	PAW-PW91	2.830		
Ref.[54]	2003	VASP	PAW-PW91	2.834	174	2.21
Ref.[55]	2003	VASP	FLAPW	2.840	174	2.17
Ref.[56]	2004	CASTEP	US-PBE	2.826		2.24
Ref.[57]	2004	VASP	PBE	2.830	174	2.20
Ref.[58]	2004	VASP	PAW-PW91	2.834	174	2.20
Ref.[3]	2005	VASP	US-PW91	2.831		
Ref.[5]	2005	VASP	PAW-PW91	2.834	170	2.20
Ref.[59]	2005	CASTEP	US-PBE	2.826		2.24
Ref.[60]	2006	CASTEP	US-PW91	2.850		2.24
Ref.[6]	2006	VASP	US-PW91	2.865	159	2.31
	2006	VASP	PAW-PW91	2.831	173	2.25
	2006	VASP	PAW-PW91	2.833	171	2.25
Ref.[7]	2007	VASP	US-PW91	2.855	156	2.30
Ref.[61]	2007	VASP	PAW-PW91	2.844	179	2.20
Present work		CASTEP	US-PW91	2.824	193	2.20
			US-PBE	2.820	205	2.24
			US-RPBE	2.852	176	2.31

a) US: ultra-soft pseudopotential. PAW: Projector Augmented Wave potential

sen adsorbate. It would therefore be useful to consider both the CASTEP RPBE and PW91 functionals to study the changing of the exchange-correlation functional in the subsequent surface model verifications.

2.4.2.4 Pseudopotentials

When comparing the same functional in the CASTEP and VASP packages (see Table 2.1) it can be seen that the results differ somewhat, although both were obtained with US-PW91. This is mostly due to the slightly different pseudopotentials that the two packages use to represent the ion-electron interactions.

This is also a parameter that can have an immense effect on the accuracy of the modelled system. Included in the CASTEP package are a range of five different pseudopotential representations for iron. The PW91 functional (16x16x16 k-points and 500eV cutoff) was used to compare the available CASTEP pseudopotentials, as shown in Table 2.2. By varying the pseudopotential, the accuracy of the calculations changed quite drastically.

Table 2.2: Variation of the calculated lattice parameter a , bulk modulus (B) and magnetic moments (M) with different pseudopotentials. Values in brackets are the %-error compared to the experimental values. Calculations were performed with the PW91 functional.

Pseudopotential	a (Å)	B (GPa)	M (μ_B)
Fe.usp	2.954 (3.3)	131 (22)	3.26 (47.7)
Fe.recpot	3.089 (8.0)	82 (51)	2.98 (34.9)
Fe.PBE	3.020 (5.6)	117 (30)	3.35 (51.9)
Fe.PBEcc	2.811 (1.7)	211 (26)	2.16 (1.9)
Fe.uspcc	2.824 (1.5)	193 (15)	2.20 (0.9)

The first three iron pseudopotentials in Table 2.2 are the normal iron pseudopotential ("Fe.usp"), the reciprocal potential ("Fe.recpot") and the PBE functional optimised potential ("Fe.PBE"). These three potentials are non-core corrected, while the last two pseudopotential calculations in the table includes non-linear core corrections. These core corrections are important since the core-valence exchange-correlation interactions are strong and non-linear in magnetic systems. This effect can be corrected for when generating a pseudopotential [62]. As can be seen from the bulk lattice parameter values in Table 2.2, the non-core corrected pseudopotentials give values which are larger than the experimental value by between 3 and 8%. The big difference lies in the magnetic moments which are all at least 34% larger than the experimental value. The use of core corrected pseudopotential for iron is therefore a necessity.

The last two considered pseudopotential calculations in Table 2.2 include core corrections. It is clear that these potentials give much better values for the bulk lattice parameters. The "Fe.uspcc" (ultrasoft pseudopotential with core correction) was chosen as the pseudopotential to be used during further calculations, since it is transferable to the exchange-correlation functionals like RPBE. Although the "Fe.PBEcc" pseudopotential did perform well, we cannot be sure about its transferability to other functionals since it is optimised for use with the PBE functional. The "Fe.uspcc" will therefore be used in all other calculations.

2.4.3 Surface Calculations

When the iron bulk model has been fully optimized, the next step is to calculate the surfaces. In this section the surface energies of the Fe(110), Fe(100) and Fe(111) surfaces are considered. Since the initial bond lengths of a surface model is directly dependent on the bulk structure used, some parameters do not need to be optimised again. The exchange correlation-functional and the pseudopotentials used for the surface and the corresponding bulk calculations needs to be the same to ensure correct calculation of surface energies. Parameters that need optimisation are the inter-slab vacuum spacing, surface unit cell k-mesh and cutoff energy.

2.4.3.1 Vacuum spacing

An extensive study of the vacuum spacing between the iron slabs was performed to find the optimum spacing at which the two slabs do not significantly interact any more. The inter-slab vacuum space was increased to create a surface. This was done for a four layer slab without relaxing the atomic coordinates.

The results for the Fe(110) surface with the PW91 functional can be seen in Figure 2.3. As the vacuum spacing increases from 2 Å (Fe(110) interlayer spacing) to 12 Å, the energy per atom increases and converges to within 1 mJ/m² at 10 Å. The average magnetic moment per atom was also monitored in the creation of a the surface. It increases to a maximum near 3.5 Å and subsequently decreases to converge at 10 Å. The maximum in magnetic moment can be ascribed to the fact that slabs only truly start to separate at 3.5 Å. Between 2.012 Å and 3.5 Å, the orbital overlap at the separation between the surfaces becomes smaller, but it is still large enough to simulate a bulk-like structure that is only slightly stretched in one dimension. This decrease in electronic overlap will yield more α -filled bands than β -filled bands which, in turn, will enhance the magnetization of the iron. At a distance further than 3.5 Å the two slabs start to separate yielding a new stable electronic state of the Fe(110) surface. A similar trend was obtained for the RPBE functional. The vacuum spacing for Fe(100) started to converge at 8 Å, but to be sure that the inter slab interaction are not significant we will use a vacuum spacing of 10 Å in further calculations.

2.4.3.2 Cutoff energy and k-points

We optimised the k-meshes and cutoff energies for the Fe(100), Fe(110) and Fe(111) surfaces. The optimised parameters used to calculate surface energies are summarised in Table 2.3.

2.4.3.3 Surface energy comparison

The calculated surface energy can be used as a measure to estimate the accuracy of the representation of the surface. Figure 2.4 shows the calculated surface energies for Fe(110), Fe(100) and Fe(111) as calculated with the PW91 and RPBE functionals. The coordinates of all the atoms in the respective slabs were optimised. The converged surface energies (to within 1% error) are summarised in Table 2.3. For PW91 the resulting average surface energy per unit area (γ_s) is at least 0.2 J.m⁻² larger than that of the RPBE. The Fe(110) surface is the most stable for PW91, although for the RPBE the Fe(110) and Fe(100) are of similar stability. If the surface energy per atom (E_{surf}) is considered, the Fe(110) is much more stable than the Fe(100) surface for both function-

als. The Fe(111) surface is less stable than the other two surfaces by about 0.27 J.m^{-2} . The stability orders of these surfaces correspond well to other calculations [61].

Our RPBE calculated surface energy values seem to agree reasonably well with the experimental estimates for the polycrystalline surface based on the liquid metal surface tension data extrapolated to 0 K (2.41 J.m^{-2} [63] and 2.55 J.m^{-2} [64]).

2.4.4 Gas phase molecules

The energies and properties of the gas phase molecules of H_2 and CO (which will be used throughout all of this work) was calculated with RPBE by placing each of these molecules in a cubic unit cell with 10 \AA sides. For H_2 we obtained an equilibrium bond distance of $r_e = 0.749 \text{ \AA}$, a vibrational frequency of $\nu = 4421 \text{ cm}^{-1}$ and a dissociation energy of $D_e = 4.564 \text{ eV}$. These values are in good agreement with the experimental values ($r_e = 0.741 \text{ \AA}$, $\nu = 4401 \text{ cm}^{-1}$ and $D_e = 4.560 \text{ eV}$) [65]. For the CO we calculated the equilibrium bond distance as $r_e = 1.147 \text{ \AA}$ and the vibrational frequency as $\nu = 2170 \text{ cm}^{-1}$, which are both in good agreement with the experimental values ($r_e = 1.128 \text{ \AA}$ and $\nu = 2170 \text{ cm}^{-1}$) [65]. These values are also in good agreement with other similar calculations [4, 5, 54, 57].

2.5 Conclusions

We presented the background of the DFT calculations that will be the basis of our theoretical work, as well as the verification of the bulk, surface and gas models. The optimisation of the pseudopotential, the k-points and cutoff energies were investigated. The RPBE exchange-correlation functional has proved to represent α -Fe bulk and Fe surfaces very well. The calculated gas molecule models using this functional are also in good agreement with experimental values. In the following chapter we will discuss the adsorption of hydrogen and CO studied with the RPBE optimised surface slabs.

Bibliography

- [1] Moroni, E. G.; Kresse, G.; Hafner, J.; Furthmüller, J. *Physical Review B* **1997**, *56*, 15629–15646.
- [2] Spencer, M. J. S.; Hung, A.; Snook, I. K.; Yarovsky, I. *Surface Science* **2002**, *513*, 389–398.
- [3] Bromfield, T. C.; Curulla Ferré, D.; Niemantsverdriet, J. W. *ChemPhysChem* **2005**, *6*, 254–260.
- [4] Sorescu, D. C.; Thompson, D. L.; Hurley, M. M.; Chabalowski, C. F. *Physical Review B* **2002**, *66*, 035416.

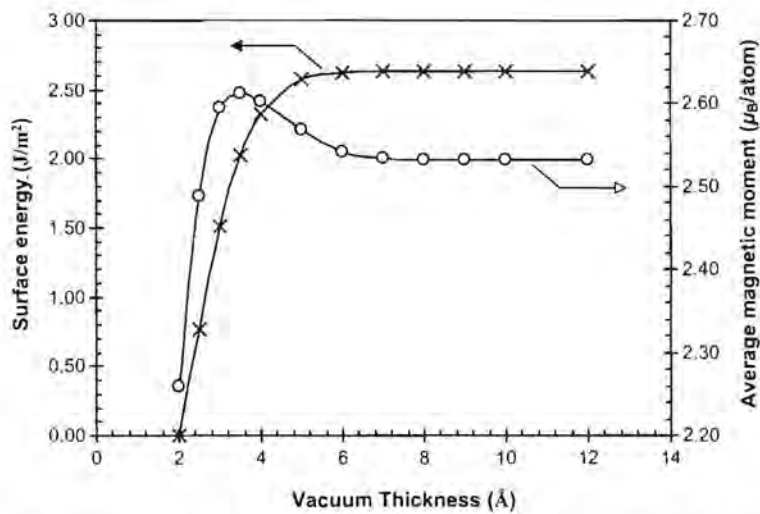


Figure 2.3: The effect of Fe(110) surface creation on the surface energy (x) and the average magnetic moment (o) using PW91.

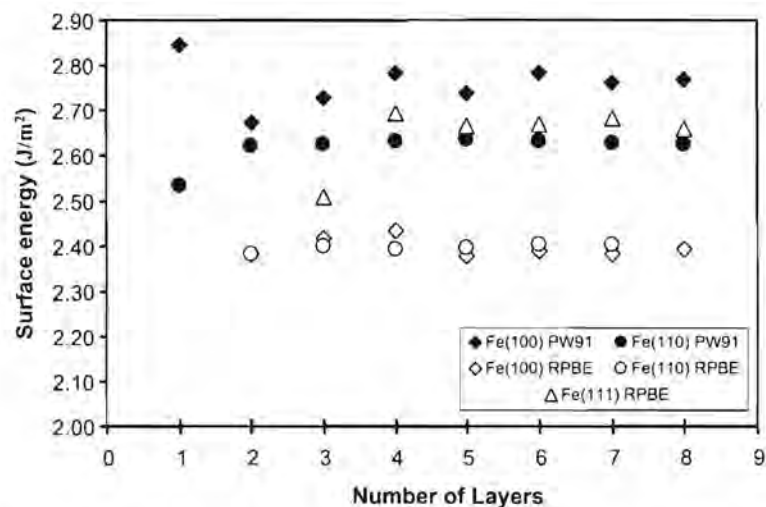


Figure 2.4: Surface energies (γ_s) of Fe(110), Fe(100) and Fe(111) as a function of the slab thickness.

Table 2.3: Summary of the optimised cutoff energies, k-meshes and surface energies for Fe surfaces.

Surface	Functional	Cutoff Energy (eV)	k-mesh	E_{surf} (eV)	γ_s (J/m ²)
Fe(110)	PW91	500	11x11x1	0.92	2.63
	RPBE	560	15x15x1	0.86	2.40
Fe(100)	PW91	500	9x9x1	1.37	2.77
	RPBE	520	9x9x1	1.22	2.40
Fe(111)	RPBE	520	6x6x1	2.35	2.67

- [5] Sorescu, D. C. *Catalysis Today* **2005**, *105*, 44–65.
- [6] Sorescu, D. C. *Physical Review B* **2006**, *73*, 155420.
- [7] Lo, J. M. H.; Ziegler, T. *The Journal of Physical Chemistry C* **2007**, *111*, 11012–11025.
- [8] Bernstein, I. M.; Thompson (Eds.), A. W. *Hydrogen Effects in Metals*; AIME, Warrendale, PA, 1981.
- [9] Parr, R.; Yang, W. *Density-Functional Theory of Atoms and Molecules*, Vol. 16 of *The international series of monographs on chemistry*; Oxford University Press, 1989.
- [10] Schrödinger, E. *Physical Review* **1926**, *28*, 1049–1070.
- [11] Born, M.; Oppenheimer, R. *Annalen der Physik* **1927**, *84*, 457–484.
- [12] Hohenberg, P.; Kohn, W. *Physical Review* **1964**, *136*(3B), 864–871.
- [13] Kohn, W.; Sham, L. J. *Physical Review* **1965**, *140*(4A), 1133–1138.
- [14] Perdew, J. P.; Chevary, J. A.; Vosko, S. H.; Jackson, K. A.; Pederson, M. R.; Singh, D. J.; Fiolhais, C. *Physical Review B* **1992**, *46*(11), 6671–6687.
- [15] Singh, D. J.; Pickett, W. E.; Krakauer, H. *Physical Review B* **1991**, *43*(14), 11628–11634.
- [16] Bagno, P.; Jepsen, O.; Gunnarsson, O. *Physical Review B* **1989**, *40*(3), 1997–2000.
- [17] Becke, A. D. *Journal of Chemical Physics* **1988**, *88*, 2547–2553.
- [18] Perdew, J. P.; Wang, Y. *Physical Review* **1992**, *45*(23), 13244–13249.
- [19] Perdew, J. P.; Burke, K.; Ernzerhof, M. *Physical Review Letters* **1996**, *77*(18), 3865–3868.
- [20] Lee, C.; Yang, W.; Parr, R. G. *Physical Review B* **1988**, *37*, 785–789.
- [21] Hammer, B.; Hansen, L. B.; Nørskov, J. K. *Physical Review B* **1999**, *59*(11), 7413–7421.
- [22] Bloch, F. *Zeitschrift für Physik* **1928**, *52*, 555.
- [23] Hellmann, H. *Journal of Chemical Physics* **1935**, *3*, 61.
- [24] Hellmann, H. *Journal of Chemical Physics* **1936**, *4*, 324.
- [25] Philips, J. C. *Physical Review* **1958**, *112*, 685.
- [26] Yin, M. T.; Cohen, M. L. *Physical Review B* **1982**, *25*, 7403.
- [27] Hamann, D. R.; Schlüter, M.; Chiang, C. *Physical Review Lett.* **1979**, *43*, 1494.
- [28] Bachelet, G. B.; Hamann, D. R.; Schlüter, M. *Physical Review B* **1982**, *26*, 4199.
- [29] Vanderbilt, D. *Physical Review B* **1990**, *41*, 7892.
- [30] Ciobîcă, I. M. *The Molecular Basis of the Fischer-Tropsch Reaction* PhD thesis, Technische Universiteit Eindhoven, Eindhoven, **2002**.
- [31] Perdew, J. *International Journal of Quantum Chemistry* **1986**, *30*, 451.
- [32] Kresse, G.; Gil, A.; Sautet, P. *Physical Review B* **2003**, *68*, 073401.
- [33] Gaudoin, R.; Burke, K. *Physical Review Letters* **2004**, *93*, 173001.
- [34] Whitten, J. L.; Yang, H. *Surface Science Reports* **1996**, *24*, 55–124.
- [35] Nayak, S. K.; Nooijen, M.; Bernasek, S. L.; Blaha, P. *The Journal of Physical Chemistry B* **2001**, *105*, 164–172.
- [36] Swart, J. C. W.; van Helden, P.; van Steen, E. *The Journal of Physical Chemistry C* **2007**, *111*, 4998–5005.
- [37] Broadbelt, L. J.; Snurr, R. Q. *Applied Catalysis A* **2000**, *200*, 23–46.

- [38] Srivastava, G.; Weaire, D. *Advances in Physics* **1987**, *36*(4), 463–517.
- [39] Segall, M. D.; Lindan, P. J. D.; Probert, M. J.; Pickard, C. J.; Hasnip, P. J.; Clark, S. J.; Payne, M. C. *Journal of Physics: Condensed Matter* **2002**, *14*, 2717–2744.
- [40] *MS Modeling 4*; Accelrys Software Inc., <http://www.accelrys.com>.
- [41] Monkhorst, H. J.; Pack, J. D. *Physical Review B* **1976**, *13*(12), 5188–5192.
- [42] Fischer, T. H.; Almlof, J. *The Journal of Physical Chemistry* **1992**, *96*, 9768–9774.
- [43] Mattsson, A. E.; Schultz, P. A.; Desjarlais, M. P.; Mattsson, T. R.; Leung, K. *Modelling and Simulations in Materials Science and Engineering* **2005**, *13*, R1–R31.
- [44] Murnaghan, F. D. *Proceedings of the National Academy of Science* **1944**, *30*, 244–247.
- [45] Birch, F. *Physical Review* **1947**, *71*, 809–824.
- [46] Kohlhaas, R.; Donner, P.; Schmitz-Pranghe, N. *Zeitschrift für Angewandte Physik* **1967**, *23*, 245.
- [47] Kittel, C. *Introduction to Solid State Physics*; John Wiley and Sons, 7 ed., 1996.
- [48] Amador, C.; Lambrecht, W. R. L.; Segall, B. *Physical Review B* **1992**, *46*(3), 1870–1873.
- [49] Cho, J.-H.; Scheffler, M. *Physical Review B* **1996**, *53*(16), 10685–10689.
- [50] Herper, H. C.; Hoffmann, E.; Entel, P. *Physical Review B* **1999**, *60*(6), 3839–3848.
- [51] Kresse, G.; Joubert, D. *Physical Review B* **1999**, *59*(3), 1758–1775.
- [52] Hung, A.; Yarovsky, I.; Muscat, J.; Russo, S.; Snook, I.; Watts, R. O. *Surface Science* **2002**, *501*, 261–269.
- [53] Stibor, A.; Kresse, G.; Eichler, A.; Hafner, J. *Surface Science* **2002**, *507-510*, 99–102.
- [54] Jiang, D. E.; Carter, E. A. *Surface Science* **2003**, *547*, 85–98.
- [55] Jiang, D. E.; Carter, E. A. *Physical Review B* **2003**, *67*, 214103.
- [56] Chen, Y.-H.; Cao, D.-B.; Jun, Y.; Li, Y.-W.; Wang, J.; Jiao, H. *Chemical Physical Letters* **2004**, *400*, 35–41.
- [57] Jiang, D. E.; Carter, E. A. *Surface Science* **2004**, *570*, 167–177.
- [58] Jiang, D. E.; Carter, E. A. *Physical Review B* **2004**, *70*, 064102 1–9.
- [59] Huo, C.-F.; Li, Y.-W.; Wang, J.; Jiao, H. *The Journal of Physical Chemistry B* **2005**, *109*, 14160.
- [60] Borthwick, D.; Fiorin, V.; Jenkins, S. J.; King, D. A. *Surface Science* **2008**, *602*, 2325–2332.
- [61] Błoński, P.; Kiejna, A. *Surface Science* **2007**, *601*, 123–133.
- [62] Louie, S. G.; Froyen, S.; Cohen, M. L. *Physical Review B* **1982**, *26*(4), 1738–1742.
- [63] Tyson, W. R.; Miller, W. A. *Surface Science* **1977**, *62*, 267–276.
- [64] Miedema, A. R. *Zeitschrift für Metallkunde* **1978**, *69*, 287.
- [65] Huber, K. P.; Herzberg, G. *Molecular Spectra and Molecular Structure 4: Constants of Diatomic Molecules*; Van Nostrand Reinhold Co.: New York, 1979.

Chapter 3

Hydrogen and CO adsorption models on the Fe(100) surface

Someone told me that each equation I included in the book would halve the sales.

—STEPHEN HAWKING

3.1 Introduction

THE study of the separate adsorption of hydrogen and CO is an important first step to understand the initial steps of the Fischer-Tropsch surface reactions. In this chapter the separate adsorption of hydrogen and CO on the model Fe(100) surface will be discussed. We will also present an estimate of the adsorption equilibrium conditions.

3.1.1 Background

3.1.1.1 Hydrogen adsorption

Hydrogen adsorption studies on iron surfaces have been motivated by the importance of this process in the field of heterogeneous catalysis. This is the case since hydrogen adsorption is one of the first reactions in various catalytic cycles. This can be seen in its particular application in the ammonia synthesis [1] and Fischer-Tropsch synthesis reactions [2].

Hydrogen chemisorption on iron surfaces has been the focus of a number of studies [3–8]. Hydrogen is known to dissociatively adsorb on iron surfaces yielding atomic hydrogen on the iron surface [3, 4]. In general the Fe-H bond is mainly due to the over-

lap of the Fe 4s and the H 1s orbitals, with a small contribution by the Fe 4p and 3d orbitals [5]. Fe-H bonding generally causes a Fe-Fe bond weakening, which contributes to the problem of steel embrittlement [9, 10]. Contrary to this, hydrogen adsorption on Fe(110) pushes Fe atoms into the surface creating an even denser surface [6].

Two adsorption sites β_1 and β_2 have been identified on the Fe(100) surface. It was proposed that the Fe-H binding energy has a lower limit of 59 kcal/mol [7]. From theoretical work it has been established that the four-fold hollow site and the bridge site is available hydrogen adsorption sites [8]. Of these two the four-fold hollow site is the favoured adsorption site on this surface.

3.1.1.2 CO adsorption

In 1964 Blyholder proposed the first molecular orbital view of the bonding of CO to a Ni metal surface [11]. The occupied 5σ orbital of CO can readily overlap with the unoccupied d_{z^2} and s type orbitals of the transition metal atoms. This is accompanied by an electron donation from the CO to the iron surface. The empty $2\pi^*$ orbitals of the CO are also capable of overlapping with occupied d_{xz} and d_{yz} type orbitals of the metal atoms resulting in electron back-donation [12]. This is similar to the interactions in discrete metal carbonyls. Activation of the CO bond can therefore take place if the resulting $2\pi^*$ orbital band shifts to lower than the Fermi level [13]. A depiction of this can be seen in the density of states (DOS) diagram in Figure 3.1. This model's validity was recently confirmed [14, 15] and it was shown that the $2\pi^*$ frontier orbitals are not the solely involved π contributor and that 1π has some influence [15]. Sung and Hoffmann [16] showed that there is a strong interaction between closely adsorbed CO molecules due to the π character of the CO bond.

A number of theoretical studies of CO adsorption on the low Miller index iron surfaces have been done [13, 18–22]. CO adsorbs very strongly to the Fe(110) surface [18, 19]. It has been shown that the on top sites and on the long bridge sites are favourable adsorption sites at coverages up to $\theta_{CO} = 0.5$ ML. The dissociation of CO on this surface has an activation energy barrier of 1.52 eV. Quite a number of adsorption sites are available on the Fe(111) surface [13]. Since the Fe(111) surface unit cell represents a less dense surface than both the Fe(110) and Fe(100), it allows CO adsorption up to $\theta_{CO} = 2$ ML. The most likely adsorption configuration is the model with a tilted on top CO and a CO in the bridge-like position simultaneously.

By LEED and HREELS analysis four associative and one dissociative adsorption state of CO on Fe(100) has been found [23]. Moon et al. [24] found that the $CO(\alpha_3)$ (1210 cm^{-1}), $CO(\alpha_2)$ (2020 cm^{-1}) and $CO(\alpha_1)$ (2070 cm^{-1}) states are filled and desorbed sequentially. From these $CO(\alpha_3)$ was found to be the preferred adsorption site with a

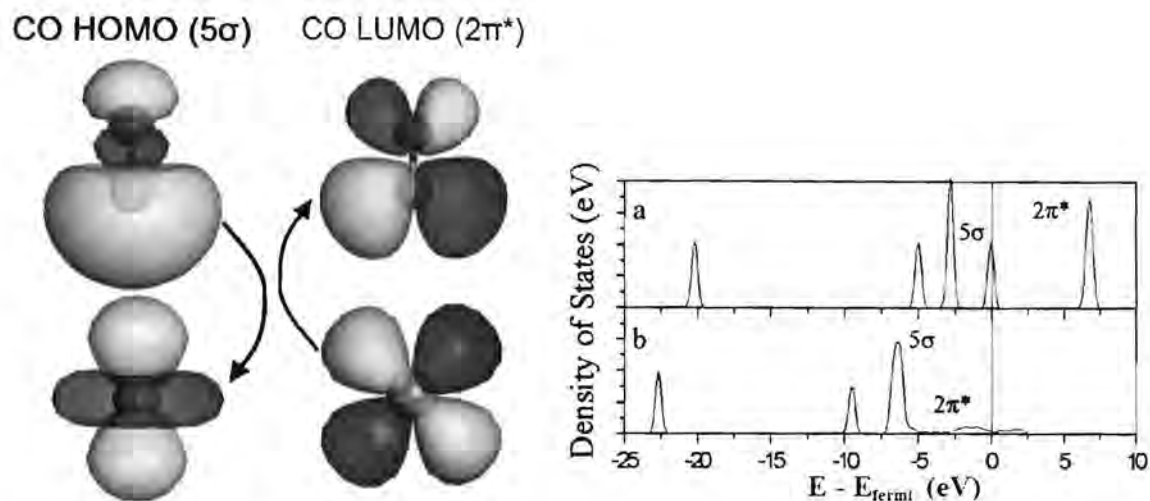


Figure 3.1: Bonding of CO to typical iron atom orbitals and the accompanying change in the DOS of CO during adsorption. The arrows indicate the donation of electrons. a) The DOS of free CO. b) The DOS for CO bonded to an iron carbide surface [17].

very low CO stretch frequency indicating a highly activated CO bond.

Nayak et al. [20] used a Fe_{22} cluster to calculate CO adsorption on Fe(100) and defined three sites for adsorption: the four-fold site, the on top site and the bridge site. By using different DFT functionals (PW91, PBE, RPBE) Sorescu et al. [21] investigated the effect of surface coverage on CO adsorption. At $\theta_{\text{CO}} = 0.25$ ML they found five possible sites for adsorption: The on top site, the bridge site, a tilted configuration at the bridge site, a four-fold site and a tilted four-fold configuration (50.2° off-normal). The tilted adsorption mode at the four-fold site was the most preferred adsorption site and it activated the CO bond most at of all the adsorption sites. At $\theta = 0.5$ ML they found that again the tilted four-fold site was the preferred adsorption site and it activated the CO the most. They found that after dissociation the carbon atoms embed into the iron lattice while the oxygen atoms remain well above the surface (1.241 \AA). The calculated activation energy of dissociation by stretching of the CO bond was 1.06 eV (24.5 kcal/mol).

Bromfield et al. [22] did a similar study, but went a step further to include a vibrational analysis to validate the proposed models. They found that at $\theta_{\text{CO}} = 0.25$ ML the four-fold hollow is the only true minimum and by far preferred adsorption site ($E_{\text{ads}} = -2.56 \text{ eV}$). At $\theta_{\text{CO}} = 0.5$ ML the on top site is shown to be a local minimum. The four-fold tilted configuration is also a local minimum and the preferred adsorption site with E_{ads} at -2.41 eV . At $\theta_{\text{CO}} = 1$ ML the tilted bridge site was not observed. The on top, bridge and hollow sites were local minima with the four-fold configuration (not tilted) as the preferred adsorption site at -1.47 eV . At a coverage of $\theta_{\text{CO}} = 1$ ML the adsorbed CO is activated, but dissociation is made impossible due to a lack of space.

They found that CO dissociation is the favoured at low coverages with an activation energy barrier of 1.14 eV. The adsorption energies that was calculated by Bromfield et al. [22] is an obvious overestimate compared to an experimental estimate, since the adsorption energy of the CO in the tilted four-fold hollow site is proposed to be 1.14 eV [25]. On a polycrystalline surface this adsorption energy is 1.604 eV [26].

3.2 Computational method

Using the surface models for Fe(100) from the previous chapter, we optimised the hydrogen and CO adsorption geometries at various coverages using the CASTEP [27] code. In the calculations we employed the generalized gradient approximation (GGA) with the Revised Perdew Burke Enzerhof (RPBE) functional [28]. A Gaussian smearing method was applied to the electron distribution at the Fermi level with $\sigma = 0.1$ eV. The ion-electron interactions were described by core corrected ultrasoft pseudopotentials as included in the CASTEP suite [29].

A seven-layer slab was used with an optimised 10 Å vacuum layer between the surfaces. To study the lower coverages, the surface was represented by using a p(2×2) periodic supercell. Adsorption was performed on both sides of the slab to facilitate the use of symmetry. The k-point sampling was generated by following the Monkhorst-Pack [30] procedure with a 5×5×1 mesh. The plane wave basis set cutoff energy was set at 400 eV. The coordinates of all atoms were fully optimized. All of the calculational set-up parameters (the k-points mesh, the number of slab layers, the vacuum spacing, etc.) were tested and optimised.

To study the adsorption of hydrogen we optimised the hydrogen adsorption geometries at a range of coverages from $\theta_H = 0.25$ ML up to $\theta_H = 2.00$ ML at various sites. We calculated the adsorption energies of these structures with molecular hydrogen gas as our zero energy reference by

$$E_{ads,H} = \frac{E_{(Fe+nH)} - E_{slab}}{2n} - 1/2E_{H_2} \quad (3.1)$$

where $E_{ads,H}$ is the heat of adsorption of H, $E_{(Fe+nH)}$ is the calculated energy of the specific adsorbed species, E_{slab} is the calculated energy of the clean Fe(100) slab, E_{H_2} is the calculated energies of the gas phase H₂ and n is the number of hydrogen atoms per p(2×2) surface supercell. These energies do not include the zero-point vibrational energy corrections. Similarly we calculated the Fe-H binding energies of these structures by:

$$E_{bind,H} = \frac{E_{(Fe+2nH)} - E_{slab}}{2n} - E_H \quad (3.2)$$

where $E_{bind,H}$ is the binding energy of hydrogen, E_H is the calculated energies of the isolated hydrogen atom and n is the number of hydrogen atoms per p(2×2) surface supercell.

For the CO adsorption calculations we optimised the CO adsorption geometries at a range of coverages from $\theta_{CO} = 0.25$ ML up to $\theta_{CO} = 1.00$ ML corresponding to the CO adsorption geometries calculated by Bromfield et al. [22]. We calculated the adsorption energies (and binding energies) of these structures with molecular CO gas as our zero energy reference by

$$E_{ads,CO} = \frac{E_{(Fe+2nCO)} - E_{slab}}{2n} - E_{CO} \quad (3.3)$$

where $E_{ads,CO}$ is the heat of adsorption of CO, $E_{(Fe+nCO)}$ is the calculated energy of the specific adsorbed species, E_{slab} is the calculated energy of the clean Fe(100) slab, E_{CO} is the calculated energies of the gas phase CO and n is the number of CO molecules per p(2×2) surface supercell.

3.3 Results and discussion

3.3.1 Hydrogen adsorption on Fe(100)

The hydrogen adsorption energies at various surface coverages has been considered by adding several hydrogen atoms to the p(2×2) surface supercell. Each supercell contains four on top and four four-fold hollow sites, and eight bridge sites. For the optimized adsorption configurations, we report the corresponding adsorption energies in Table 3.1. Although subsurface hydrogen may play a role on some surfaces, we consider here only surface hydrogen adsorption since the dissolution of hydrogen atoms into the bulk is less favourable [31].

For hydrogen adsorption (Table 3.1) it is clear that at all coverages the four-fold hollow and the bridge sites are stable with regard to H₂ gas, while the on top adsorption site is unfavoured at all the considered coverages. This is in agreement with the calculations by Sorescu [8] and the heat of adsorption proposed by Burke and Madix [7] of 0.34 eV. According to these results it is clear that H atoms would possibly be bonded at the bridge and four-fold hollow sites up to $\theta_H = 1.00$ ML. We also considered the adsorption energies for hydrogen adsorption with coverages larger than $\theta_H = 1.00$ ML. At $\theta_H = 1.50$ ML the adsorption energy is -0.17 eV. This is almost half of the adsorption energy at $\theta_H = 0.25$ ML indicating a large destabilisation at this coverage. At $\theta_H = 2.00$ ML the adsorption energy is -0.02 eV, which is nearly iso-energetic with the H₂

gas molecule.

Sorescu [8] points out that in his calculations the asymmetric three-fold hollow adsorption site, as proposed by Merrill and Madix [32] could not be found. Upon a vibrational analysis of the four-fold site adsorption geometry it was found that in our model the hydrogen atom in symmetric four-fold hollow site at $\theta = 0.25$ ML was at a second order saddle-point on the potential energy surface. Following the eigen-vectors of the imaginary frequencies we found the local minimum where the hydrogen atom is only slightly shifted to one side of the hollow. This is a very small shift of 0.018 \AA away from the centre of the four-fold hollow toward the bridge site. The hydrogen atom in this slightly off-centre geometry can still be regarded as asymmetrical adsorption in the four-fold hollow site. We could not find an asymmetric three-fold hollow adsorption site either.

3.3.2 CO adsorption on Fe(100)

The CO adsorption energies at various surface coverages has been considered by adding several CO molecules to the $p(2 \times 2)$ surface supercell. For the optimized adsorption configurations, we report the corresponding adsorption energies in Table 3.2.

The calculated CO geometries correspond to the geometries reported by Bromfield et al. [22]. Similarly we found that the CO molecule is the most stable in the four-fold hollow site with the CO molecular axis tilted away from the normal. We calculated this tilt angle as 47.72° at $\theta_{CO} = 0.5$ ML and 47.84° at $\theta_{CO} = 0.25$ ML. This tilt angle is slightly smaller than the angle calculated by Bromfield et al. [22] and the experimental value of $55 \pm 2^\circ$ [33]. A direct comparison of our values with those calculated by Bromfield et al. [22] can be seen in Figure 3.2. The trend in our values for the CO adsorption energies is similar to the trend in their calculated values. The main difference is that they used the PW91 functional where we used the RPBE functional. The difference between these trends can be clearly seen in the nearly constant shift in the trend of about 0.5 eV. If we compare these two sets of values to the experimental estimates of the adsorption energy of CO (1.14 eV [25] and 1.604 eV [26]), it is clear that our values are more in line with these values. Hammer et al. [28] showed that the RPBE usually improves agreement of calculated energies of chemisorption on transition metals with the experimental data. The values in Table 3.2 also show some correspondence to the other calculated values [21]. As a further confirmation of our calculated adsorption geometries we calculated the vibrational frequencies of the tilted CO in the four-fold hollow at $\theta_{CO} = 0.25$ ML. The CO-stretch normal mode had a frequency of $\nu = 1174 \text{ cm}^{-1}$ which is in good agreement with the experimental value ($\nu = 1210 \text{ cm}^{-1}$) [24].

Table 3.1: Calculated adsorption energies of H on Fe(100) in eV per H atom.

θ_H [ML]	Adsorption site		
	On top	Bridge	Hollow ^a
0.25	0.26	-0.28	-0.31
0.50	0.32	-0.21	-0.31
1.00	0.54	-0.18	-0.30
1.25			-0.27
1.50			-0.17
1.75			-0.14
2.00			-0.02

^a At $\theta_H > 1.00$ ML the H is on both bridge and hollow sites.

Table 3.2: Calculated adsorption energies of CO on Fe(100) in eV per CO.

Site	Coverage θ_{CO}		
	0.25 ML	0.50 ML	1.00 ML
On top	-1.31	-1.29	-0.93
Bridge	-1.18	-1.24	-0.92
Hollow	-1.44	-1.46	-1.18
Tilted hollow	-1.89	-1.88	-

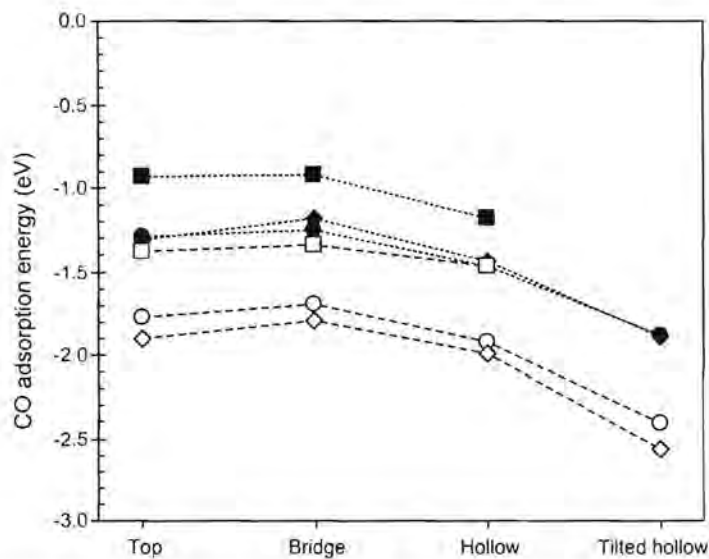


Figure 3.2: A comparison of the calculated RPBE CO adsorption energies (black) with the PW91 literature values (white) [22]. (\diamond - $\theta_{CO} = 0.25$ ML; \circ - $\theta_{CO} = 0.50$ ML; \square - $\theta_{CO} = 1.00$ ML) Dashed lines are only guides for the eye.

The vibrational analysis also confirmed that tilted CO in the four-fold hollow site is a local minimum at $\theta_{CO} = 0.25$ ML as was shown by Bromfield et al. [22]. The bond length of the adsorbed CO is stretched (1.308 Å) with regard to the gas phase CO ($r_e = 1.147$ Å). This indicates a weakening of the CO bond, which is in line with the low CO-stretch frequency. From the CO adsorption energy trend in Table 3.2 it is clear that all these CO adsorption geometries are stable with regard to gas phase CO, although according to Bromfield et al. [22] only some geometries are local minima on the potential energy surface.

3.4 Equilibrium surface coverage

To consider the separate adsorption of hydrogen and CO at Fischer-Tropsch conditions it is necessary to cross the temperature and pressure gaps to look at coverage of hydrogen and CO at temperatures of between 500 K and 650 K, and pressures of at least 1 bar. This can be done by using statistical thermodynamics. These methods were applied by Faglioni and Goddard [34] whereby they derived a general model to estimate the equilibrium surface coverage of hydrogen on a metal surface.

3.4.1 H₂ equilibrium surface coverage

There are a few assumptions inherent to the Faglioni and Goddard [34] model. The first assumption is included in the three models they propose for the behaviour of hydrogen on the metal surface. The second is in the way that the metal-hydrogen binding energies are estimated. It is also assumed that the adsorption energy is independent of the temperature. Furthermore we can assume that hydrogen gas is an ideal gas for this analysis.

With regard to the way that the metal-hydrogen binding energies are estimated, we can use the adsorption energies we calculated to find a function which describes the trend of hydrogen adsorption on the Fe(100) surface. We can least squares fit this function to the calculated data for hydrogen adsorption. This function will then be used to describe the adsorption energy of hydrogen as a function of surface coverage. We considered three possible fitting functions: a tangens hyperbolicus function (*tanh*), an inverse tangent function (*arctan*) and an adapted hyperbola function (*hyperbolic*). A summary of the considered possible fitting functions and their fitted parameters are given in Table 3.3. The quality of the various fits can be seen in Figure 3.3.

In the case of the second assumption, the behaviour of hydrogen on the surface must lie somewhere between being in a covalently, site-bound state and a two di-

Table 3.3: Summary of function fitting parameters for the interpolation of H adsorption energies. Resulting binding energies ($|E_{bind,H}|$) from these functions are in kcal/mol.

	<i>tanh</i> fit	<i>arctan</i> fit	<i>hyperbolic</i> fit
	$A + B \tanh(C + D\theta)$	$A + B \arctan(C + D\theta)$	$\frac{1}{2}[A\theta + B + C\theta + D - \sqrt{(A\theta + B - C\theta - D)^2 + 4\beta}]$
A	54.493	54.667	-0.432
B	5.593	-4.247	60.033
C	2.823	-3.917	-7.167
D	-1.523	2.133	67.756
α			0.005
β			$\alpha\sqrt{(1 + A^2)(1 + C^2)}$

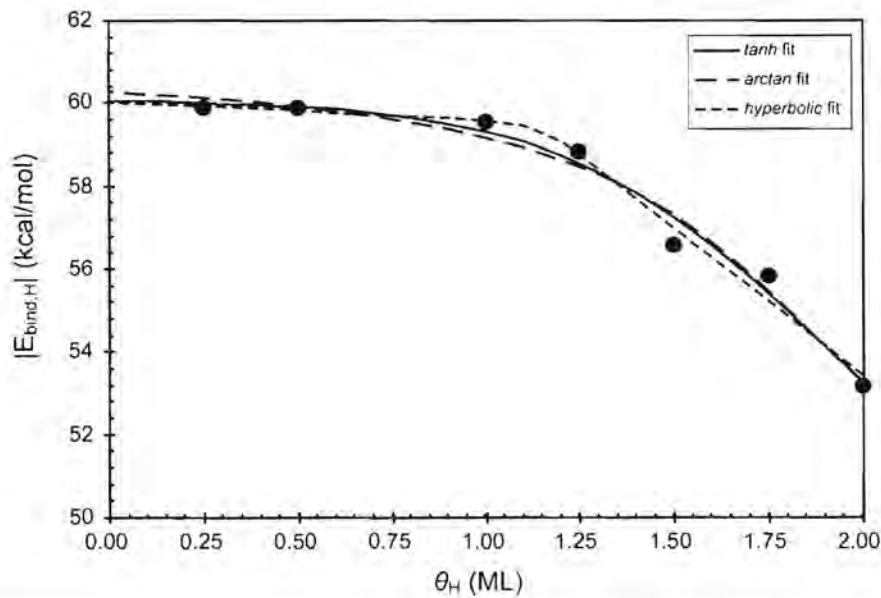


Figure 3.3: Interpolation of the calculated atomic binding energies of hydrogen ($|E_{bind,H}|$) on Fe(100) by using various fitting functions.

dimensionally delocalised quantum surface gas. Faglioni and Goddard presented three models to describe this system.

In the *ideal surface gas* model the hydrogen is regarded as a two-dimensional ideal surface gas. This approach should be correct when the temperature is very high and the coverage is low. In the *hard-disk surface gas* model exclusion interactions between the surface hydrogen atoms are included. This is done by considering the surface phase as a mixture of 'disks' of specific radii. This should help in the description of saturation effects. Faglioni and Goddard expect this model to correctly describe the surface hydrogen's behaviour at high temperatures and high coverage. The third model they propose is the *anchored* model. The individual hydrogen atoms are considered to be anchored to their surface sites. The low temperature limit should be described by this model. The full derivation of these models can be found in the original paper [34], while the following equations represent the summary of these three models:

Ideal surface gas:

$$P_{H_2}^{ideal} = k_B T \left(\frac{q_g}{V} \right) \left(\frac{e^{\theta \Lambda^2 |N_s|} - 1}{q_v} \right)^2 e^{-\frac{2F(\theta)}{RT}} \quad (3.4)$$

with

$$q_v = \frac{1}{1 - e^{h\nu/k_B T}} \quad (3.5)$$

$$\Lambda = (h^2/2\pi m_H k_B T)^{1/2} \quad (3.6)$$

$$F(\theta) = E(\theta) + \theta \frac{dE(\theta)}{d\theta} \quad (3.7)$$

Hard-disk surface gas:

$$P_{H_2}^{hard} = P_{H_2}^{ideal} \left(\frac{e^{\theta/(\theta_M - \theta)}}{(1 - \theta/\theta_M)^2} \right) \quad (3.8)$$

Anchored:

$$P_{H_2}^{anch} = P_{H_2}^{ideal} \left(\frac{1}{(1 - \theta/\theta_M)^2} \right) \quad (3.9)$$

where $P_{H_2}^{ideal}$ is the equilibrium gas pressure, k_B is the Boltzmann constant, h the Planck constant, m_H is the mass of hydrogen, R the ideal gas constant, T the temperature, N_s is the number of surface metal per unit area, q_g the full hydrogen gas partition function, q_v is the adsorbed atom vibrational partition function, θ is the surface coverage, θ_M is the maximum possible value of θ ; $E(\theta)$ is the adsorption energy function relative to the gas phase hydrogen molecule and Λ is the De Broglie wavelength for hydrogen.

From these models we can obtain the predicted surface coverage as a function of temperature and pressure by solving the coverage in the equilibrium condition equations (equations 3.4, 3.8 and 3.9).

A value of 2 ML was used for θ_M which would be large enough to ensure that the curvature of the fitted adsorption energy function would determine the saturation coverage. The resulting predicted equilibrium surface coverages for the various models and fits can be seen in Figure 3.4. These are represented by plots of the hydrogen surface coverage as a function of the temperature, with each line representing a different pressure value.

If we first consider the *hyperbolic* fit models in Figure 3.4 (a – c), we see that they are quite similar. The first similarity is that these models all predict the 100 K saturation coverage to be approximately 1.15 ML. This corresponds rather well to the value proposed from TPD experiments (1 ± 0.1 ML) [7]. It can also be seen that all of the *hyperbolic* fit models have a very similar dependence on pressure. The only difference lies at temperatures higher than 650 K where the hydrogen coverage in (b) decreases much sharper than in (a) and (c). In this figure (b) represents the *hard-disk surface gas* model which is supposed to best describe the high temperature and high coverage limit.

Considering the *tanh* fit and the *atan* fit results we find that these two interpolation fits give the same results for hydrogen. We therefore discuss only the *tanh* fit results (d – f in in Figure 3.4). All three these models are once again quite similar, although they differ quite a bit from that of the *hyperbolic* fit. The first similarity between the *tanh* fit models is that they all predict a slightly larger 100 K saturation coverage (between 1.0 and 1.25 ML depending on the pressure). This is still in range with the experimental value [7]. The most prominent feature of these models is the steeper dependence of the coverage on temperature in the higher pressure ranges. Once again the main difference between these three models lie at temperatures higher than 650 K. Here the hydrogen coverage in (e) has a slightly sharper decrease than that of models (d) and (f).

By comparing the two model fits it is clear that the applied interpolation fit plays a very large role. This can be seen in the fact that by changing the interpolation fits we see a larger change in shape of the equilibrium functions than by changing the surface adsorbate model limits. The applied interpolation fit seems to largely determine the low temperature saturation coverage value, as well as the nature of the high coverage pressure dependence. A very interesting feature of all the models is that they predict the same surface coverage dependence below $\theta_H = 0.3$ ML.

It is interesting to note that, although these plots cannot be directly compare to TPD

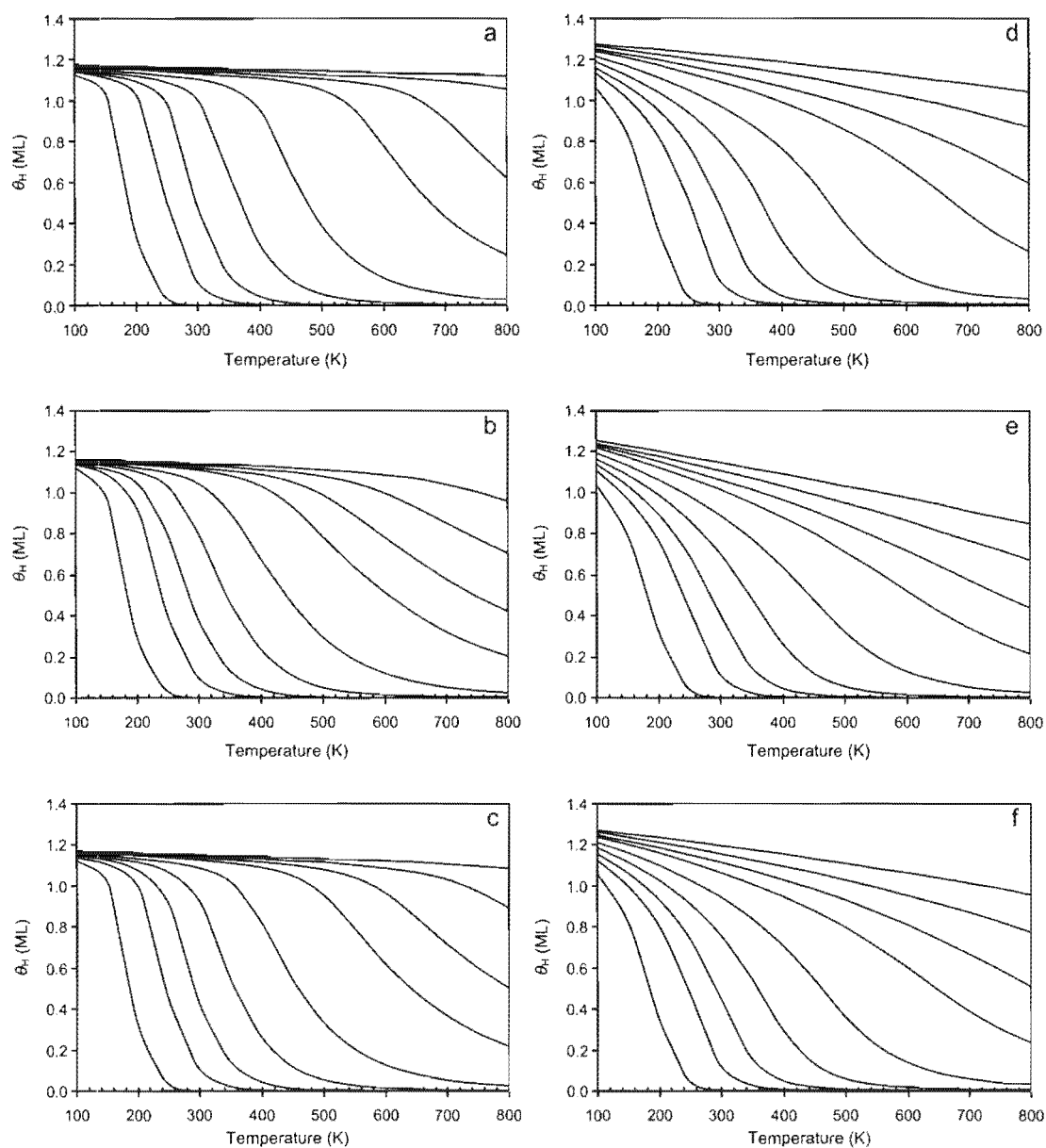


Figure 3.4: The predicted equilibrium surface hydrogen coverage (θ_H) as a function of the temperature using various combinations of interpolation fits and models. *hyperbolic-fit:* a) *ideal surface gas*, b) *hard-disk* and c) *anchored*. *tanh-fit:* d) *ideal surface gas*, e) *hard-disk* and f) *anchored*. Each isobar corresponds to one of the following pressures: 10^{-14} (lower, leftmost line), 10^{-10} , 10^{-8} , 10^{-6} , 10^{-4} , 10^{-2} , 10^{-1} , 1, and 10 bar (upper, rightmost line).

results, the derivatives of these model plots could be considered to relate to the hydrogen TPD peaks produced with an infinitely slow heating rate. The problem with such a view is the fact that the TPD peak produced in such a fashion does not include the effects of the specific adsorption/desorption pathway barriers (which will increase the peak temperature), specific coverage dependent ordered overlayer structures and site differences. Another consideration is that the peak temperature in TPD increases with an increase in the heating rate. Even with these considerations kept in mind it can be remarked that the lower left-most line in each plot should roughly correspond to the UHV conditions in a TPD experiment. The resulting pseudo-TPD peak temperature we obtain from the derivatives of our models are at approximately 200 K. This is much lower than the first expected TPD peak on Fe(100) of 280 K [7]. Although this is only a rough indication, it shows that our pseudo-TPD peak temperatures are somewhat on the low side. We found that these pseudo-TPD peak temperatures are extremely sensitive to the calculated low coverage binding energies. This discrepancy might indicate that our calculated model hydrogen binding energies might be slightly lower than those of hydrogen in the real system. We can therefore expect that the representations of the equilibrium surface coverage of hydrogen in the real system might be shifted to slightly higher temperatures.

The above mentioned slight mismatch is actually only of great importance at low pressures and low temperatures. If we now consider the relevant Fischer-Tropsch temperatures and pressures ($500 \text{ K} < T < 650 \text{ K}$ and $P > 1 \text{ bar}$) we can see that θ_H is at least 1 ML in all cases. This will stay the same even if there is a shift to slightly higher temperatures. This indicates that at realistic Fischer-Tropsch conditions the hydrogen adsorption equilibrium is strongly shifted toward saturation coverage on this surface. At these conditions there is therefore a strong driving force towards covering the whole surface with hydrogen.

3.4.2 CO equilibrium surface coverage

Since the critical temperature and pressure of CO are 133 K and 35 bar respectively [35], we can also consider CO to behave like an ideal gas under in Fischer-Tropsch conditions. This allows us to draw up an equilibrium coverage model for CO in a similar fashion as Faglioni and Goddard [34] did for hydrogen (*vide supra*). The full derivation is given in Appendix B. We used the same assumptions as those for hydrogen. The resulting equations for the CO equilibrium coverage is:

Ideal surface gas:

$$P_{CO}^{ideal} = k_B T \left(\frac{q_g}{V} \right) \left(\frac{e^{\theta \Lambda^2 |N_s|} - 1}{q_\nu} \right) e^{-\frac{F(\theta)}{RT}} \quad (3.10)$$

with

$$q_\nu = \frac{1}{1 - e^{h\nu/k_B T}} \quad (3.11)$$

$$\Lambda = (h^2/2\pi m_{CO} k_B T)^{1/2} \quad (3.12)$$

$$F(\theta) = E(\theta) + \theta \frac{dE(\theta)}{d\theta} \quad (3.13)$$

Hard-disk surface gas:

$$P_{CO}^{hard} = P_{CO}^{ideal} \left(\frac{e^{\theta/(\theta_M - \theta)}}{(1 - \theta/\theta_M)} \right) \quad (3.14)$$

Anchored:

$$P_{CO}^{anch} = P_{CO}^{ideal} \left(\frac{1}{(1 - \theta/\theta_M)} \right) \quad (3.15)$$

where P_{CO}^{ideal} is the equilibrium gas pressure, k_B is the Boltzmann constant, h the Planck constant, m_{CO} is the mass of CO, R the ideal gas constant, T the temperature, N_s is the number of surface metal atoms per unit area, q_g the full hydrogen gas partition function, q_ν is the adsorbed atom vibrational partition function, θ is the surface coverage, θ_M is the maximum possible value of θ , $E(\theta)$ is the adsorption energy function relative to the gas phase CO molecule and Λ is the De Broglie wavelength for CO.

We used the same three functions to fit the interpolation of the CO adsorption energies as we used for the hydrogen model. A summary of the fitting parameters can be seen in Table 3.4. The quality of the correspondence of these respective fitting functions to the data can be seen in Figure 3.5. From these models we can obtain the predicted CO surface coverage as a function of temperature and pressure by solving the coverage in the equilibrium condition equations.

For the *hard-disk* and *anchored* models we used a value of $\theta_M = 1$ ML. This would be large enough to ensure that the curvature of the fitted adsorption energy function would determine the saturation coverage. The resulting predicted equilibrium surface coverages for the various models and fits can be seen in Figure 3.6, with the CO surface coverage as a function of the temperature. Within these models the various surface adsorbate models (*ideal*, *hard-disk* and *anchored*) essentially gave the same results. The only noticeable difference is due to the applied adsorption energy interpolation fit and therefore we only compare the results of the three applied interpolation fits.

In the *hyperbolic* fit results ((a) in Figure 3.6) it is clear that the saturation coverage at 300 K varies quite a lot, with values ranging between 0.5 and 0.8 ML depending on

Table 3.4: Summary of function fitting parameters for the interpolation of CO adsorption energies. Resulting binding energies ($|E_{bind,CO}|$) from these functions are in kcal/mol.

	<i>tanh</i> fit	<i>arctan</i> fit	<i>hyperbolic</i> fit
	$A + B \tanh(C + D\theta)$	$A + B \arctan(C + D\theta)$	$\frac{1}{2}[A\theta + B + C\theta + D - \sqrt{(A\theta + B - C\theta - D)^2 + 4\beta}]$
<i>A</i>	33.531	33.516	0.133
<i>B</i>	10.320	8.202	43.281
<i>C</i>	2.679	3.762	-29.586
<i>D</i>	-3.584	-5.028	55.689
α			0.005
β			$\alpha \sqrt{(1 + A^2)(1 + C^2)}$

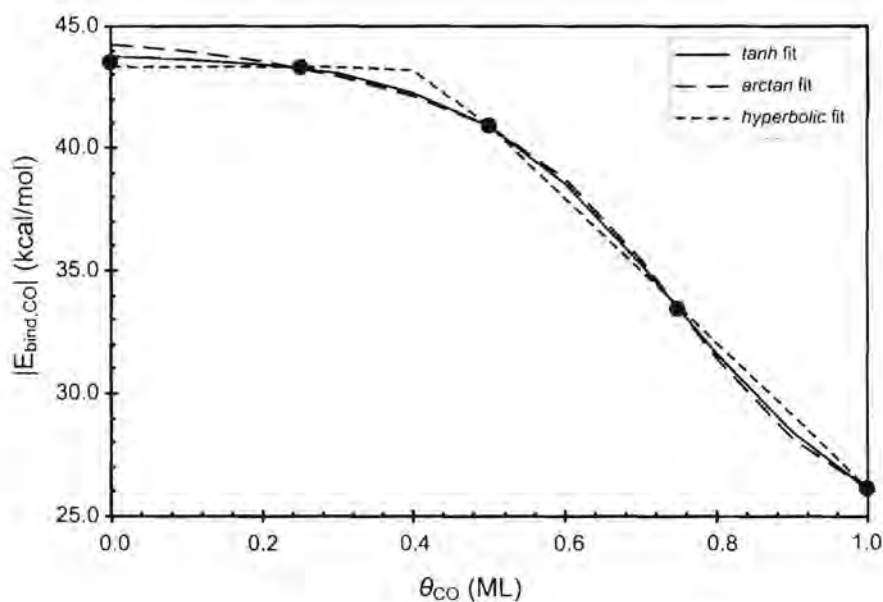


Figure 3.5: Interpolation of the calculated molecular binding energies of CO ($|E_{bind,CO}|$) on Fe(100) by using various fitting functions.

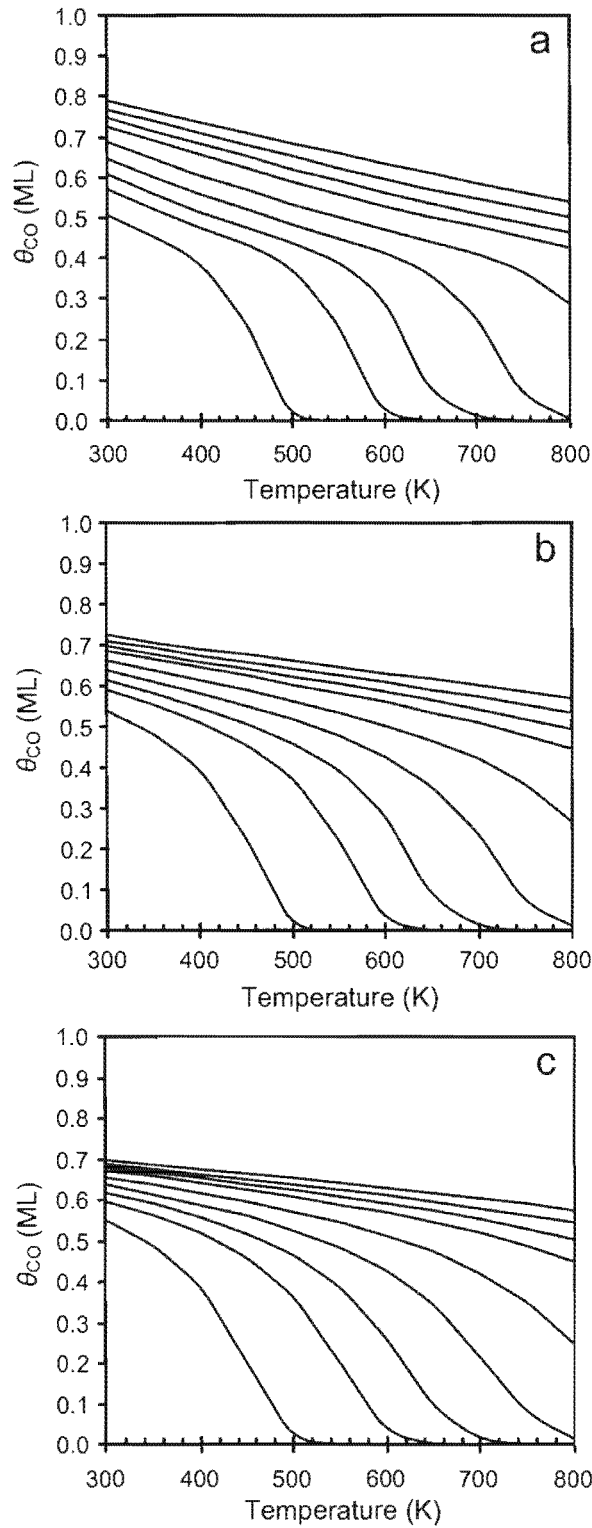


Figure 3.6: The predicted equilibrium CO surface coverage (θ_{CO}) as a function of the temperature using the proposed interpolation fits: a) *hyperbolic*-fit, b) *tanh*-fit and c) *atan*-fit. Each isobar corresponds to one of the following pressures: 10^{-14} (lower, leftmost line), 10^{-10} , 10^{-8} , 10^{-6} , 10^{-4} , 10^{-2} , 10^{-1} , 1, and 10 bar (upper, rightmost line).

the pressure. The lowest considered pressure value corresponds to the experimental estimate of 0.58 ML from TPD [7] and 0.5 from XPS [36]. At all the pressure values we see a nearly linear decrease of coverage with increasing temperature down to 0.45 ML. After this value we observe a steeper decrease in the CO coverage. What is clear is that in the relevant Fischer-Tropsch range ($500 \text{ K} < T < 650 \text{ K}$ and $P > 1 \text{ bar}$) the surface coverage is larger than 0.5 ML. It is also interesting to note that the CO coverage never reaches 1 ML at the considered pressures.

If we consider the *tanh* fit we see that the saturation coverages at 300 K still varies quite a lot, but not as much as in (a). The 300 K coverage values ranges from between 0.53 and 0.73 ML depending on the pressure. This is also roughly within range of the experimental values. At all the pressure values we see a nearly linear decrease in the CO coverage, but not nearly as steep as in (a). Below 0.4 ML we see a similar CO coverage dependence on temperature as in (a).

If we consider the *atan* fit we see that the saturation coverage at 300 K does not vary as much as in (a) or (b). The 300 K coverage values ranges from between 0.55 and 0.7 ML depending on the pressure. This is well in line with the experimental values. Once again we see that at all the pressure values we have a nearly linear decrease in the CO coverage at high pressures. Below 0.4 ML we see a similar CO coverage dependence on temperature as in (a) and (b).

When calculating the pseudo-TPD peak value from the derivatives of these figures at the lowest pressure value, we find a very broad peak with a maximum at a temperature of 450 K. This corresponds quite well to the α_3 TPD peak observed by Burke and Madix at 425 K [7]. This view cannot account for specific overlayer adsorbate structures which Burke and Madix clearly observed at lower temperatures. The broadness of our pseudo-TPD peak is probably accounting for the average adsorption energy of these states. This indicates that a more step-like interpolation function would be needed to simulate these states.

Another factor which must be considered in the Fischer-Tropsch temperature range is that the tilted CO molecules on Fe(100) can readily dissociate upon heating to above 400 K [37, 38]. This dissociation will result in atomic C and O on the surface. We must therefore be careful when drawing conclusions from these molecular adsorption equilibrium plots.

From these CO adsorption equilibrium plots it is clear that at realistic Fischer-Tropsch conditions the molecular CO adsorption equilibrium is strongly shifted towards saturation coverage on this surface. There is therefore a strong driving force towards having CO at saturation coverage on the surface at Fischer-Tropsch conditions. At pressures larger than 1 bar this saturation corresponds to a value of between 0.5 and

0.65 ML. This shows that there will be some "empty sites" available between the CO molecules due to the CO lateral interaction.

3.5 Conclusions

We have calculated the separately adsorbed hydrogen and CO geometries by using the RPBE function. For hydrogen we considered adsorption structures ranging from $\theta_H = 0.25$ ML to $\theta_H = 2.00$ ML with the hydrogen atoms in the hollow sites and on the bridge sites being stable with regard to the gas phase H_2 . We found that at hydrogen surface coverages higher than $\theta_H = 1.00$ ML the average hydrogen adsorption energy decreases monotonously with an increase in coverage. At $\theta_H = 2.00$ ML the adsorption energy is almost iso-energetic with the gas phase.

We also calculated CO adsorption geometries similar to those calculated by Bromfield et al. [22] using the PW91 exchange-correlation functional. Although our calculated geometries are very similar, we showed that by using the RPBE exchange-correlation functional we obtain CO adsorption energy values which are much closer to the experimental values than the overestimated values of Bromfield et al. [22].

To be able to consider the separate adsorption of hydrogen at relevant Fischer-Tropsch conditions ($500 \text{ K} < T < 650 \text{ K}$ and $P > 1 \text{ bar}$), we used a statistical thermodynamic model [34] in which we used our calculated hydrogen adsorption values. We used the resulting models to consider the equilibrium surface of hydrogen at a large range of temperatures and pressures. From these models we can conclude that at the relevant Fischer-Tropsch conditions there will be a strong driving force to fill up the Fe(100) surface with hydrogen. This would correspond to a hydrogen coverage of around $\theta_H = 1.00$ ML.

We derived a similar statistical thermodynamic model for the equilibrium surface coverage of CO. From the resulting models we conclude that at Fischer-Tropsch conditions the CO adsorption equilibrium is shifted towards saturation coverage. This saturation coverage value lies between 0.5 and 0.65 ML at pressures larger than 1 bar. This saturation coverage of CO that is lower than that of hydrogen can be ascribed to the large CO lateral interactions that exist at coverages larger than $\theta_{CO} = 0.5$ ML. At Fischer-Tropsch conditions we expect that almost half of the hollow sites will still be open. The possibility therefore exists that the small hydrogen atoms might be able to mix with the CO upon coadsorption. This will be further explored in chapter 5.

Bibliography

- [1] Ertl, G. *Journal of Vacuum Science and Technology A* **1983**, 1(2), 1247–1253.
- [2] Dry, M. E. *Catalysis Today* **2002**, 71, 227–241.
- [3] Reuel, R. C.; Bartholomew, C. H. *Journal of Catalysis* **1984**, 85, 63–77.
- [4] Boszo, F.; Ertl, G.; Grunze, M.; Weiss, M. *Applications of Surface Science* **1977**, 1, 103–119.
- [5] Juan, A.; Hoffmann, R. *Surface Science* **1999**, 421, 1–16.
- [6] Hammer, L.; Landskron, H.; Nichtl-Pecher, W.; Fricke, A.; Heinz, K.; Muller, K. *Physical Review B* **1993**, 47(23), 15969–15972.
- [7] Burke, M. L.; Madix, R. J. *Surface Science* **1990**, 237, 20–34.
- [8] Sorescu, D. C. *Catalysis Today* **2005**, 105, 44–65.
- [9] Clum, J. A. *Scripta Metallurgica* **1975**, 9, 51–58.
- [10] Gangloff, R. P.; Wei, R. P. *Metallurgical Transactions A* **1977**, 8, 1043–1053.
- [11] Blyholder, G. *The Journal of Physical Chemistry* **1964**, 68(10), 2772–2778.
- [12] Van Santen, R. A.; Neurock, M. *Catalysis Reviews, Science and Engineering* **1995**, 37(4), 557–698.
- [13] Chen, Y.-H.; Cao, D.-B.; Jun, Y.; Li, Y.-W.; Wang, J.; Jiao, H. *Chemical Physical Letters* **2004**, 400, 35–41.
- [14] Aizawa, H.; Tsuneyuki, S. *Surface Science* **1999**, 399, L364–L370.
- [15] Föhlisch, A.; Nyberg, M.; Bennich, P.; Triguero, L.; Hasselström, J.; Karis, O.; Pettersson, L. G. M.; Nilsson, A. *Journal of Chemical Physics* **2000**, 112(4), 1946–1958.
- [16] Sung, S.-S.; Hoffmann, R. *Journal of the American Chemical Society* **1985**, 107, 578–584.
- [17] Cao, D.-B.; Zhang, F.-Q.; Li, Y.-W.; Jiao, H. *The Journal of Physical Chemistry B* **2004**, 108, 9094–9104.
- [18] Stibor, A.; Kresse, G.; Eichler, A.; Hafner, J. *Surface Science* **2002**, 507–510, 99–102.
- [19] Jiang, D. E.; Carter, E. A. *Surface Science* **2004**, 570, 167–177.
- [20] Nayak, S. K.; Nooijen, M.; Bernasek, S. L.; Blaha, P. *The Journal of Physical Chemistry B* **2001**, 105, 164–172.
- [21] Sorescu, D. C.; Thompson, D. L.; Hurley, M. M.; Chabalowski, C. F. *Physical Review B* **2002**, 66, 035416/1–035416/13.
- [22] Bromfield, T. C.; Curulla Ferré, D.; Niemantsverdriet, J. W. *ChemPhysChem* **2005**, 6, 254–260.
- [23] Lu, J.-P.; Albert, M. R.; Bernasek, S. L. *The Journal of Physical Chemistry* **1990**, 94, 6028–6033.
- [24] Moon, D. W.; Bernasek, S. L.; Dwyer, D. J.; Gland, J. L. *Journal of the American Chemical Society* **1985**, 107, 4363–4364.
- [25] Moon, D. W.; Dwyer, D. J.; Bernasek, S. L. *Surface Science* **1985**, 163, 215–229.
- [26] Wedler, G.; Colb, K. G.; McElhiney, G.; Heinrich, W. *Applications of Surface Science* **1978**, 2, 30–42.
- [27] Segall, M. D.; Lindan, P. J. D.; Probert, M. J.; Pickard, C. J.; Hasnip, P. J.; Clark, S. J.; Payne,

- M. C. *Journal of Physics: Condensed Matter* **2002**, *14*, 2717–2744.
- [28] Hammer, B.; Hansen, L. B.; Nørskov, J. K. *Physical Review B* **1999**, *59*(11), 7413–7421.
- [29] *MS Modeling 4*; Accelrys Software Inc., <http://www.accelrys.com>.
- [30] Monkhorst, H. J.; Pack, J. D. *Physical Review B* **1976**, *13*(12), 5188–5192.
- [31] Jiang, D. E.; Carter, E. A. *Physical Review B* **2004**, *70*, 064102.
- [32] Merrill, P. B.; Madix, R. J. *Surface Science* **1996**, *347*, 249–264.
- [33] Saiki, R. S.; Herman, G. S.; Yamada, M.; Osterwalder, J.; Fadley, C. S. *Physical Review Letters* **1989**, *63*(3), 283–286.
- [34] Faglioni, F.; Goddard III, W. A. *Journal of Chemical Physics* **2005**, *122*, 014704.
- [35] Lide, D. R., Kehiaian, H. V., Eds. *CRC Handbook of Thermophysical and Thermochemical Data*; CRC Press: Boca Raton, FL, 1994.
- [36] Benziger, J.; Madix, R. J. *Surface Science* **1980**, *94*, 119–153.
- [37] Moon, D. W.; Bernasek, S. L.; Lu, J.-P.; Gland, J. L.; Dwyer, D. *Surface Science* **1987**, *184*, 90–108.
- [38] Cameron, S. D.; Dwyer, D. J. *Langmuir* **1988**, *4*, 282.

Chapter 4

Hydrogen dissociation on CO and C precovered surfaces

Alle Ding sind Gift, und nichts ohn Gift; allein die Dosis macht, daß ein Ding kein Gift ist.

— PARACELSUS

4.1 Introduction

STUDIES of the process of hydrogen adsorption on iron surfaces have been motivated by the importance of this process in the field of heterogeneous catalysis. This is the case since hydrogen adsorption is one of the first reactions in the representation of various catalytic cycles. This can further be seen in its particular application in the ammonia synthesis [1] and Fischer-Tropsch synthesis reactions [2].

Although the hydrogen dissociation reaction seems to be a simple reaction, it has quite a lot of intricacies. In the first step in the process of hydrogen chemisorption on a metal surface, the H_2 molecule approaches the surface. As this happens the electrons in the filled $1\sigma_g$ orbital start to overlap with that of the metal surface. This results in a Pauli repulsion with the accompanying increase in energy. As the H_2 comes even closer, the empty anti-bonding $1\sigma_u^*$ orbital becomes partially occupied, weakening the H-H bond slightly. As all of this happens, new strong chemical bonds start to form with the surface which also counteracts the Pauli repulsion. The specific point at which this counteraction takes place determines the position of the barrier on the hydrogen adsorption potential energy surface (PES) [3]. This interaction of attractive and repulsive potentials will differ at different sites on the metal surface. It will also depend on the orientation of the hydrogen molecule. The dissociation activation en-

ergy barrier height can therefore differ at various sites. These different values can dynamically "steer" the approaching hydrogen molecule to a more favourable site for dissociation [4]. Other effects that has been noted to play a role in certain cases are quantum tunnelling and zero-point effects [5].

The study of hydrogen chemisorption on a clean Fe(100) surface has been the focus of a number of studies [6–10]. On the Fe(110), Fe(100) and Fe(111) surfaces hydrogen undergoes dissociative chemisorption [6]. On the clean Fe(100) two adsorption sites β_1 and β_2 have been identified. It was by TPD shown that the β_2 activation energy of desorption is 23 kcal/mol (1.00 eV) [7]. The desorption activation energy of β_1 site has been established as 14.1 kcal/mol (0.74 eV) [8]. It was also proposed that the Fe-H bond energy has a lower limit of 59 kcal/mol [7]. From theoretical work it has been established that the four-fold hollow and the bridge sites are available hydrogen adsorption sites with the four-fold hollow site as the slightly more favourable adsorption site [9]. By use of the PW91 functional the classical adsorption barrier on the on top site was calculated at 3.6 kcal/mol (0.16 eV) and over the bridge site at 3.48 kcal/mol (0.15 eV) [9]. From molecular beam experiments the value for H₂ dissociation barrier was estimated at 0.45 eV [10]. In contrast to this Burke and Madix have proposed an upper limit to the adsorption activation barrier of about 2 kcal/mol (0.01 eV) which corresponds to a sticking probability of $s_0 = 0.05$ [7].

This picture might change significantly once other adsorbates are present on the surface. In this regard Ko and Madix [11] showed that the presence of either carbon or oxygen hindered the dissociative adsorption of hydrogen on Mo(100). When a clean surface is therefore modified with a preadsorbed species it can have an effect on the dissociation of hydrogen. Various explanations has been put forward for this type of "poisoning". Feibelman and Hamann [12, 13] proposed that this effect is due to an adsorbate induced change of the Fermi level density of states (DOS). Nørskov et al. [14] proposed a slightly different model for the poisoning. They proposed that the change in reactivity by an adlayer is due to the interaction of the hydrogen molecule with the electrostatic field that is induced by the adlayer. For dissociative hydrogen adsorption they predict that electronegative adlayers are usually poisons for hydrogen dissociation and that electropositive adlayers are promoters for hydrogen dissociation.

These models show that C and CO adsorbates can be poisons, but they do not give a detailed microscopic description of the hydrogen dissociation process in their presence. Local effects can occur by increased dissociation barriers along specific dissociation pathways of the hydrogen molecule or simply by the blocking adsorption sites for atomic hydrogen.

Examples of these effects are the simultaneous blocking of adsorption sites and the

increase of dissociation barriers on a sulphur precovered Pd(100) surface [15]. Sulphur can increase the dissociation barrier at a low S coverage by changing the Pd electronic structure, but when the hydrogen molecule is less than 1.5 Å away from the S, the main contribution is the blockage of the adsorption site due to a strong S-H repulsion.

In this chapter we use density functional theory (DFT) to calculate the potential energy surface (PES) for the H₂ dissociation process on the Fe(100) surface. We consider the dissociation process on various high symmetry sites in the p(2×2) surface unit cell on a clean surface. Since two other species that will be present on the surface in the Fischer-Tropsch process are CO and C, we also consider these adsorbate precovered surfaces at various coverages. We discuss the most important PES profiles and discuss the various effects that play a role in the adsorption of hydrogen on these precovered Fe(100) surfaces.

4.2 Methods and models

4.2.1 Calculational setup

All the calculations in this study were performed using the CASTEP [16] code. This code employs periodic DFT calculations with a plane wave basis set and pseudopotentials. We used the generalized gradient approximation (GGA) with the Revised Perdew Burke Ernzerhof (RPBE) functional [17]. The electron distribution at the Fermi level was modelled by a Gaussian smearing method with $\sigma = 0.1$ eV. The ion-electron interactions were described by core corrected ultrasoft pseudopotentials as included in the CASTEP suite [18].

A five-layer Fe(100) slab was used with an optimised 17 Å vacuum layer between the surfaces. This large vacuum spacing ensures that when the hydrogen molecule is sufficiently far away from the surface it will have no significant interaction with either side of the surface slab. The surface was represented by using a p(2×2) periodic supercell. The k-point sampling was generated by following the Monkhorst-Pack [19] procedure with a 4×4×1 mesh. The plane wave basis set cutoff energy was set at 400 eV. The coordinates of the slab (as well as the preadsorbed CO and C) were fully optimized before the hydrogen molecule was introduced into the cell. The calculational setup parameters (the k-points mesh, the number of slab layers, the vacuum spacing, etc.) were tested and optimised.

We calculated the equilibrium lattice constant for bulk iron at 2.852 Å with a bulk modulus of 176 GPa using the Birch-Murnaghan equation of state [20, 21]. A magnetic moment of 2.31 μ_B per iron atom was also calculated. These values are in good agree-

ment with the experimental values of 2.86 Å, 168 GPa and 2.24 μ_B [22, 23]. The calculated surface energy of the seven-layer slab was 2.36 J.m⁻² which is in good agreement with the experimental value of 2.41 J.m⁻² [24].

The energy and properties of the gas phase hydrogen molecule was calculated by placing the molecule in a cubic unit cell with 10 Å sides. For H₂ we obtained a equilibrium bond distance of $r_e = 0.749$ Å, a vibrational frequency of $\nu = 4421$ cm⁻¹ and a dissociation energy of $D_e = 4.564$ eV. These values are in good agreement with the experimental values ($r_e = 0.741$ Å, $\nu = 4401$ cm⁻¹ and $D_e = 4.560$ eV) [25].

4.2.2 Dissociation model

The full description of a H₂ molecule approaching the surface has six dimensions (X, Y and Z coordinates of the centre of mass, the H₂ interatomic distance and the polar (θ) and azimuthal (ϕ) angles of the molecular axis). To fully calculate this large calculational space will be immensely time consuming and therefore we had to simplify our approach. We only considered specific 2D cuts through this 6D surface. The two dimensions under consideration are the H₂ interatomic distance and the height of the centre of mass above the surface (Z). On various Cu [26–29], Pd [4, 30–32], Ag [32] and Rh [32, 33] surfaces H₂ dissociation is enhanced by having the H₂ molecular axis parallel to the surface. The proposed mechanism that underlies this H₂ rotational orientation effect is the enhanced metal-H₂ interaction when both the H atoms are bound to the metal surface atoms at the same time. Therefore, as a first approach we assume that, although Fe is in many respects different to these metals, in a similar fashion the interaction of the H₂ with the molecular axis parallel to the surface will be of the most significance in the H₂ dissociation process on the Fe(100) surface.

The surface slab geometry was kept fixed for all of the studied H₂ adsorption pathways. This approximation can be used since the mass mismatch of H with the Fe atoms is quite large (the mass mismatch between H₂ and CO/C is not that prominent and therefore their movements cannot necessarily be so cleanly decoupled. However, to simplify the calculational space it is assumed that we can decouple the CO/C and H₂ movements). The reference energy zero is taken as the energy of the geometry where the hydrogen molecule is 4.00 Å away from the surface. Single point energies were calculated for a large range of possible combinations of the height of the H₂ above the surface and the H₂ bond length. An interpolation of the energy values were done, resulting in a classical "elbow plot" graphs. Each plot is constructed from a set of approximately 240 single point calculations with an average grid spacing of 0.1 Å. All iso-energetic lines in these graphs are 0.1 eV apart. Zero-point corrections are not

included in the PES, but will be considered separately.

4.2.3 Zero-Point Corrections

It is important to consider the effect zero-point energies have on the barrier height, since it has been shown that it is one of the quantum effects for the dissociation of H₂ [30]. A classical particle can follow the minimum-energy path of a PES exactly. A quantum particle is delocalised and cannot follow the bottom of the valley of the PES. It needs at least the zero-point energy perpendicular to the minimum energy pathway [5]. We therefore estimated the minimum zero-point energies for a specific PES by fitting the potential at various points to a Morse potential [34]. From this fit we obtain the zero-point vibrational frequency (ν_0) and the potential well depth (D_e). With h as the Plack constant, the zero-point energy (E_0) estimate is calculated by:

$$E_0 = \frac{1}{2}h\nu_0 - \frac{(\frac{1}{2}h\nu_0)^2}{4D_e} \quad (4.1)$$

4.2.4 DOS and Charge analysis

The electronic local density of states (LDOS) was calculated by a projection of the wavefunctions onto spherical harmonics to obtain the s, p and d character of the electrons. The DOS is given relative to the Fermi-level of each system. All the DOS-plots are shown as spin-polarised with the α -spin profile at the top and the β -spin profile at the bottom. We also estimated the charge of the preadsorbed C and CO on the surface by a Mulliken charge analysis [35, 36].

4.3 Results

We calculated the 2D cuts in the H₂ adsorption potential energy surface (PES) for a clean Fe(100) surface, as well as CO and C precovered surfaces. The adsorption potential energy surfaces will be described by following the minimum energy pathway. The H₂ molecule approaches the surface from 4 Å above the surface with an equilibrium bond length of 0.794 Å. A summary of all the activation barrier energies is given in Table 4.1

4.3.1 H₂ dissociation on the clean Fe(100) surface

The resulting H₂ dissociation profiles on a clean Fe(100) surface can be seen in Figure 4.1. The left of Figure 4.1 shows the dissociation profile of H₂ on the on top site

with H atoms ending up on the bridge sites. The H_2 approaches to 2.2 Å where it goes over a small barrier of 0.08 eV to enter a molecular adsorbed state at 1.8 Å above the surface. The H-H bond length is slightly stretched at 0.82 Å. The depth of the energy well of this molecularly adsorbed state is 0.03 eV. This is much smaller than the energy well calculated by Sorescu with PW91 [9]. The simultaneous H-H bond stretch and surface-H bond shortening results in an energy increase up to the dissociation activation energy barrier at 1.42 Å above the surface, with the H atoms separated at 1.25 Å and with an energy value of about 0.24 eV. This is much larger than the barrier calculated by Sorescu [9] for the same site. After inclusion of the ZPE correction for this profile the height of the dissociation barrier (0.16 eV) compares slightly better with Sorescu's values. After the barrier the H-H distance increases until the H atoms are bonded at the bridge site (2.85 Å separation) at a height of 0.95 Å above the surface. The adsorption energy of the 2 H atoms on the bridge site is -0.41 eV ($E_{ads} = -0.205$ eV per H atom).

The centre profile of Figure 4.1 shows the dissociation profile of H_2 on the on top site with the H-H bond rotated by 45° in the plane parallel to the surface. In this case the H atoms end up in the hollow sites. The H_2 approaches to 2.2 Å where it goes over a small barrier of 0.08 eV to enter a molecular adsorbed state at 1.8 Å above the surface with a slightly stretched H-H bond length at 0.81 Å. The depth of the energy well of this molecularly adsorbed state is also 0.03 eV. The dissociation barrier has an energy value of about 0.33 eV. The separation of the H atoms increases until they are bonded in hollow sites separated at 4.02 Å with a height of 0.30 Å above the surface. The adsorption energy of the 2 H atoms in these hollow sites is -0.59 eV ($E_{ads} = -0.30$ eV per H atom).

The right profile in Figure 4.1 shows the dissociation profile of H_2 on the bridge site with the H atoms ending up in the hollow sites. The H_2 approaches to 1.4 Å where it reaches a barrier of 0.34 eV with a slightly stretched H-H bond length at 0.85 Å. Only after this barrier the H-H bond starts to stretch significantly until they are both bonded in hollow sites at a height of 0.30 Å above the surface. The adsorption energy of the 2 H atoms in these hollow sites is -0.62 eV ($E_{ads} = -0.31$ eV per H atom).

We also considered the dissociation profile of H_2 over the hollow site with H atoms ending up on the bridge sites. As the H_2 approaches the surface it experiences a very strong repulsion. The barrier of 0.86 eV is reached at 1.25 Å above the surface with a slightly stretched H-H bond length at 0.83 Å.

4.3.2 H₂ dissociation on the CO-covered Fe(100) surface

Besides hydrogen, the other component in synthesis gas is CO. We considered the effect of adsorbed CO on the process of hydrogen adsorption by having CO perpendicularly adsorbed in the hollow site at coverages of $\theta_{CO} = 0.25$ ML and $\theta_{CO} = 0.5$ ML. We considered the same pathways as those described on the clean surface.

4.3.2.1 $\theta_{CO} = 0.25$ ML

The profiles for H₂ dissociation on a $\theta_{CO} = 0.25$ ML precovered surface can be seen in Figures 4.2 and 4.3. The left profile of Figure 4.2 shows the dissociation profile of H₂ on the on top site with H atoms ending up on the bridge sites. As the H₂ approaches the surface it experiences a much stronger repulsion than was seen for the corresponding pathway on a clean surface. This is due to the fact that the CO molecule orbitals are sticking out further into the vacuum. These CO orbitals contribute to a strong Pauli repulsion interaction with the H₂ at a very earlier stage in the H₂ approach. No molecular adsorbed state can be observed in this profile. The H-H bond stretches and the surface-H bond shortens with a corresponding increase of the energy to 1.46 eV at the dissociation barrier. After the barrier the H atoms are bonded at the bridge sites. The energy of the 2 H atoms is 0.94 eV at this point. This is much less stable than the gas phase. It is important to keep in mind that in this case the two H atoms are not equivalent. The one that is the closest to the CO molecule would probably experience severe forces that will move it down to the hollow site right next to it. This would result in a more favourable energetic configuration. At this CO coverage this seems to be a very unlikely dissociation pathway.

In contrast to the on top site, the dissociation barrier is slightly lower for the on top site with the H-H bond rotated by 45° parallel to the surface plane (right of Figure 4.2). In this case both the H atoms end up in hollow sites. As the H₂ approaches the surface it once again experiences a strong repulsion. No distinct molecular adsorbed state can be observed. The energy value of this activation barrier is 0.90 eV. This barrier is much higher than on a clean surface, but it is significantly lower than that of the previously considered on top site. The H atoms end up in hollow sites with an adsorption energy of the 2 H atoms of -0.72 eV ($E_{ads} = -0.36$ eV per H atom).

From the previous two profiles it is clear that there is a strong repulsion between the CO and the approaching H₂ molecule. We therefore also considered an adsorption profile similar to the on top site with the H-H bond rotated by 45°, but with the H₂ centre of mass shifted away from the CO by 0.5 Å. We call this the rotated *off-symmetry site*. This profile can be seen in Figure 4.3. It is clear that the CO-H₂ repulsion is

significantly smaller here. The initial repulsion is almost down to the level of the clean surface, with a dissociation barrier of 0.35 eV. This is in line with that of the clean surface.

We also considered the dissociation of H_2 on the bridge site which is not directly next to a CO. The H atoms end up in hollow sites. The H_2 reaches a barrier of 0.33 eV with a profile which looks exactly like that of the clean surface bridge site. Upon calculation the dissociation profile over the possible hollow sites, an even larger repulsion was experienced than that which was observed on the clean surface indicating that the barriers will be even higher than that of the clean surface hollow site.

4.3.2.2 $\theta_{CO} = 0.50$ ML

At this coverage all of the bridge sites will have a CO molecule in the hollow sites next to it. The strong repulsion between CO and H_2 will effectively block these bridge sites for adsorption. The dissociation barrier for a H_2 molecule on the on top site (with the H atoms ending up on the bridge sites) has an extremely high energy value of 2.67 eV. Similarly dissociation over the hollow sites and bridge sites cannot take place, since these bridge sites are blocked by the adsorbed CO molecules in the hollow sites.

Figure 4.4 shows the dissociation profile of H_2 on the on top site, with the H-H bond rotated by 45° parallel to the surface plane. In this case the H atoms end up in the two remaining hollow sites. The initial repulsion H_2 experiences as it approaches the surface is similar to that at $\theta_{CO} = 0.25$ ML. The dissociation barrier has an energy value of 1.33 eV. This barrier is significantly higher than the barriers for the corresponding geometries on the clean surface and at $\theta_{CO} = 0.25$ ML.

The most stable CO adsorption geometry on Fe(100) is the hollow site with the CO bond tilted towards the surface [37]. We have therefore also calculated the H_2 dissociation profile for this tilted CO geometry at $\theta_{CO} = 0.5$ ML on the on top site with the H-H bond rotated by 45° parallel to the surface plane. We found that the H_2 experiences an extremely large repulsion as it approaches the surface. The dissociation barrier in this case has an energy value of 2.46 eV. This barrier is a lot higher than that of the corresponding geometry with the CO molecular axis perpendicular to the surface. It is clear that when the CO is tilted on the surface at $\theta_{CO} = 0.50$ ML, dissociation would probably only take place if the CO molecules move to the perpendicular positions.

4.3.3 H_2 dissociation on the C-covered Fe(100) surface

It has been shown that the tilted CO molecules on Fe(100) can readily dissociate upon heating to above 400 K [38, 39]. This will result in atomic C and O on the surface. We

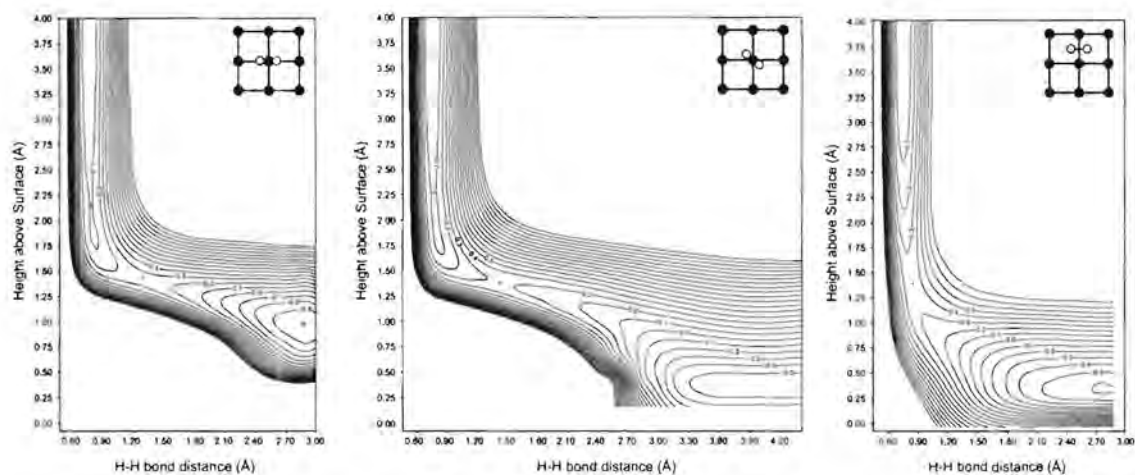


Figure 4.1: PES for H_2 dissociation on a clean Fe(100) surface with H_2 on top (left), on top rotated by 45° (centre) and on the bridge site (right).

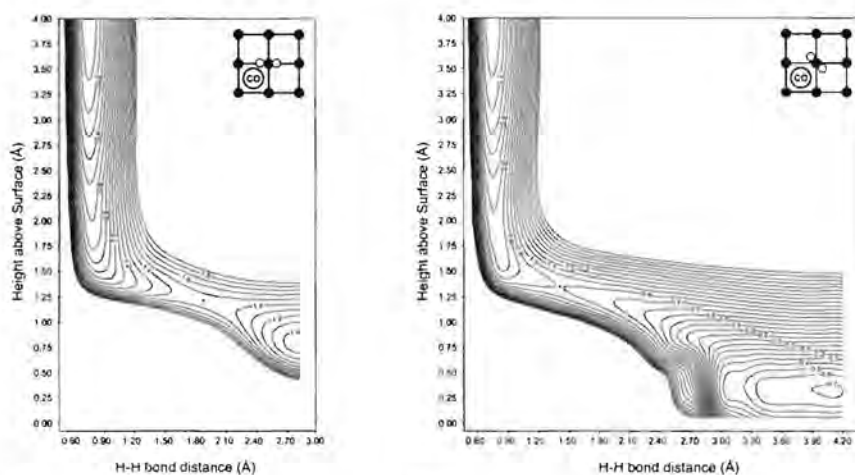


Figure 4.2: PES for H_2 dissociation on a $\theta_{CO} = 0.25$ ML precovered Fe(100) surface with H_2 adsorption on top (left) and on top rotated by 45° (right).

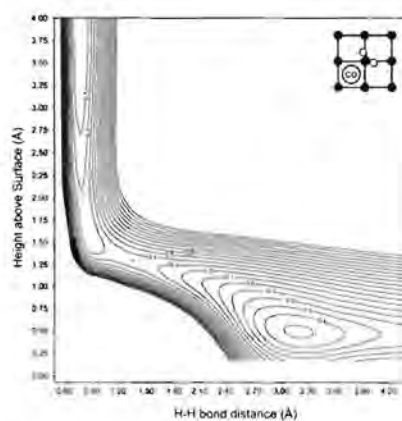


Figure 4.3: PES for H_2 dissociation on a $\theta_{CO} = 0.25$ ML precovered Fe(100) surface with H_2 rotated by 45° . The H_2 centre of mass is slightly moved away from the high symmetry on top site.

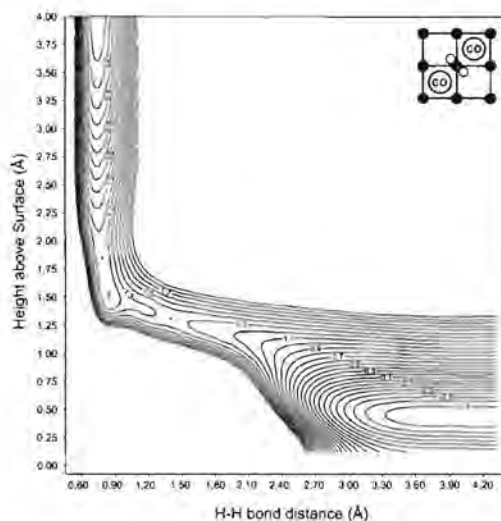


Figure 4.4: PES for H_2 dissociation on a $\theta_{CO} = 0.5$ ML precovered Fe(100) surface with H_2 on top and on top rotated by 45° .

therefore also need to consider the effect of a C precovered surface on H_2 dissociation.

4.3.3.1 $\theta_C = 0.25$ ML

The resulting H_2 dissociation profiles on Fe(100) surface with $\theta_C = 0.25$ ML can be seen in Figures 4.5 and 4.6. The left profile of Figure 4.5 shows the dissociation profile of H_2 on the top site with H atoms ending up on the bridge sites. As the H_2 approaches the surface it experiences a slightly stronger repulsion than that of the corresponding pathway on a clean surface, but not as strong as at $\theta_{CO} = 0.25$ ML. No molecular adsorbed state can be observed. The dissociation barrier has an energy value of 0.55 eV. This barrier is almost twice as high as on the clean surface, but much lower than at $\theta_{CO} = 0.25$ ML. Once again the two H atoms are not equivalent and the one that is the closest to the C atom will probably move down into the hollow site right next to it. This would result in a more favourable adsorption energy.

The profile in the right of Figure 4.5 shows the H_2 dissociation profile on the Fe(100) surface with $\theta_C = 0.25$ ML on the on top site with the H-H bond rotated by 45° parallel to the surface. In this case the H atoms end up in the unoccupied hollow sites. The H_2 approaches to 2.05 Å where it goes over a barrier of 0.16 eV to enter a molecular adsorbed state at 1.78 Å above the surface with a slightly stretched H-H bond length. The depth of the energy well of this molecularly adsorbed state is once again very shallow. The energy will increase up to the dissociation barrier with an energy value of 0.49 eV. Although this barrier is lower than that for the CO precovered surfaces, this value is still about twice as large as the lowest barrier on a clean Fe(100) surface (0.24 eV). The adsorption energy of the 2 H atoms in these hollow sites is -0.66 eV ($E_{ads} =$

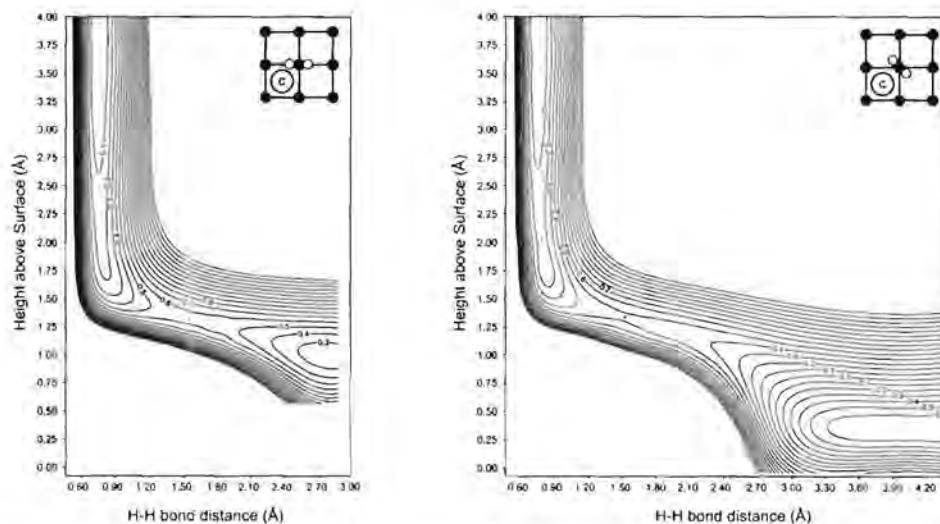


Figure 4.5: PES for H_2 dissociation on a $\theta_C = 0.25$ ML precovered Fe(100) surface with H_2 on top and rotated by 45° .

-0.33 eV per H atom).

From the previous profiles it is clear that there is also a repulsion between the C and the approaching H_2 molecule. We therefore also considered an *off-symmetry* adsorption profile similar to the one we calculated at $\theta_{CO} = 0.25$ ML with the H_2 centre of mass shifted away from the C by 0.5 \AA . This profile can be seen in Figure 4.6. It is clear that the C- H_2 repulsion is significantly smaller here. The initial repulsion is very small in this case and the corresponding dissociation barrier is 0.25 eV. This is smaller than most of the barriers we calculated on the clean surface. It is quite clear that the off-symmetry sites become very important when there is another adsorbate covering the surface.

We also considered the dissociation of H_2 on the bridge site which is not directly next to the C. The H_2 reaches a dissociation barrier of 0.31 eV with a profile that looks exactly like that of the clean surface bridge site. Over the two possible hollow sites much larger repulsions were observed than that which was observed on the clean surface indicating that the barriers will be higher than that of the clean surface hollow site.

We also considered the dissociation profile of H_2 directly on the pre-adsorbed carbon on the surface. This would directly form CH_2 . In this case the H_2 experiences an extremely strong repulsion as it approaches the C atom. The H_2 reaches a barrier of 2.20 eV in this process. This high barrier for direct CH_2 formation indicates that CH_2 would not likely be formed by direct addition of H_2 to the C atom and that the H_2 needs to be dissociated by the iron atoms. This strong repulsion would likely redirect the H_2 molecule to a more favourable site (e.g. off-symmetry or bridge sites).

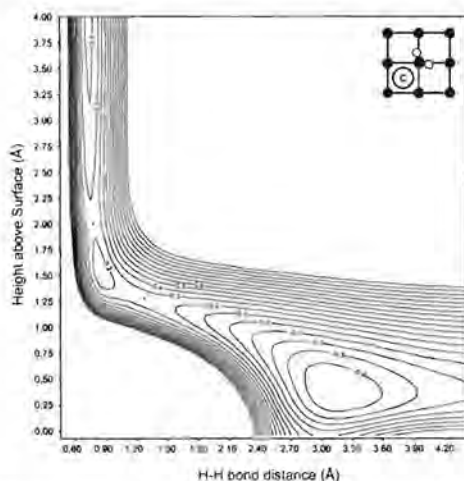


Figure 4.6: PES for H_2 dissociation on a $\theta_C = 0.25$ ML precovered Fe(100) surface with H_2 rotated by 45° . The H_2 centre of mass is slightly moved away from the high symmetry on top site.

4.3.3.2 $\theta_C = 0.50$ ML

Figure 4.7 shows the dissociation profile of H_2 on the on top site at $\theta_C = 0.50$ ML. The left of Figure 4.7 shows the on top dissociation pathway. Once again all the bridge sites will have a C atom in the hollow next to it. As the H_2 approaches the surface it experiences a slightly stronger repulsion than what was seen for the corresponding pathway at $\theta_C = 0.25$ ML and the clean surface. No distinct molecular adsorbed state was observed. The resulting dissociation barrier has an energy value of 0.95 eV. The adsorption energy of the 2 H atoms on the bridge site is 1.78 eV ($E_{ads} = 0.89$ eV per H atom). This adsorption energy is very unfavourable and the H atoms would probably be pushed into the empty hollow sites right next to them. Once again we see the C-H repulsion in effect.

The right profile in Figure 4.7 shows the dissociation profile of H_2 on the on top site with the H-H bond rotated by 45° parallel to the surface plane. In this case the H atoms end up in the two remaining hollow sites. The initial repulsion H_2 experiences as it approaches the surface is similar to that at $\theta_C = 0.25$ ML. No distinct molecular adsorbed state can be observed. The dissociation barrier has an energy value of 0.71 eV. This barrier is higher than at $\theta_C = 0.25$ ML. The adsorption energy of the dissociated H atoms in the hollow sites is -0.78 eV ($E_{ads} = -0.39$ eV per H atom).

Dissociation over the hollow sites and bridge sites cannot take place, since the bridge sites are blocked by the adsorbed C in the hollow sites.

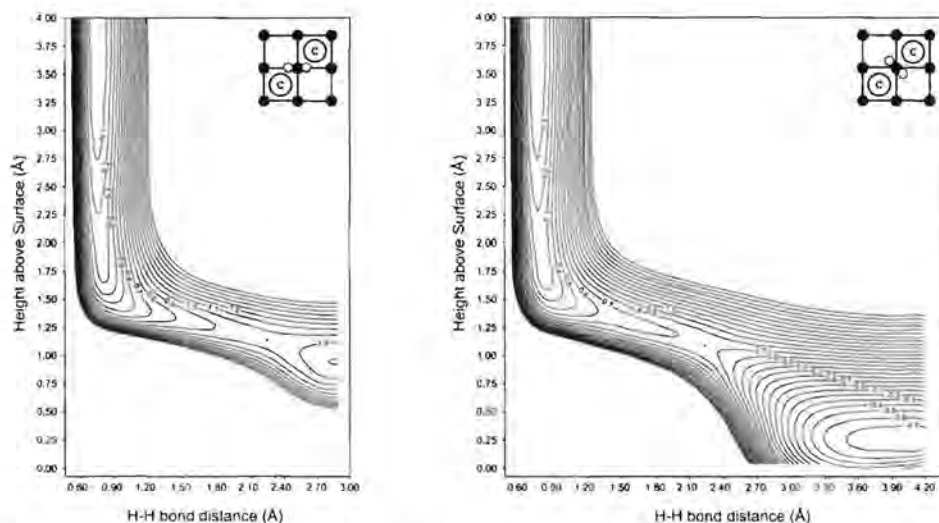


Figure 4.7: PES for H_2 dissociation on a $\theta_{CO} = 0.5$ ML precovered Fe(100) surface with H_2 on top and on top rotated by 45° .

4.3.4 Zero-point corrections

The above description considers H_2 as a classical particle. If we also want to consider it as a quantum particle we have to take the zero-point vibrations into account. We have calculated the estimated minimum zero-point energy perpendicular to the minimum energy pathway for selected profiles. The zero-point corrected overall barrier values are summarised in Table 4.1. It is interesting to note that after the zero-point corrections have been applied all the dissociation barriers have values that are on average 0.1 eV lower than in the classical approach.

4.3.5 Electronic analysis

We have calculated the Mulliken charges of the clean and precovered surfaces before the reaction with H_2 . These estimated charges are summarised in Table 4.2. The clean surface has a very small projected charge per surface atom. This changes as C and CO is introduced. The C atoms have large negative charges of $-0.75 e^-$ at both coverages, while the CO molecules have cumulative charges of $-0.82 e^-$ and $-0.79 e^-$ at $\theta_{CO} = 0.25$ ML and $\theta_{CO} = 0.50$ ML respectively.

We also calculated the LDOS for the same systems. Plots of the d-electron LDOS of the surface Fe atoms of these systems can be seen in Figure 4.8. These plots are all relative to the Fermi level (E_f). It is clear that although these d-bands are different in internal shape, their centres of gravity are at the same position relative to the Fermi level. The Fermi level, on the other hand, becomes lower as we introduce more C and CO to the surface (see Table 4.2). Since the d-band position does not change relative to the Fermi level, this change in the Fermi level will result in the subsequent lowering

Table 4.1: Summary of the calculated barriers for H₂ dissociation on clean and pre-covered Fe(100).

Profile	Site	E_a (eV)	$E_{a,ZPC}$ (eV) ^a	Barrier position ^b
Clean Fe(100)	On top	0.24	0.16	late
	On top 45°	0.33	0.22	late
	Bridge	0.34	0.26	early
	Hollow	0.86	0.73	early
$\theta_{CO} = 0.25$ ML	On top	1.46	1.34	late
	On top 45°	0.90	0.80	late
	Bridge	0.33	0.24	early
	Off-symm. top 45°	0.35	0.26	late
$\theta_{CO} = 0.50$ ML	On top	2.67	2.49	late
	On top 45°	1.33	1.24	late
$\theta_{CO,tilted} = 0.50$ ML	On top 45°	2.46	2.23	centre
$\theta_C = 0.25$ ML	On top	0.55	0.46	late
	On top 45°	0.49	0.40	late
	Bridge	0.31	0.23	early
	Off-symm. top 45°	0.25	0.08	late
	Top C	2.20	2.07	centre
$\theta_C = 0.50$ ML	On top	0.95	0.84	late
	On top 45°	0.71	0.60	late

^a $E_{a,ZPC}$ indicates the zero-point corrected barrier estimates.^b This indicates the position of the dissociation barrier on PES.

of the absolute energy of the d-bands.

The first of these electronic effects is the negative charges on the CO and C adsorbates. According to Nørskov et al. [14] the change in reactivity towards H₂ is due to the interaction of the hydrogen molecule with the electrostatic field that is induced by the adlayer. A negative field is regarded as a "poison" for the dissociation reaction. This seems to fit very well with our calculated charges and the accompanying increases in the barriers. The charge transfer that created the charged surface species is usually associated with a change in the Fermi level. As the Fermi level decreases, the difference in energy between the $1\sigma_g$ orbital of H₂ and the d-band decreases. Since the $1\sigma_g$ is a fully filled closed shell orbital, the Pauli repulsion will increase with the lowering of the Fermi level. The attractive interaction between the Fermi level and the LUMO ($1\sigma_u^*$) of H₂ is responsible for the weakening of the H₂ bond. Since a lowering in the Fermi level will increase the difference between these two electronic levels, this interaction becomes weaker. We can therefore expect an increase in the dissociation barrier of H₂ if the Fermi level and d-band shift to lower energies. To illustrate this relation we plotted the on top 45° site dissociation barriers as a function of a change in the Fermi level energy (Figure 4.9). In this view the H₂ position is kept constant and the CO and C occupies a similar surface area. This obviously does not include local effects that may result in a decrease of the barrier energy (as can be seen in the resulting off-symmetry dissociation pathways). From Figure 4.9 it is clear that the barrier height increases as the Fermi level becomes smaller. A linear regression of these values gave an empirical function of $E_a = -0.755E_f + 0.28$. By using this we predict that if the Fermi level Fe(100) surface can be increased by at least 0.45 eV (by alloying or adding a electropositive promoting adsorbate) the dissociation barrier can be decreased to 0 eV.

4.4 Discussion

A summary of all the barriers that we have calculated is given in Table 4.1. If we consider the values in Table 4.1 it is clear that most of the barriers for dissociation of H₂ change due to the pre-adsorbed C and CO on the surface. On the clean surface the lowest calculated zero-point corrected barrier for H₂ dissociation is on the on top site (0.16 eV). When we consider pre-adsorbed CO at $\theta_{CO} = 0.25$ ML we see that the barriers for the both the on top and the rotated on top type adsorption sites have increased significantly. An off-symmetry site has taken over the role as the lowest "late" adsorption barrier (after the "elbow-curve") for both CO and C. It is interesting to note that in both cases the bridge site adsorption barrier ("early" barrier) has not

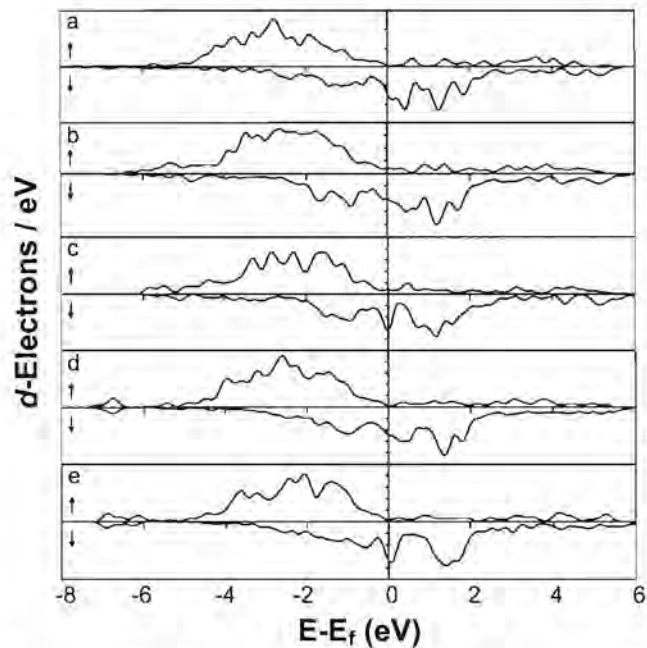


Figure 4.8: Spin resolved DOS plots of the d-bands of the surface Fe atoms for clean and precovered Fe(100) surfaces. a) Clean surface. b) $\theta_C = 0.25$ ML. c) $\theta_C = 0.5$ ML. d) $\theta_{CO} = 0.25$ ML. e) $\theta_{CO} = 0.5$ ML.

Table 4.2: Calculated charges (q) and Fermi level energies (E_f) for the clean and precovered Fe(100) surfaces. All charges are in e^- per atom.

System	q_{Fe}	q_C	q_O	E_f (eV)
Clean surface	0.04			-3.69
$\theta_C = 0.25$ ML	0.25	-0.75		-3.98
$\theta_C = 0.50$ ML	0.40	-0.75		-4.38
$\theta_{CO} = 0.25$ ML	0.25	-0.42	-0.40	-4.51
$\theta_{CO} = 0.50$ ML	0.45	-0.42	-0.37	-5.02

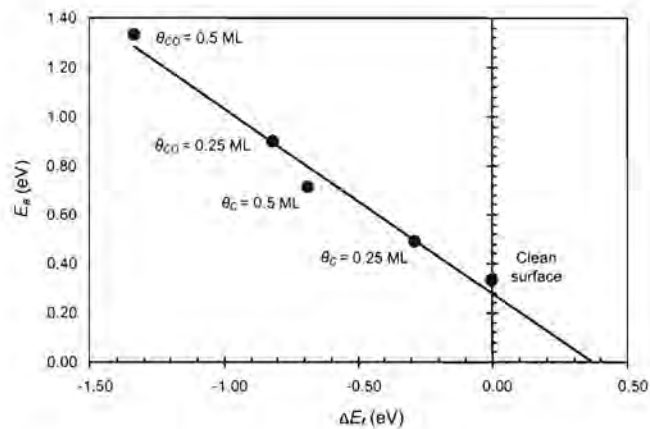


Figure 4.9: The H_2 dissociation barriers (E_a) on the on top rotated by 45° site as a function of the change in the Fermi level ΔE_f .

changed significantly.

When the pre-adsorbate coverage is increased further the picture changes significantly. H_2 dissociation with $\theta_{\text{CO}} = 0.5$ ML has the lowest calculated zero-point corrected barrier at 1.24 eV for the on top 45° site, while at $\theta_{\text{C}} = 0.5$ ML the lowest calculated zero-point corrected barrier energy is 0.60 eV for the on top 45° site. These values are three to six times larger than the barriers on a clean surface. In this model these are the only adsorption available pathways at these high CO and C coverages, since the bridge sites are blocked. The CO and C will also block certain hollow sites for adsorption by physically occupying certain hollow adsorption sites. By being directly next to the bridge sites, adsorption on the bridge sites are also blocked due to the large CO-H and C-H repulsion at these sites.

The calculated increase of the dissociation barriers in the presence of C corresponds to TPD experiments by Benziger and Madix [40] in which it was shown that carbon contamination reduced the iron surface's affinity for hydrogen. They proposed that at 200 K the initial sticking probability was reduced by an order of magnitude.

These sharp increases of the barriers at certain high symmetry points will contribute to steering slow moving (kinetic energy of less than $E_k \approx 0.1$ eV) H_2 molecules to the sites with the lower barriers (steering effect [30]). This may be a contributing factor in the case of Fischer-Tropsch, since the average kinetic energy in the Fischer-Tropsch temperature range (500 K – 650 K) is between 0.2 and 0.3 eV. If the kinetic energy of the hydrogen molecules is increased, this steering effect will become less effective. The favourable pathways generally seem to be the bridge sites and off-symmetry sites at coverages of 0.25 ML for both C and CO. Although the bridge sites seem favourable, dissociation of the H_2 molecule will be dynamically hampered on these sites if the H_2 molecules are vibrationally active. This is due to the fact that not only the barrier height is important, but also the position of the barrier on the PES [41]. If the barrier is "early" no translational-vibrational coupling is possible. It has been shown from molecular beam simulations that the hydrogen molecules which are not vibrationally active have a lower probability for dissociation [42]. In the case of these bridge site profiles no significant vibrational activation can take place and therefore the pathway will only be available for the dissociation of molecules with a normal kinetic energy component directly larger than the barrier height. The other H_2 molecules on these sites will be reflected away from the surface.

There are therefore two important effects involved when we consider the overall view of H_2 dissociation in the presence of pre-adsorbed C or CO on the Fe(100) surface:

1. The increase in the H_2 dissociation barriers (due to the surface electronics)

2. The physical blocking of available adsorption sites

If we consider the rate of hydrogen adsorption in an Arrhenius type equation, the rate constant (k) of the dissociation process can be written as the product of the barrier height in the exponent ($e^{-E_a/RT}$) and a pre-exponential factor (A). It is clear that an increase in the activation energy of dissociation will significantly lower the adsorption rate constant (effect 1). Considering the fact that the pre-exponential factors for dissociative adsorption (order of 10^6 s^{-1}) are generally significantly lower than that of surface processes (order of 10^{13} s^{-1}), the dissociative adsorption process cannot be considered to be a fast reaction. Changes to the value of the pre-exponential factor will therefore also have an impact on the rate constant. The decrease of the number of possible dissociation pathways and the physical blocking of the adsorption sites of the H atoms (effect 2) will contribute to a lower A value.

These two effects will result in a significant lowering of the rate constant of adsorption on highly precovered surfaces. Van Santen and Niemantsverdriet noted that with low pre-exponential factors, dissociative adsorption processes may already be the rate limiting step in many catalytic cycles [43]. This may become the case for hydrogen dissociation over a highly C or CO covered Fe(100) surface due to the accompanying large increases in the dissociation barriers and blocking of adsorption and dissociation sites.

The implication of this for the Fischer-Tropsch synthesis is that surface hydrogen is not necessarily freely available. This hydrogen availability will depend on the effect of the other coadsorbates (like CO and C in this case) on the H_2 dissociation barrier.

4.5 Conclusions

We have calculated the PES of the dissociation process of H_2 on clean and precovered Fe(100) surfaces. From the results it is clear that the presence of CO and C will block several sites for hydrogen adsorption as well as increasing the hydrogen dissociation barriers. At CO and C coverages of up to 0.25 ML the main contributor to the barrier increase is the CO-H and C-H repulsion. In these cases off-symmetry sites will play an important role to dissociate the approaching hydrogen molecules.

At coverages around 0.5 ML of CO and C we showed that the dissociation barriers increased to more than three times larger values than that of the clean surface. Since the effect of the activation barrier is expressed exponentially, this will result in a significant decrease in the rate constant for the dissociative adsorption process. Another factor at this coverage is the fact that many of the hydrogen adsorption sites will be

blocked, as well as the fact that the number of available possible pathways have also decreased. This will lower an already low pre-exponential factor. Overall the rate of dissociative hydrogen adsorption will be severely hampered in the presence of a highly CO or C covered surface.

Bibliography

- [1] Ertl, G. *Journal of Vacuum Science and Technology A* **1983**, 1(2), 1247–1253.
- [2] Dry, M. E. *Catalysis Today* **2002**, 71, 227–241.
- [3] Lundqvist, B. I.; Nørskov, J. K.; Hjelmberg, H. *Surface science* **1979**, 80, 441.
- [4] Groß, A.; Wilke, S.; Scheffler, M. *Physical Review Letters* **1995**, 75, 2718.
- [5] Groß, A. *Journal of Chemical Physics* **1999**, 110, 8696–8702.
- [6] Boszo, F.; Ertl, G.; Grunze, M.; Weiss, M. *Applications of Surface Science* **1977**, 1, 103–119.
- [7] Burke, M. L.; Madix, R. J. *Surface Science* **1990**, 237, 20–34.
- [8] Merrill, P. B.; Madix, R. J. *Surface Science* **1996**, 347, 249–264.
- [9] Sorescu, D. C. *Catalysis Today* **2005**, 105, 44–65.
- [10] Berger, H. F.; Grosslinger, E.; Rendulic, K. D. *Surface Science* **1992**, 261, 313.
- [11] Ko.; Madix, R. J. *Surface Science* **1981**, 109, 221.
- [12] Feibelman, P. J.; Hamann, D. R. *Physical Review Letters* **1984**, 52, 61.
- [13] Feibelman, P. J.; Hamann, D. R. *Surface Science* **1985**, 149, 48.
- [14] Nørskov, J. K.; Holloway, S.; Lang, N. D. *Surface science* **1984**, 137, 65–78.
- [15] Wei, C. M.; Gross, A.; Scheffler, M. *Physical Review B* **1998**, 57(24), 15572–15584.
- [16] Segall, M. D.; Lindan, P. J. D.; Probert, M. J.; Pickard, C. J.; Hasnip, P. J.; Clark, S. J.; Payne, M. C. *Journal of Physics: Condensed Matter* **2002**, 14, 2717–2744.
- [17] Hammer, B.; Hansen, L. B.; Nørskov, J. K. *Physical Review B* **1999**, 59(11), 7413–7421.
- [18] *MS Modeling 4*; Accelrys Software Inc., <http://www.accelrys.com>.
- [19] Monkhorst, H. J.; Pack, J. D. *Physical Review B* **1976**, 13(12), 5188–5192.
- [20] Murnaghan, F. *Proceedings of the National Academy of Science* **1944**, 30, 244–247.
- [21] Birch, F. *Physical Review* **1947**, 71, 809–824.
- [22] Kittel, C. *Introduction to Solid State Physics*; John Wiley and Sons, 7 ed., 1996.
- [23] Kohlhaas, R.; Donner, P.; Schmitz-Pranghe, N. *Zeitschrift für Angewandte Physik* **1967**, 23, 245.
- [24] Tyson, W. R.; Miller, W. A. *Surface Science* **1977**, 62, 267–276.
- [25] Huber, K. P.; Herzberg, G. *Molecular Spectra and Molecular Structure 4: Constants of Diatomic Molecules*; Van Nostrand Reinhold Co.: New York, 1979.
- [26] Hammer, B.; Scheffler, M.; Jacobsen, K. W.; Nørskov, J. K. *Physical Review Letters* **1994**, 73, 1400–1403.

- [27] Diño, W. A.; Kasai, H.; Okiji, A. *Journal of the Physical Society of Japan* **1995**, *64*, 2478–2487.
- [28] Dai, J.; Light, J. C. *Journal of Chemical Physics* **1997**, *107*, 1676–1679.
- [29] Kroes, G.; Gross, A.; Baerends, E.; Scheffler, M.; McCormack, D. A. *Accounts of Chemical Research* **2002**, *35*, 193–200.
- [30] Gross, A.; Scheffler, M. *Physical Review B* **1998**, *57*(4), 2493–2506.
- [31] Wilke, S.; Scheffler, M. *Physical Review B* **1996**, *53*, 4926–4932.
- [32] Eichler, A.; Hafner, J.; Groß, A.; Scheffler, M. *Physical Review B* **1999**, *59*, 13297–13300.
- [33] Dianat, A.; Sakong, S.; Gross, A. *European Physical Journal B* **2005**, *45*, 425–432.
- [34] Morse, P. M. *Physical Review* **1929**, *34*, 57–64.
- [35] Mulliken, R. S. *Journal of Chemical Physics* **1955**, *23*, 1833–1846.
- [36] Sanchez-Portal, D.; Artacho, E.; Soler, J. M. *Solid State Communications* **1995**, *95*, 685–690.
- [37] Bromfield, T. C.; Curulla Ferré, D.; Niemantsverdriet, J. W. *ChemPhysChem* **2005**, *6*, 254–260.
- [38] Moon, D. W.; Bernasek, S. L.; Lu, J.-P.; Gland, J. L.; Dwyer, D. *Surface Science* **1987**, *184*, 90–108.
- [39] Cameron, S. D.; Dwyer, D. J. *Langmuir* **1988**, *4*, 282.
- [40] Benziger, J.; Madix, R. J. *Surface Science* **1980**, *94*, 119.
- [41] Polanyi, J. C. *Science* **1987**, *236*(4802), 680–690.
- [42] Darling, G. R.; Holloway, S. *Journal of Chemical Physics* **1992**, *97*(7), 5182–5192.
- [43] Van Santen, R. A.; Niemantsverdriet, J. W. *Chemical Kinetics and Catalysis, Fundamental and Applied Catalysis*; Plenum Press, New York, 1995.

Chapter 5

Coadsorption of CO and H on Fe(100)

Where there is matter, there is geometry.

— JOHANNES KEPLER

5.1 Introduction

THE adsorption of carbon monoxide and the co-adsorption with hydrogen on the Fe(100) surface is particularly interesting because of its relevance to the Fischer-Tropsch synthesis. This reaction is used to obtain a wide spectrum of hydrocarbons by the reaction between hydrogen and carbon monoxide on Fe or Co catalyst surfaces [1]. Whereas separate CO and H adsorption on Fe surfaces has been studied quite extensively, very little information is available for the hydrogen-carbon monoxide coadsorption system.

In considering surface reactions between CO and H, knowledge of the conditions in which they can coexist on the metal surface is necessary. However, a limited number of studies on the coadsorption of these species exist and even less theoretical work exists [2–8]. The strong dependence of coadsorbate structure on the type of gas exposure (sequential vs. mixture), the adsorption temperature and the surface structure makes the predictions of coadsorbate structures very difficult [3]. Most studies were carried out by sequential dosing of H₂ and CO, however, under reaction conditions a mixture of reactant molecules interact with the catalyst surface. In the process of coadsorption some coadsorption effects have been observed such as blocking of H adsorption by CO (and vice versa) [3], formation of subsurface H [6, 9] and island formation [5].

Only a few studies on the coadsorption of H and CO on Fe surfaces are known. Wedler et al. [10] showed that CO induced changes in the adsorption state of H on Fe surfaces. It was postulated that pre-adsorbed H inhibits the dissociation of CO

on Fe [11]. Burke and Madix [12] did a systematic TPD study of the coadsorbed CO and H. They showed that the higher the CO coverage, the weaker the H is bound to the surface. They proposed that CO and H would be coadsorbed in a mixed adlayer with a repulsive interaction between the CO and H via electrostatic repulsion while 'through-surface' interactions might also play a role. By analysing H presaturated Fe(100) with EELS at both 100 K and 343 K, Merrill and Madix [13] found a quite different binding for CO with the blocking of the four-fold hollow site by H. They found that the frequency of the CO stretch vibration shifts to a higher value than for pure adsorbed CO. Contrary to the results with other transition metals they found no H and CO segregation on Fe(100).

Blyholder and Lawless [14, 15] attempted theoretical studies of coadsorption on Fe(100) by using semi-empirical calculations on a Fe_{12} cluster. However, this cluster is too small to give reliable results for an extended surface, because edge effects play a significant role. Despite this they found that H destabilised CO adsorption at on top sites, while at four-fold hollow sites both CO and H adsorption strengths decreased. To gain further insight into the coadsorption of H and CO on the Fe(100) surface we consider the results of calculations done within the pseudopotential approximation of first principles DFT. In this chapter we will analyse the different available coadsorption geometries on the Fe(100) surface. We also include a discussion on the electronic effects, the zero-point vibrational energy effects and the vibrational entropy of the adsorbates.

5.2 Method and models

5.2.1 Computational setup

The quantum chemical calculations in this work were performed using the CASTEP [16] code using the RPBE functional [17]. A Gaussian smearing method was applied to the electron distribution at the Fermi level with $\sigma = 0.1$ eV. The ion-electron interactions were described by core corrected ultrasoft pseudopotentials as included in the CASTEP suite [18].

A seven-layer slab was used with an optimised 10 Å vacuum layer between the surfaces. The surface was represented by using a $p(2 \times 2)$ periodic supercell. Adsorption was performed on both sides of the slab to facilitate the use of symmetry. The k-point sampling was generated by following the Monkhorst-Pack [19] procedure with a $5 \times 5 \times 1$ mesh. The plane wave basis set cutoff energy was set at 400 eV. The coordinates of all atoms were fully optimized. All of the calculational setup parameters (the

k-points mesh, the number of slab layers, the vacuum spacing, etc.) were optimised.

5.2.2 Coadsorption method

To study the coadsorption of CO and H we first have to look at the separate H and CO adsorption geometries. These were described in Chapter 3.

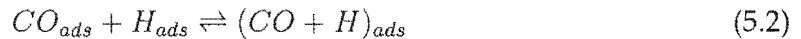
We proceeded to model the coadsorption of CO and H on Fe(100) by using the optimised CO adsorption geometries and superimposing the H adsorption geometries onto these. Only the CO geometries corresponding to the local minima calculated by Bromfield et al. [20] have been used as the starting CO geometries at CO coverages of $\theta_{CO} = 1$ ML, $\theta_{CO} = 0.5$ ML and $\theta_{CO} = 0.25$ ML. Although subsurface hydrogen adsorption is a possibility on some metals, coadsorption of CO with subsurface hydrogen was not considered, because Jiang and Carter [9] showed that hydrogen atoms prefer to stay on Fe surface instead of going into the subsurface layers or into the Fe bulk. The coadsorption energy per adsorbed CO is calculated by:

$$E_{coads} = \frac{E_{(CO+nH)} - E_{slab}}{2} - \frac{1}{2}nE_{H_2} - E_{CO} \quad (5.1)$$

with E_{coads} is the energy of formation of the species relative to the gas-phase CO and H_2 , $E_{(CO+nH)}$ is the calculated energy of the specific coadsorbed geometry, E_{slab} is the calculated energy of the clean Fe(100) slab, E_{H_2} and E_{CO} is the calculated energies of the gas-phase species H_2 and CO, and n is the number of H atoms in the specific adsorbate under consideration. The coadsorption energies do not include the zero-point vibrational energy corrections.

5.2.3 Analysis of island formation

To analyse the possibility that the coadsorption state (mixed state) would be the favoured state compared to island formation (the segregation of adsorbates to form separately adsorbed areas on the surface), its energy should be compared to the most stable separate adsorption energies of CO and H. This will give an initial indication (from the electronic energies alone) on whether the CO and H will be mixed or whether they will prefer to form islands on the Fe(100) surface. This can be regarded as a surface mixing reaction:



The left side of the equation represents the two segregated states and the right side the coadsorbed state.

To analyse island formation we follow a method similar to that proposed by Ciobica et al. [5]:

$$X = a - b - c - n\frac{d}{2} \quad (5.3)$$

$$Y = (e + f - 2b - c - n\frac{d}{2})/2 \quad (5.4)$$

where:

- a : energy of coadsorbed system
- b : energy of clean Fe(100) slab
- c : energy of CO in the gas phase
- d : energy of H₂ in the gas phase
- e : energy of CO adsorbed on Fe(100)
- f : energy of n H adsorbed on Fe(100)
- X : coadsorption energy of CO and H on Fe(100)
- Y : sum of the adsorption energies of the segregated CO and H on Fe(100)

Island formation is favoured if $|X| < |Y|$, whereas when $|X| > |Y|$ the reaction favours a mixed coadsorbed state. The difference between X and Y corresponds to the heat of mixing ($\Delta E_{mix} = (X - Y)/2$) for the surface mixing reaction in eq. 5.2. Our current model uses a conservation of surface sites. This implies that both the CO and H in the segregated state will be at double their surface coverages in the corresponding coadsorbed state.

5.2.4 Vibrational analysis

A partial Hessian vibrational analysis [21] was performed on the CO and H of some of the coadsorbed geometries. This approximation can be used since Fe atoms are much heavier than adsorbate atoms (see Appendix C). The vibrational analysis was performed using perturbations of 0.005292 Å in the Cartesian space. From this analysis we obtained the vibrational frequencies of the considered atoms. The harmonic vibrational zero-point energy can be calculated from these frequencies (ν):

$$E_{ZPVE} = \frac{\hbar}{2} \sum \nu_i \quad (5.5)$$

The effect of the vibrational entropy of the adsorbates was taken into account by calculating the vibrational entropy contribution from these frequencies using the method

applied by Li and Jensen [21]. The Gibbs free energy of mixing (ΔG_{mix}^*) can be approximated by including these vibrational entropy values (S^*) and the vibrational temperature corrections on E_{ads} and E_{coads} (E^*):

$$\Delta G_{mix}^* = \Delta H_{mix}^* - T\Delta S_{mix}^* \quad (5.6)$$

with

$$\Delta H_{mix}^* = \Delta E_{mix}^* + \Delta E_{ZPVE(mix)} \quad (5.7)$$

We have not included the configurational entropy contribution because in our case it should amount to less than $6 \text{ meV}/\text{\AA}^2$ at all temperatures lower than 1000 K [22].

5.2.5 DOS analysis

The electronic effects of coadsorption was also investigated by analysing the density of states (DOS) of some systems. The local DOS (LDOS) was calculated by a projection of the wavefunctions onto spherical harmonics to obtain the s, p and d character of the electrons. The DOS is also given relative to the Fermi-level of each system. All the DOS-plots are shown as spin-polarised with the α -spin profile at the top and the β -spin profile at the bottom.

5.2.6 Graphical Representation

In this chapter the adsorbate structures will be represented graphically by a space-filling model viewed along the surface normal (unless otherwise indicated). All of these representations corresponds to a $p(2 \times 2)$ surface unit cell. To avoid confusion the following colours are used to identify various atoms: Fe = purple, C = grey, O = red and H = white.

5.3 Results and discussion

5.3.1 Coadsorption at $\theta_{CO} = 1.00 \text{ ML}$

The results for the calculated coadsorption geometries at $\theta_{CO} = 1 \text{ ML}$ can be seen in Figure 5.1 and Table 5.1. With CO in the four-fold hollow the coadsorbed H totally destabilises the four-fold hollow CO coadsorption geometries (1-A and 1-B in Figure 5.1). The third geometry in Figure 5.1 (1-C) has two H atoms per CO. We found that by adding H to the bridge sites at this coverage, the CO gets removed from the four-fold

hollow. This CO is then pushed away from the surface into the vacuum leaving only H behind. Therefore 1-C indicates only the starting geometry.

Having CO on the bridge sites at $\theta_{CO} = 1$ ML gives rise to three coadsorption geometries (1-D to 1-F). Putting the H on the bridge site (1-D) gives rise to the lowest energy state of the three (0.03 eV lower than the corresponding pure CO adsorption geometry), while having H on top gives rise to an unstable geometry (1-E). If the H is in the four-fold hollow the geometry (1-F) is stable with regard to the gas molecules, but still less stable than the corresponding pure CO adsorption state.

When we consider the CO on the on top site there are four possible coadsorption geometries (1-G to 1-J). The first geometry (1-G) has H in the four-fold hollow and CO on top with a coadsorption energy of -1.22 eV. This is more stable than on top CO alone. This geometry is the most stable geometry of the high CO and H coverage geometries. This geometry is destabilised if the position of the H atoms are changed to the bridge site (1-H). By adding more H atoms to the geometry even further destabilisation takes place (1-I). By having three H atoms for every on top CO (1-J) the interatomic forces become very large. After relaxing the structure the H atoms in the four-fold sites were forced below the level of the surface Fe atoms.

Although these geometries at a CO coverage of $\theta_{CO} = 1$ ML are quite unrealistic (since the saturation coverage of CO is considered to be around $\theta_{CO} = 0.5$ ML [12, 23]) it clearly shows a lateral repulsion if the H and CO are too close together. It can also be seen that the coadsorption geometry becomes destabilised when H atoms are on the on top site. This is similar to the relative instability of the H atoms on the on top sites in pure H adsorption.

5.3.2 Coadsorption at $\theta_{CO} = 0.5$ ML

The results for the coadsorption geometries for a CO coverage of $\theta_{CO} = 0.5$ ML can be seen in Figure 5.2 and Table 5.1. Bromfield et al. [20] noted that at $\theta_{CO} = 0.5$ ML CO has two local minima: The on top and the four-fold tilted geometries. Thus, the coadsorption geometries imposing H-adsorption on to these two local minima were investigated. Only a few coadsorption geometries are possible when CO is in the on top position. This corresponds to 2-A to 2-D in Figure 2. From the results it can clearly be seen that H in the four-fold hollow is the preferred position if CO is on the on top site. Although these geometries were created by the superposition of the local minima of H and on top CO, the resulting geometries 2-A to 2-D are not local minima on the PES. This is evident from the vibrational analysis in which all these geometries have one or more imaginary frequency.

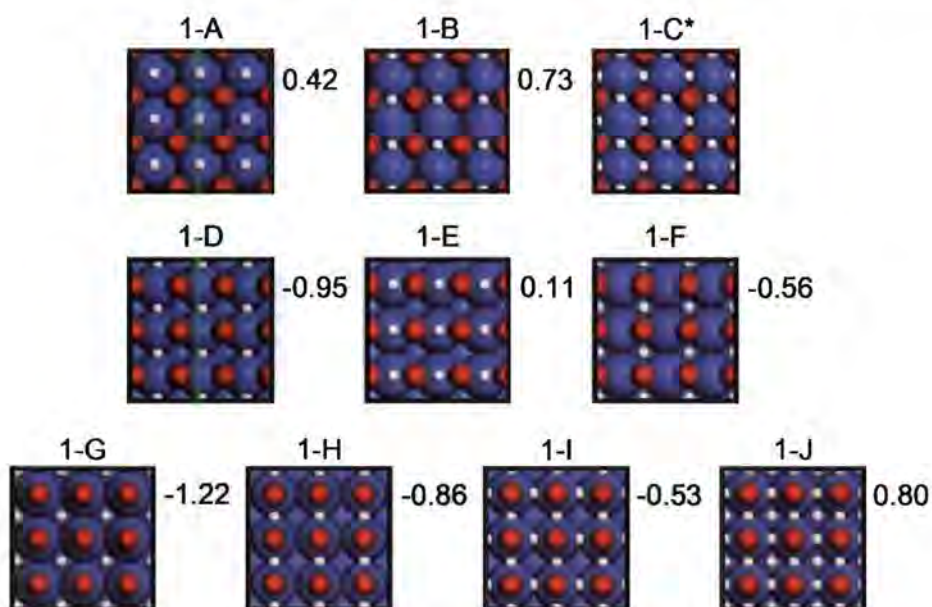


Figure 5.1: Top view of the coadsorption geometries on Fe(100) with $\theta_{CO} = 1$ ML (coadsorption energy (E_{coads}) in eV indicated to the right of each geometry; 1-C* indicates the starting geometry only).

When considering the coadsorption geometries for the tilted CO at $\theta_{CO} = 0.5$ ML it must be noted that there are three effects visible. The first can be seen in both 3-A and 3-B in Figure 5.2. The H atom is initially positioned in the centre of the four-fold hollow. H migration was observed upon optimisation of these coadsorption geometries where after it was located on the carbon's side of the hollow. These two coadsorption geometries are of similar energy values indicating that the additional H does not stabilise the geometry any further.

The second effect can be seen in 3-C and 3-D in Figure 5.2. The H was initially positioned on the bridge site next to the C atom, but upon optimising the geometry the H formed a bond with the C atom. The CO bond length is stretched to 1.363 Å in both cases. This lengthening of the bond indicates a weakening of the CO bond upon bonding of the H atom to the C atom of the CO. Although 3-D is less stable than 3-C, both geometries are less stable compared to pure CO in the tilted four-fold hollow state. These geometries are similar to the geometry Blyholder and Lawless [14] proposed for H assisted CO dissociation.

The third effect is seen when H is initially positioned on the bridge site which is parallel to the CO tilt direction. From here it migrates down into the four-fold hollow upon optimisation. Therefore, by putting one and two H atoms next to a titled CO adsorbate, the geometry optimised to 3-A and 3-B respectively. By putting two H atoms next to the same CO adsorbate both the H atoms moved into a hollow, giving rise to a coadsorption geometry with two H atoms in the same hollow (3-E). The same

effect is visible at higher H coverage on these bridge sites (3-F).

A radically different geometry was formed when two H atoms were placed on top next to the same C atom (3-G). The two H atoms moved toward the C atom and bonded to it. The C atom of the CO was pulled out of the hollow giving rise to a CO bond that is nearly parallel to the surface. The CO bond length is stretched to 1.42 Å while the other CO adsorbate's bond length is unchanged.

In all cases except those where the H was directly bonded to the C atom of the CO, the CO bond length decreased indicating that the coadsorbed H strengthens the CO bond.

An analysis of island formation (Table 5.1) showed that all of the considered geometries favour the mixed state, except 3-D. For the geometries where the H atoms are alone in the hollow sites (3-A and 3-B) the heat of mixing is quite large at -0.66 eV and -0.58 eV, respectively. It should be noted that the CO coverage in the segregated state (i.e. the CO island) has a coverage of $\theta_{CO} = 1.00$ ML, which is very unfavourable compared to pure CO adsorption at 0.50 ML (a difference of 0.70 eV). This large energy difference in compressing the adsorbed CO to a higher coverage when forming the segregated H and CO is the driving force behind the large energy of mixing.

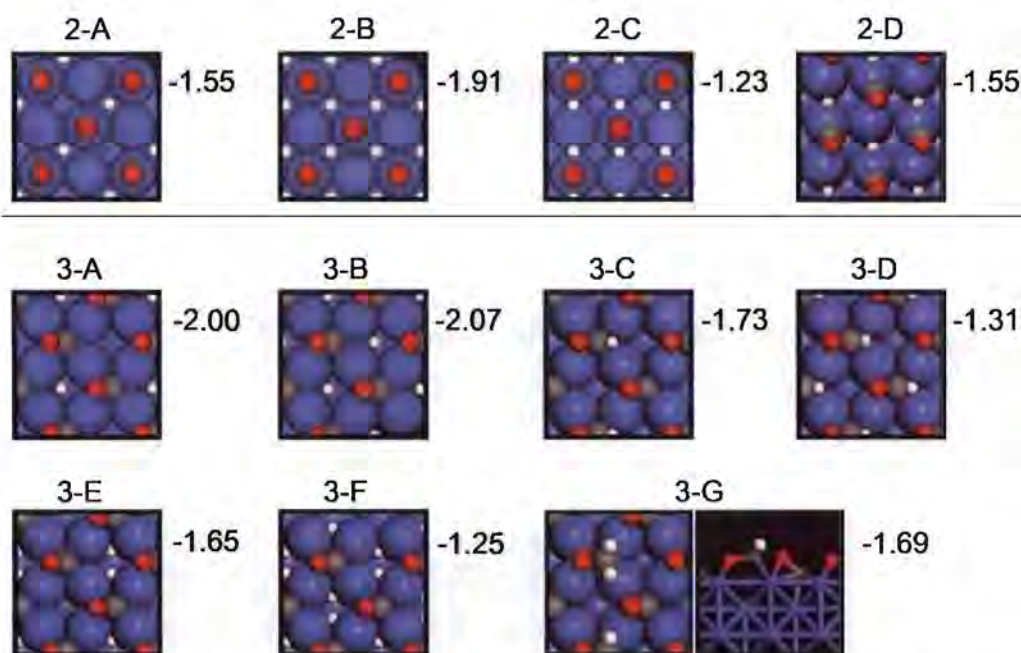


Figure 5.2: Top view of the coadsorption geometries on Fe(100) with $\theta_{CO} = 0.5$ ML (coadsorption energy (E_{coads}) in eV indicated to the right of each geometry; 3-G shows a side view for clarity).

5.3.3 Coadsorption at $\theta_{CO} = 0.25$ ML

Coadsorption of H and CO (in the tilted hollow site, since this is the only local minimum for CO adsorption at $\theta = 0.25$ ML) gave rise to a number of coadsorption geometries, most of which are very stable with regard to gas phase CO and H₂ (Figures 5.3 and 5.4, and Table 5.1).

Geometries 4-A to 4-G in Figure 5.3 correspond to the coadsorption geometries with the H atoms in the hollow sites. Geometries 4-A to 4-C represents a surface H-coverage of $\theta_H = 0.25$ ML. In 4-A the H is in the *trans*-hollow site which is the most favoured of the three geometries with a coadsorption energy of -2.34 eV. This is the only coadsorption geometry of these seven in which the CO bond is slightly longer than that of adsorbed pure CO (1.308 Å). Moving the H to the two different *cis*-hollow site geometries, 4-B and 4-C, gives rise to coadsorption energies of -2.17 eV and -2.22 eV respectively. This shows that there is a slight repulsion between the CO and the H which results in the *trans*-hollow being the site of preference. It is of interest to note that the positional shift of the H atom towards the C atom in the four-fold hollow is similar to what was shown for $\theta_{CO} = 0.5$ ML (3-A and 3-B). In both cases the repulsion results mainly from the H-O interaction, because the H is always shifted to the side of the hollow which is further away from the O atom.

An analysis of island formation was done on these geometries (Table 5.1). The values for the heat of mixing show that 4-A and 4-C favours mixed coadsorption by 0.15 eV and 0.03 eV respectively, while 4-B favours island formation by 0.2 eV.

Adding another H atom to a hollow site ($\theta_H = 0.5$ ML) gives rise to 4-D to 4-F. The additional H stabilises these geometries. 4-E and 4-F are the two most favoured geometries with coadsorption energies of -2.61 eV and -2.65 eV respectively. By keeping the *trans*-hollow site open we find a slightly less favoured geometry (4-D) at -2.54 eV.

When another H atom is added, all three possible four-fold hollow sites are filled up ($\theta_H = 0.75$ ML). 4-G corresponds to this arrangement with a coadsorption energy of -2.95 eV. The H which is in line with the CO adsorbate is once again shifted away from the O atom. This geometry is by far the most stable of all the coadsorption geometries that were considered.

The geometries from 4-D to 4-G all favour mixed coadsorption above island formation. 4-D has the smallest energy gain (-0.05 eV) while 4-G has the largest energy gain of all geometries at $\theta_{CO} = 0.25$ ML. Considering the heats of mixing of 3-A to 3-C, 3-E to 3-G, 4-A and 4-C to 4-G, it is clear that we can expect to find the H and CO in a mixed coadsorbed state (as proposed by Burke and Madix [12]).

The next group of coadsorption geometries with the tilted CO at $\theta_{CO} = 0.25$ ML were created by adding H to the bridge sites (geometries 4-I to 4-L and 4-Q in Figure 5.4).

Note that if a H is positioned on the bridge site which runs directly parallel to the axis of the tilted CO, it optimises to 4-C. Geometry 4-I, along with 4-K and 4-Q, has similar coadsorption energies indicating that there is no real difference in having H on either of the three bridge sites. The similar coadsorption energies for all three geometries show that there is an absence of a significant stabilising interaction between the CO and the coadsorbed H on any specific bridge site.

If we consider 4-J we see the same effect that was discussed for 3-C and 3-D. The H atom moved once again to bond with the C atom of the CO to form a 'HCO' species. This geometry is also similar to the geometry Blyholder and Lawless [14] proposed for H assisted CO dissociation.

Another interesting geometry was obtained by putting an H atom on the bridge site directly next to the O atom (4-L) binding the H to the O atom, resulting in a tilting away of CO tilted from the surface. The system optimised to a 'COH' adsorbed perpendicular to the surface. The CO bond length stretched to 1.420 Å and the C-O-H angle is 110.5°, which are both in line with what is generally found in aliphatic alcohols. This geometry is by far the least stable of the considered coadsorption geometries at $\theta_{CO} = 0.25$ ML. Both the 4-M and 4-N geometries are quite stable, but they show no significant interaction with the coadsorbed CO. Adding even more H to the surface resulted in the geometries 4-O and 4-P. From 4-O it can be seen how the H atoms migrated into the four-fold hollow site when initially positioned directly parallel to the tilted CO as was seen in 3-E and 3-F.

The coadsorption geometries that we considered with the H on the on top site all optimised to geometries we have discussed above (4-K, 4-M, 4-N and 4-Q). It can therefore clearly be stated that H would not be in the on top position when coadsorption has taken place.

All the geometries in Figure 5.4, except 4-P, have positive heats of mixing indicating likely island formation. 4-P has a H coverage equivalent to $\theta_H = 1.00$ ML. Upon segregation to islands the H atoms will be compressed to a state with a coverage of $\theta_H = 2.00$ ML. As can be seen in Table 3.1 the heat of H adsorption per H atom at this coverage is -0.02 eV. This is nearly iso-energetic with the gas-phase molecules. This is also 0.16 eV per H atom less stable than the corresponding H at the bridge site at $\theta_H = 1.00$ ML. The total destabilisation of the segregated state (4 atoms per $p(2 \times 2)$) is therefore 0.64 eV. This is similar to what was shown for the compression of the CO adlayer from $\theta_{CO} = 0.50$ ML to $\theta_{CO} = 1.00$ ML. Consequently, these effects show that the instability of the highly compressed segregated H and CO is one of the driving forces behind the favourable mixing of H and CO on Fe(100).

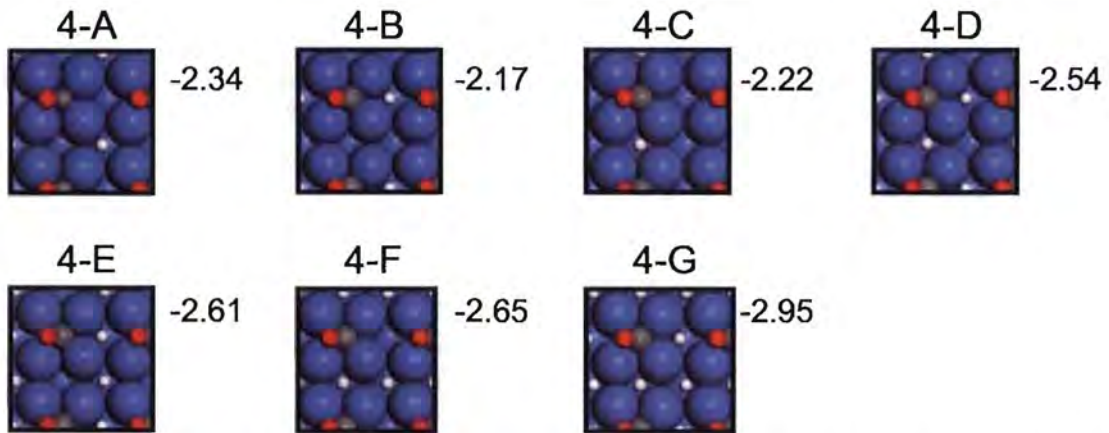


Figure 5.3: Top view of the coadsorption geometries on Fe(100) with $\theta_{CO} = 0.25$ ML with H in four-fold hollow sites (coadsorption energy (E_{coads}) in eV indicated to the right of each geometry).

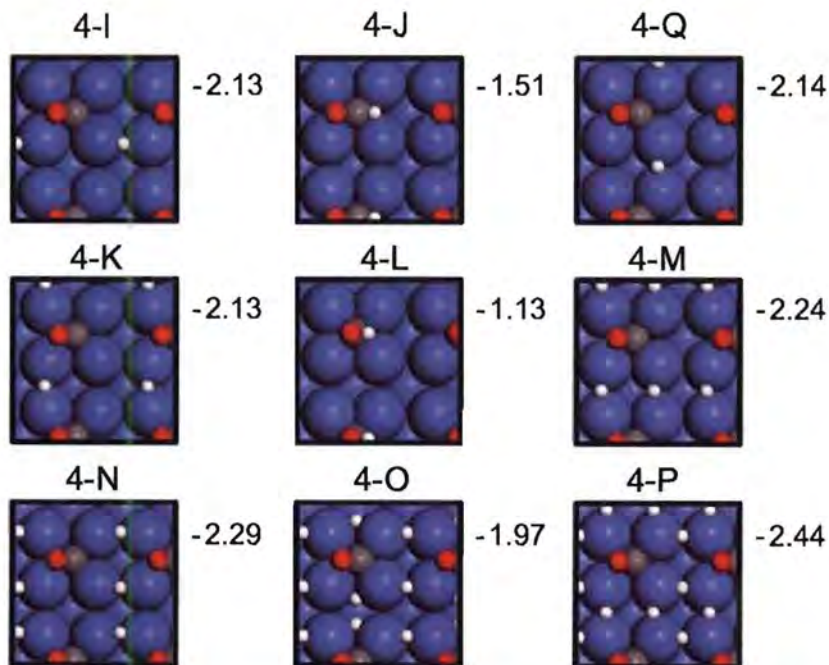


Figure 5.4: Top view of the coadsorption geometries on Fe(100) with $\theta_{CO} = 0.25$ ML with H on other sites (coadsorption energy (E_{coads}) in eV indicated to the right of each geometry).

Table 5.1: Calculated coadsorption energies, heats of mixing, CO bond lengths and angles for the considered coadsorption geometries on the Fe(100) surface at different initial CO coverages.

Label	CO site ^a	H site ^a	θ_H	H:CO	E_{ads}^b [eV]	ΔE_{mix}^c [eV]	d_{CO} [Å] ^d	ϕ [°] ^e
$\theta_{CO} = 1.00$ ML								
1-A	4F	1F	1.00	1	0.42		1.217	
1-B	4F	2F	1.00	1	0.73		1.204	
1-D	2F	2F	1.00	1	-0.95		1.171	
1-E	2F	1F	1.00	1	0.11		1.209	
1-F	2F	4F	1.00	1	-0.56		1.168	
1-G	1F	4F	1.00	1	-1.22		1.158	
1-H	1F	2F	1.00	1	-0.86		1.161	
1-I	1F	2F	2.00	2	-0.53		1.160	
1-J	1F	2F, 4F	4.00	4	0.80		1.165	
$\theta_{CO} = 0.50$ ML								
2-A	1F	4F	0.50	1	-1.55		1.167	
2-B	1F	4F	1.00	2	-1.91		1.166	
2-C	1F	2F	1.00	2	-1.23		1.165	
2-D	1F	2F	0.50	1	-1.55		1.175	
3-A	4FT	4F	0.50	1	-2.00	-0.66	1.296	47.3
3-B	4FT	4F	1.00	2	-2.07	-0.58	1.285	44.2
3-C	4FT		0.50	1	-1.73	-0.39	1.363	57.5
3-D	4FT		1.00	2	-1.31	0.17	1.363	57.3
3-E	4FT		0.50	1	-1.65	-0.16	1.288	50.3
3-F	4FT		1.00	2	-1.25	-0.02	1.267	44.6
3-G	4FT		0.50	1	-1.69	-0.21	1.417	99.6
$\theta_{CO} = 0.25$ ML								
4-A	4FT	4F	0.25	1	-2.34	-0.15	1.309	47.3
4-B	4FT	4F	0.25	1	-2.17	0.02	1.293	43.2
4-C	4FT	4F	0.25	1	-2.22	-0.03	1.303	47.3
4-D	4FT	4F	0.50	2	-2.54	-0.05	1.292	43.2
4-E	4FT	4F	0.50	2	-2.61	-0.12	1.295	43.3
4-F	4FT	4F	0.50	2	-2.65	-0.16	1.302	46.5
4-G	4FT	4F	0.75	3	-2.95	-0.56	1.294	43.8
4-I	4FT	2F	0.25	1	-2.13	0.06	1.304	46.6
4-J	4FT		0.25	1	-1.51	0.68	1.368	57.9 (111.4) ^f
4-K	4FT	2F	0.25	1	-2.13	0.06	1.295	44.4
4-L	4FT		0.25	1	-1.13	1.06	1.420	5.3 (110.5) ^g
4-M	4FT	2F	0.25	1	-2.24	0.25	1.298	46.8
4-N	4FT	2F	0.50	2	-2.29	0.20	1.300	45.2
4-O	4FT		0.50	2	-1.97	0.00	1.289	46.2
4-P	4FT	2F	1.00	4	-2.44	-0.46	1.287	42.0
4-Q	4FT	2F	1.00	4	-2.14	0.05	1.315	51.6

[a] Sites are defined by: 1F = on top; 2F = bridge; 4F = hollow; 4FT = tilted hollow. If there is no value, a special or undefined position is indicated. [b] ΔE_{ads} is the coadsorption energy. [c] ΔE_{mix} is the heat of mixing as defined in the text. [d] d_{CO} is the CO bond length. [e] ϕ is the angle between the surface normal and the CO molecular axis. [f] Value in brackets for the H-C-O angle. [g] Value in brackets for the C-O-H angle.

Table 5.2: Mulliken Charges at $\theta_{CO} = 0.25$ ML. (Charges indicated in electrons, e^-)

Label	q_H^a	q_C	q_O	q_{CO}
4-A	-0.29	-0.43	-0.46	-0.89
4-B	-0.26	-0.41	-0.45	-0.86
4-C	-0.28	-0.40	-0.46	-0.86
4-D	-0.29	-0.39	-0.45	-0.84
4-E	-0.28	-0.41	-0.45	-0.86
4-F	-0.28	-0.41	-0.46	-0.87
4-G	-0.28	-0.40	-0.45	-0.85
4-I	-0.29	-0.41	-0.45	-0.86
4-J	0.03	-0.58	-0.50	-1.08
4-K	-0.29	-0.41	-0.44	-0.85
4-L	0.42	-0.49	-0.61	-1.10
4-M	-0.28	-0.40	-0.44	-0.84
4-N	-0.28	-0.42	-0.44	-0.86
4-O	-0.26	-0.35	-0.43	-0.78
4-P	-0.24	-0.41	-0.41	-0.82
4-Q	-0.28	-0.40	-0.46	-0.86

[a] q_x indicates the charge in electrons (e^-)

5.3.4 Charge analysis at $\theta_{CO} = 0.25$ ML

Burke and Madix [12] proposed that the coadsorbed CO and H might have electrostatic repulsions. The Mulliken charges [24, 25] on the C, O and H atoms of the coadsorption geometries at $\theta_{CO} = 0.25$ ML were calculated (Table 5.2). The projected charges on the H atom varies between $-0.24 e^-$ and $-0.29 e^-$ except for 4-J and 4-L where the H is bonded to the C atom and the O atom of the CO, respectively. The negative charges on the H atoms in all the other geometries indicate that the adsorbed H underwent a charge transfer from the surface to become negatively charged. Except for geometries 4-J and 4-L the charge on the C atom varies from $-0.35 e^-$ to $-0.42 e^-$. The charges on 4-J and 4-L are significantly larger due to the positive charges on the H atoms that are bonded to CO in both geometries. The charges on the O atom varies between $-0.41 e^-$ and $-0.46 e^-$ for all geometries (except 4-J and 4-L). In all cases the charge on the O atom is slightly larger than that of the C atom. The total charge on the coadsorbed CO molecule varies between $-0.78 e^-$ and $-0.89 e^-$ in all cases (except 4-J and 4-L).

Although the Mulliken charge analysis is a crude estimation of the atomic charges, it clearly indicates that both H and CO are negatively charged when coadsorbed (except when they are directly bonded as in 4-J and 4-L). This implies that there will be a repulsive electrostatic interaction between the H and CO on the surface as the dominant destabilising effect.

5.3.5 Electronic analysis at $\theta_{CO} = 0.25$ ML

Although there are electrostatic repulsions between the H and the CO, many geometries would still prefer the mixed coadsorbed state rather than the segregated state on the surface. This indicates that the electrostatic repulsion is not the only interaction between the coadsorbed CO and H. Burke and Madix [12] proposed a 'through-surface effect', because CO and H both bond strongly to the surface Fe atoms. By calculating a localised density of states (LDOS) for the coadsorbed CO and H, the through-surface electronic interactions can be considered.

As an example of these interactions, the LDOS of the CO orbitals for three very stable coadsorption geometries were compared to pure adsorbed CO (Figure 5.5). The orbitals of pure adsorbed CO can be named according to the corresponding gas phase orbitals. The 3σ peak occurs at about -22.3 eV while the 4σ peak occurs at about -10.7 eV. The 1π and 5σ peaks occur at -7.3 eV and -6.8 eV, respectively. The 2π orbital spread out from -4.0 eV to higher than the Fermi level due to the interaction with the d-band of the Fe slab. Only the 2π orbitals show significant spin polarisation.

The positions of the 3σ , 4σ and 1π peaks relative to the Fermi level did not change at all upon coadsorption of H in geometry 4-A. The 2π orbital is only very slightly changed. A large change happens to the 5σ orbital where the peak has been spread out to a band between -7.9 eV and -6.0 eV. Only a slight difference arises between the α and β spin components for this band. This shift of about 1.1 eV to a lower energy value indicates an electronic stabilising effect and an upshift of the top of the band of about 0.4 eV indicating a slightly weaker destabilising effect, resulting in an overall stabilisation of the coadsorbed state. This is similar to the splitting of orbitals upon bonding in the classical molecular orbital view. This could be the origin of the stabilisation needed for the exothermic heat of mixing for this geometry.

A similar shift of the 5σ bond is observed in the CO LDOS of 4-B. In this case it results in three narrow bands per spin component at about -7.7 eV, -6.9 eV, -6.2 eV (α) and -5.9 eV (β). Again the downshift of the lower of the three bands are about 1.1 eV, whereas the largest upshift is about 0.9 eV. It seems like the stabilisation and destabilisation is relatively balanced in this case. The fact that the CO and H are much closer together in this geometry than in 4-A will enhance the electrostatic repulsion and therefore the slight stabilisation that might occur due to the electronic interactions, are not contributing enough to stabilise this geometry as a mixed state. This results in the preference for island formation for this geometry.

The addition of more H atoms to the coadsorbed state (4-G) results not only in the spreading of the 5σ bond, but also has an effect on the 1π orbital. Once again the orbitals spread out to lower and higher energy levels.

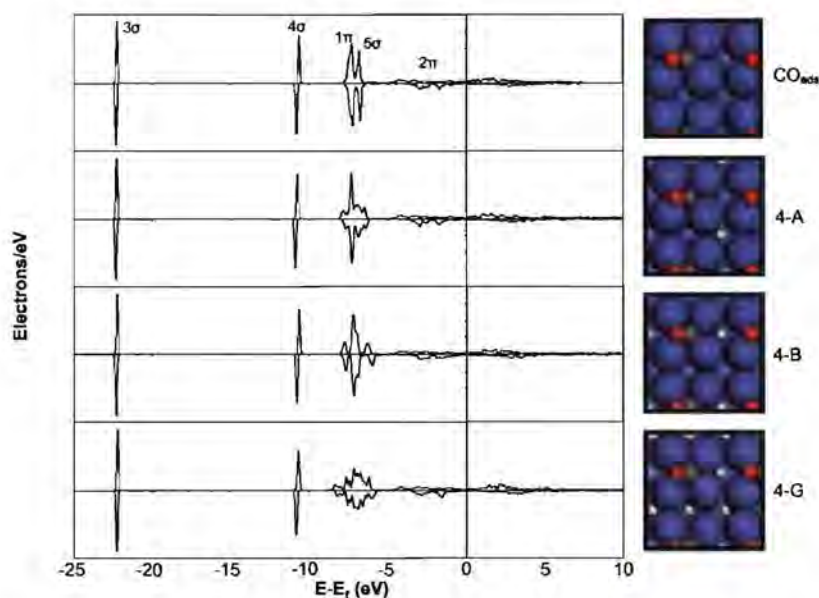


Figure 5.5: LDOS of the orbitals of CO in purely adsorbed CO and in the coadsorption geometries of 4-A, 4-B and 4-G.

The resulting LDOS plots for the pure adsorbed H and the same three coadsorption geometries are shown in Figure 5.6. In the top profile we can see the slightly spin polarised s-type orbitals of H adsorbed in the four-fold hollow. Although four peaks are visible, the first peak would dominate any interaction. This main peak lies at -7.4 eV and -7.1 eV for the α and β spin components, respectively. This is only 0.6 eV and 0.3 eV away from the 5σ peak in the LDOS of pure adsorbed CO. According to the molecular orbital theory, the closer the interacting orbitals are in energy the larger the splitting of the new bonding and anti-bonding orbital will be. Since the levels of the 5σ of CO and s-type orbitals of H are close in energy, this splitting effect due to bonding can surely be seen from these LDOS plots of the coadsorbed H and CO. The orbitals of the coadsorbed H (4-A, 4-B and 4-G) are spread out to the same levels as seen in the LDOS of coadsorbed CO (Figure 5.6).

A similar analysis was performed on a coadsorption geometry where the H atom is on a bridge site. The LDOS plots for the CO orbitals of pure adsorbed CO, 4-I and the orbitals of H of 4-I can be seen in Figure 5.7. If we compare the CO LDOS of pure adsorbed CO and 4-I we see no significant changes in any of the peak positions. The main peaks for the orbitals of H lie at -5.4 eV (α) and -5.0 eV (β). This is more than 1.4 eV away from the 5σ peak of CO. The orbital interaction between H and CO would thus be minimal. Hence, no further stabilisation due to electronic interactions with the H on the bridge site was observed. The only interaction in these coadsorption geometries is the electrostatic repulsions. Thus, coadsorption geometries with one H on the bridge site favours island formation in all cases at $\theta_{CO} = 0.25$ ML.

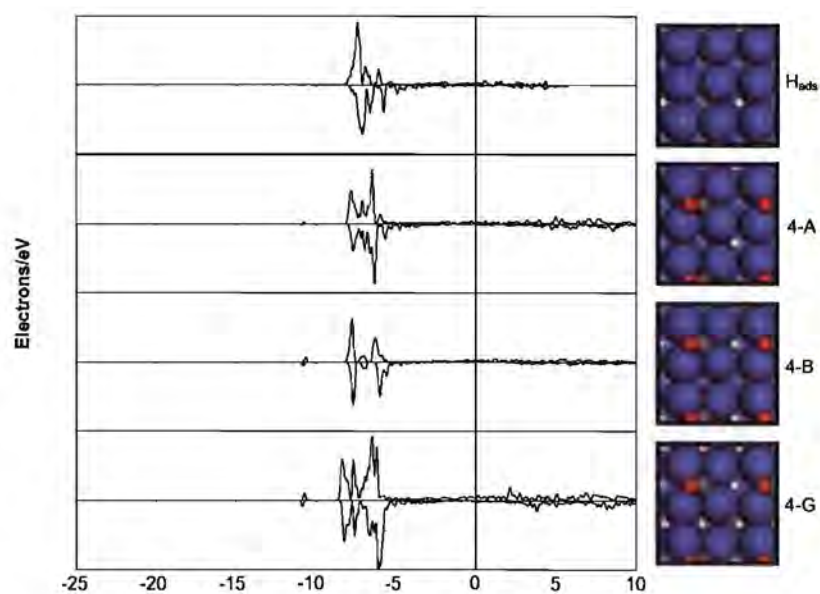


Figure 5.6: LDOS of the orbitals of H in purely adsorbed H and in the coadsorption geometries of 4-A, 4-B and 4-G.

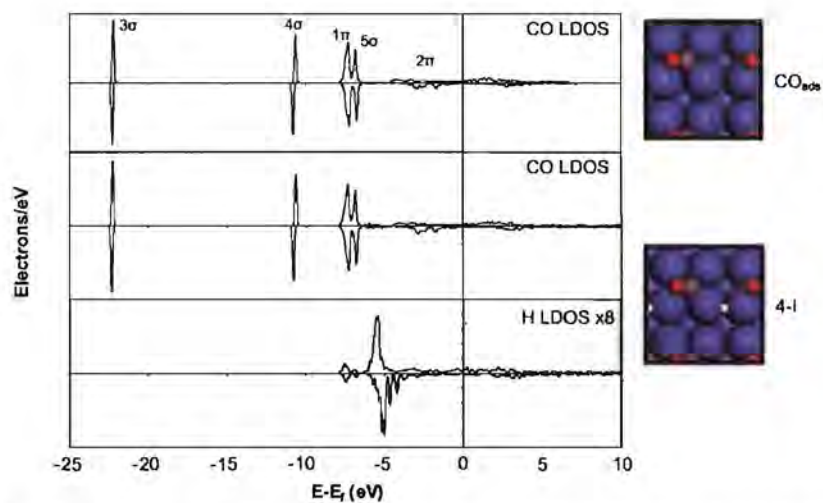


Figure 5.7: LDOS of the orbitals of CO and H (enlarged 8 times) in purely adsorbed CO and in coadsorption geometry 4-I with H on a bridge site.

5.3.6 Zero-point vibrational corrections at $\theta_{CO} = 0.25$ ML

In the previous sections we discussed the coadsorption according to the electronic contributions, but even at 0 K the quantum vibrations of the molecules can have an effect on adsorption energies. To analyse this we calculated the partial vibrational frequencies of CO and H in various structures at $\theta_{CO} = 0.25$ ML. The resulting frequencies, zero-point vibrational energies (ZPVE) and corrections to the coadsorption energies are given in Table 5.3. From the vibrational frequencies listed in 5.3 it is clear that all the listed geometries are local minima on the potential energy surface.

The CO stretching frequencies increase to values higher than pure adsorbed CO (1174 cm^{-1}) upon coadsorption of H, confirming the effect experimentally observed by Merrill and Madix [13]. In these cases, the coadsorption of H strengthens the CO bond which results in higher CO stretch frequencies. This is also reflected in the CO bond lengths (5.1). This is valid for all coadsorbed states except 4-J, which is strictly speaking not a mixed state but a product of a surface reaction. 4-J has a lower CO stretch frequency since it has been shown that the H that bonds to the C atom weakens the CO bond (*vide supra*). This surface reaction is discussed in the next chapter.

The ZPVE values of the coadsorbed states in Table 5.3 are quite large, ranging from 0.41 eV for 4-B to 0.78 eV for 4-G. These calculated ZPVE values will have a destabilising effect on the adsorption energies of pure adsorbed H and CO, as well as the coadsorption energies. The effect of these corrections on the heat of mixing is shown in Table 5.3. For 4-A, the heat of mixing is still exothermic although it has decreased from -0.15 eV to -0.11 eV. 4-B was destabilised even further by 0.02 eV. Geometries 4-C and 4-D favoured the mixed state, but after the ZPVE corrections these states favour island formation. The ZPVE corrections had no effect on 4-E (still favours the mixed state by 0.12 eV). On the contrary, we see that 4-F is drastically decreased from -0.16 eV to -0.04 eV. Geometry 4-G is even more favoured by 0.01 eV. The ZPVE corrections on 4-I show that this bridge site favours island formation even more after these corrections.

It is clear that the ZPVE corrections can change the state which was favoured if the original heat of mixing was quite small (like the cases of 4-C and 4-D). It is therefore important to consider ZPVE corrections when analysing the coadsorption of H and CO.

5.3.7 Effect of vibrational entropy

A first approach to describe the effect of temperature on the state of mixing includes an analysis of the partial vibrational entropy of the considered geometries (Table 5.3). The resulting estimated Gibbs free energies of mixing, ΔG_{mix}^* , as a function of temperature,

Table 5.3: Vibrational frequencies and zero-point vibrational energies (ZPVE) of a selected number of geometries. Emphasized values correspond to the CO stretching frequencies.

Label	Frequencies [cm^{-1}]	E_{ZPVE}^a [eV]	$\Delta E_{mix}^{b(corr)}$ [eV]
1.00 ML CO	1753, 322, 307, 307, 172, 172	0.19	
0.50 ML CO	1408, 1406, 689, 682, 570, 540, 518, 501, 491, 453, 430, 395	0.25	
0.25 ML CO	1174, 396, 317, 295, 218, 96	0.15	
0.25 ML H	1407, 695, 675	0.17	
0.50 ML H	1257, 1257, 503, 503, 442, 442	0.19	
0.75 ML H	1173, 1155, 1107, 667, 527, 518, 414, 367, 228	0.13	
1.00 ML H	1316, 787, 400	0.16	
1.50 ML H	1214, 1208, 1200, 1199, 1193, 1179, 1176, 950, 948, 926, 896, 858, 852, 820, 800, 765, 729, 617	0.18	
2.00 ML H	1238, 1119, 804, 799, 318, 223	0.14	
4-A	1579, 1261, 1223, 1161, 456, 364, 353, 260, 211	0.43	-0.11
4-B	1467, 1336, 1129, 917, 452, 405, 376, 310, 268	0.41	0.04
4-C	1654, 1290, 1144, 1079, 414, 389, 361, 250, 243	0.42	0.01
4-D	1674, 1540, 1306, 1207, 1202, 1187, 919, 475, 402, 319, 187, 157	0.66	0.05
4-E	1449, 1436, 1304, 1086, 926, 790, 734, 431, 351, 334, 184, 73	0.56	-0.12
4-F	1630, 1576, 1297, 1251, 1221, 1161, 1157, 513, 465, 370, 220, 208	0.69	-0.04
4-G	1415, 1393, 1351, 1301, 1126, 978, 911, 906, 853, 811, 423, 391, 328, 180, 159	0.78	-0.57
4-I	1852, 1760, 1370, 1194, 624, 559, 463, 428, 406	0.54	0.20
4-J	2601, 1348, 1052, 850, 439, 416, 372, 294, 285	0.47	0.77

[a] ZPVE - Zero-point vibrational energy. For pure H-geometries the value is given per H atom. For the rest it is given per CO.

[b] $E_{mix}^{b(corr)}$ is heat of mixing including the necessary ZPVE corrections.

are shown in Figure 5.8. To the left of Figure 5.8 the ΔG_{mix}^* values for coadsorbed geometries at $\theta_{CO} = 0.5$ ML is plotted, while the corresponding values at $\theta_{CO} = 0.25$ ML is plotted on the right graph of Figure 5.8.

In all cases ΔG_{mix}^* is the same as ΔE_{mix}^* at 0 K because there is no vibrational entropy contribution. As the temperature increases, the vibrational entropy contribution ($T\Delta S_{mix}^*$) becomes more pronounced. The ΔG_{mix}^* values (at $\theta_{CO} = 0.5$ ML) shows a significant increase with increasing temperature for all the considered geometries. Thus, mixing becomes less favourable with increasing temperature due to the vibrational entropy contribution.

For 3-A, 3-B and 3-C, ΔG_{mix}^* is negative across the whole considered temperature range (0 K – 800 K), although ΔG_{mix}^* for 3-C increases to nearly 0 eV as it approaches 800 K. The other considered geometries at $\theta_{CO} = 0.5$ ML are not favoured at temperatures larger than 0 K. These geometries would therefore favour island formation at all temperatures.

The ΔG_{mix}^* values at $\theta_{CO} = 0.25$ ML shows a small decrease with increasing temper-

ature for all the considered geometries. The trend for geometry 4-G has been omitted since it has a similar downwards trend as the other geometries at $\theta_{CO} = 0.25$ ML, with the exception that it starts at $\Delta G_{mix}^* = -0.57$ eV. This shows that because of the vibrational entropy the surface mixing reaction in eq. 5.2 becomes more favourable at this CO coverage. For 4-A, 4-E and 4-F the ΔG_{mix}^* values are negative across the whole considered temperature range, and thus the mixed state is favoured. At 0 K geometry 4-C favours island formation, although at approximately 220 K the value for ΔG_{mix}^* becomes negative, indicating that the equilibrium would shift toward the mixed state. Similarly, 4-D starts out favouring island formation up to 600 K. At higher temperatures the mixed coadsorbed state would be preferred. From these results it is clear that 4-B is the least favoured coadsorption geometry at $\theta_{CO} = 0.25$ ML because its ΔG_{mix}^* values are positive over the whole considered temperature range.

Fe(100) surfaces with CO at both $\theta_{CO} = 0.5$ ML and $\theta_{CO} = 0.25$ ML will yield a mixed coadsorbed state of coadsorbed CO and H at all considered temperatures (0 – 800 K), because at both of these coverages there are geometric arrangements in which the mixed coadsorbed state is preferred over the most stable island arrangements. These results concur with the experimental work by Burke and Madix [12]. At Fischer-Tropsch conditions (500 – 650 K) these results show that CO and H will still be in a mixed coadsorbed state. At $\theta_{CO} = 0.5$ ML and $\theta_{CO} = 0.25$ ML, the optimal saturation of the surface results in H:CO ratios of 1 and at 3 respectively.

It should be noted that under those conditions the effect of temperature on CO dissociation must be considered [26–28], because then the surface state of CO changes to atomic C and O on the surface and we cannot regard it as coadsorbed molecular CO and H any more. Other surface reactions, like the formation of ‘HCO’ adsorbates (like structures 3-C, 3-D and 4-A) will also become more likely at higher temperatures.

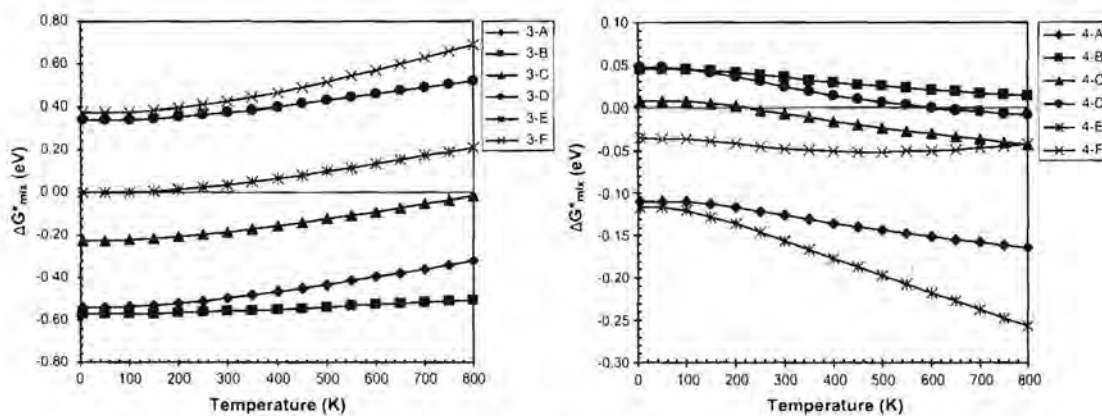


Figure 5.8: Trends in the free energy of the surface mixing process for coadsorption at $\theta_{CO} = 0.5$ ML (left) and $\theta_{CO} = 0.25$ ML (right).

5.4 Conclusions

We have constructed a model for the coadsorption of H and CO on Fe(100) from the separately adsorbed H and CO geometries at three initial CO coverages of $\theta_{CO} = 1$ ML, $\theta_{CO} = 0.50$ ML and $\theta_{CO} = 0.25$ ML. At $\theta_{CO} = 1.00$ ML we found large repulsions between the adsorbates and the resulting coadsorption geometries are not very stable with regard to the gas phase. At both $\theta_{CO} = 0.5$ ML and $\theta_{CO} = 0.25$ ML all the considered geometries are stable with regard to the gas phase molecules. The CO bond was not activated by the coadsorption of H, except in the cases where the H is in some way directly bonded to the CO. The coadsorbed geometry is destabilised by the electrostatic repulsion and stabilised by an electronic orbital interaction.

The stability of the coadsorbed geometries were compared to the stability of separately adsorbed H and CO to investigate whether the mixed state is more favoured than islands of CO and H. The comparison was performed against the pure adsorbed compounds at double the coverage to take into account the concentrating effect upon creating islands on a limited surface.

Upon inclusion of the partial zero-point vibrational energies and vibrational entropy, changes in the stabilities of the mixed coadsorbed states were observed. The final analysis of island formation, including the partial vibrational entropy, showed that the mixed coadsorbed state is favoured at both $\theta_{CO} = 0.5$ ML and $\theta_{CO} = 0.25$ ML. The main driving force for mixing seems to be the relatively less stable configurations of the high coverage CO and H in the segregated state. The optimal saturation H:CO ratios for the mixed coadsorption at $\theta_{CO} = 0.5$ ML and $\theta_{CO} = 0.25$ ML are 1 and 3 respectively.

Bibliography

- [1] Dry, M. E. In *Fischer-Tropsch Technology*; Steynberg, A., Dry, M., Eds., Vol. 152 of *Studies in Surface Science and Catalysis*; Elsevier, 2004; pages 533–600.
- [2] Li, J.; Schioett, B.; Hoffmann, R.; Proserpio, D. M. *The Journal of Physical Chemistry* **1990**, *94*(4), 1554–64.
- [3] Wang, H.; Tobin, R. G.; Lambert, D. K.; Fisher, G. B.; DiMaggio, C. L. *Surface Science* **1995**, *330*, 173–81.
- [4] Getzlaff, M.; Bode, M.; Wiesendanger, R. *Applied Surface Science* **1999**, *142*, 428–432.
- [5] Ciobica, I. M.; Kleyn, A. W.; Van Santen, R. A. *The Journal of Physical Chemistry B* **2003**, *107*, 164–172.
- [6] Rupprechter, G.; Morkel, M.; Freund, H.-J.; Hirschl, R. *Surface Science* **2004**, *554*, 43–59.
- [7] Cao, D.-B.; Zhang, F.-Q.; Li, Y.-W.; Wang, J.; Jiao, H. *The Journal of Physical Chemistry B* **2005**, *109*(21), 10922–10935.

- [8] Ma, Z.-Y.; Huo, C.-F.; Liao, X.-Y.; Li, Y.-W.; Wang, J.; Jiao, H. *The Journal of Physical Chemistry C* **2007**, *111*, 4305–4314.
- [9] Jiang, D. E.; Carter, E. A. *Physical Review B* **2004**, *70*, 064102.
- [10] Wedler, G.; Colb, K. G.; Heinrich, W.; McElhiney, G. *Applications of Surface Science* **1978**, *2*, 85–101.
- [11] Benzieger, J. B.; Madix, R. J. *Surface Science* **1982**, *115*, 279–289.
- [12] Burke, M. L.; Madix, R. J. *Surface Science* **1990**, *237*, 20–34.
- [13] Merrill, P. B.; Madix, R. J. *Surface Science* **1992**, *271*, 81–84.
- [14] Blyholder, G.; Lawless, M. *Progress in Surface Science* **1987**, *26*, 281–199.
- [15] Blyholder, G.; Lawless, M. *Langmuir* **1991**, *7*, 140–141.
- [16] Segall, M. D.; Lindan, P. J. D.; Probert, M. J.; Pickard, C. J.; Hasnip, P. J.; Clark, S. J.; Payne, M. C. *Journal of Physics: Condensed Matter* **2002**, *14*, 2717–2744.
- [17] Hammer, B.; Hansen, L. B.; Nørskov, J. K. *Physical Review B* **1999**, *59*(11), 7413–7421.
- [18] *MS Modeling 4*; Accelrys Software Inc., <http://www.accelrys.com>.
- [19] Monkhorst, H. J.; Pack, J. D. *Physical Review B* **1976**, *13*(12), 5188–5192.
- [20] Bromfield, T. C.; Curulla Ferré, D.; Niemantsverdriet, J. W. *ChemPhysChem* **2005**, *6*, 254–260.
- [21] Li, H.; Jensen, J. H. *Theoretical Chemistry Accounts* **2002**, *107*, 211–219.
- [22] Reuter, K.; Scheffler, M. *Physical Review B* **2003**, *68*, 045407.
- [23] Benziger, J.; Madix, R. J. *Surface Science* **1980**, *94*, 119.
- [24] Mulliken, R. S. *Journal of Chemical Physics* **1955**, *23*, 1833–1846.
- [25] Sanchez-Portal, D.; Artacho, E.; Soler, J. M. *Solid State Communications* **1995**, *95*, 685–690.
- [26] Moon, D. W.; Bernasek, S. L.; Dwyer, D. J.; Gland, J. L. *Journal of the American Chemical Society* **1985**, *107*, 4363–4364.
- [27] Benndorf, C.; Krüger, B.; Fritz, T. *Surface Science* **1985**, *163*, L675–L680.
- [28] Moon, D. W.; Dwyer, D. J.; Bernasek, S. L. *Surface Science* **1985**, *163*, 215–229.

Chapter 6

Hydrogen assisted CO dissociation

All things are in a process of change.

—MARCUS AURELIUS – MEDITATIONS, IX, 19

6.1 Introduction

THE topic of CO dissociation mechanisms is always of great interest in discussions on the reactions of synthesis gas over catalysts. This is typically the case for the Fischer-Tropsch reaction where Dry [1] has stated that there is still the question of whether the chemisorbed CO needs to dissociate or if it can be directly hydrogenated to 'CHO' and 'HCOH' species. On Fe the direct CO dissociation mechanism is usually considered to be the main mechanism of producing the surface carbide [2, 3]. In the past, other pathways for the scission of CO by metal surfaces have been proposed, including hydrogen assisted CO dissociation [4–11]. Wang et al. [4] proposed that on Pd the carbon species which forms CH₄ is originated in a hydrogen assisted step. By the use of theoretical methods this was shown to be the case on Pd and Pt [5–8]. On Ru it was shown that the rate constant for CO consumption significantly increased due to the assistance of hydrogen [9]. Various studies on Ni indicated that, although direct CO dissociation is favoured on the flat surfaces, the CO dissociation is assisted by hydrogen via a 'COH' species on various types of steps [5, 6, 10]. On Co the assistance of hydrogen in the CO dissociation process has also been noted to be more favourable [11].

On a clean Fe(100) surface CO can molecularly adsorb in a tilted state in the hollow site at both $\theta_{CO} = 0.25$ ML and $\theta_{CO} = 0.5$ ML [2]. These tilted CO molecules can readily dissociate upon heating to above 400 K [12, 13]. It is proposed that the saturation coverage of the molecularly adsorbed CO is around 0.58 ML [14] (also see Chapter 3).

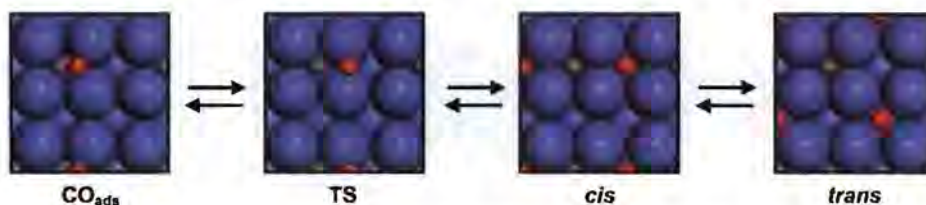


Figure 6.1: Direct CO dissociation pathway on Fe(100) at $\theta_{CO} = 0.25$ ML including the *cis* and *trans* product structures.

At $\theta_{CO} = 0.25$ ML the CO bond stretches as the O atom of CO moves away from the C. Dissociation proceeds through a transition state to the *cis* position and can subsequently dissociate to the *trans* position (See Figure 6.1). The reaction was calculated to be exothermic with an activation energy for dissociation of 1.14 eV [2]. At $\theta_{CO} = 0.5$ ML dissociation proceeds in a similar fashion, except that the O cannot dissociate away to the *trans* position since it is occupied by another CO molecule. At this coverage the reaction is calculated to be slightly endothermic with an activation energy of dissociation of 1.18 eV.

The first attempt to consider the hydrogen assisted CO dissociation pathway on iron was done by Blyholder and Lawless [15]. Using a semi-empirical theoretical approach, they compared CO dissociation to a hydrogen assisted pathway on a constrained 12 atom iron cluster, representing the Fe(100) surface. They showed that there are two points where a surface hydrogen atom can attach to the chemisorbed CO. Attaching the H atom to the C of CO results in an 'HCO' species and attaching the H atom to the O in CO results in a 'COH' species. Accordingly, both of these dissociate to form adsorbed 'CH + O' and 'C + OH' respectively. The direct CO dissociation barrier they calculated is an overestimate (53 kcal/mol) compared to the experimental value (26.2 kcal/mol [12]). Despite the overestimation of the values, they showed that the 'COH'-pathway did not decrease the overall dissociation barrier and that the 'HCO'-pathway had a dissociation activation energy which was about 40% lower (1.39 eV).

The aim of this chapter is to compare the direct CO dissociation to hydrogen assisted CO dissociation on the Fe(100) surface. We consider this by density functional theory (DFT) calculations performed within the pseudopotential approximation. We compared these two mechanisms by initially considering the CO dissociation mechanism on this surface, where after we consider the hydrogen assisted CO dissociation mechanism and discuss the implications of including this mechanism.

6.2 Computational method

In this study we used the CASTEP [16] DFT code to perform the quantum chemical calculations within the generalized gradient approximation (GGA) with the Revised Perdew Burke Enzerhof (RPBE) functional [17]. The smearing of the electron distribution at the Fermi level was calculated with a Gaussian smearing scheme with $\sigma = 0.1$ eV. The ion-electron interactions were described by core corrected ultrasoft pseudopotentials as included in the CASTEP suite [18].

To represent the Fe(100) surface we used a iron slab with a seven layers and a 10 Å vacuum spacing between the surfaces. The considered surface sites were represented by using a p(2×2) periodic supercell. To be able to use symmetry effectively we adsorbed the species of interest on both sides of the slab. The k-point sampling was generated by following the Monkhorst-Pack [19] procedure with a 5×5×1 mesh. We used a plane wave basis set cutoff energy which was optimised to 400 eV. Full geometrical optimisation was allowed of all the atoms. The linear synchronous transit/quadratic synchronous transit (LST/QST) method was used to locate the transition states structures [20–24].

We also performed partial Hessian vibrational analysis [25] on selected geometries. The vibrational analysis was performed using perturbations of 0.005 Å in the Cartesian space. From these calculations we obtain the vibrational frequencies (ν) from which we can obtain the vibrational zero-point energy:

$$E_{ZPVE} = \frac{1}{2} \sum_i h\nu_i \quad (6.1)$$

In this chapter the adsorbate structures will be represented graphically by a p(2×2) Fe(100) surface unit cell viewed along the surface normal. The following colours are used to identify various atoms: Fe = purple, C = grey, O = red and H = white.

6.3 Results

In chapters 3 and 5 we discussed the adsorption and coadsorption structures and energies of the various reactant species discussed below. In chapter 5 we showed that H and CO will be in a mixed coadsorbed state on the Fe(100) surface, allowing surface reactions between the two species to take place. The results for the CO dissociation and the hydrogen assisted CO dissociation calculations are given and discussed in this section.

6.3.1 CO dissociation

We calculated the tilted CO adsorption structures which is similar to those proposed by Bromfield et al. [2]. Furthermore we calculated the activation energy for the dissociation of this molecularly adsorbed tilted CO in the hollow site for $\theta_{CO} = 0.5$ ML and 0.25 ML according to:



Bromfield et al. [2] showed that the products of these CO dissociation processes are coadsorbed atomic C and O. At $\theta_{CO} = 0.25$ ML there are two possible coadsorption configurations which are referred to as the *cis* and *trans* positions (see Figure 6.1). We also calculated these reaction products with the *trans* configuration being 0.68 eV more stable than the *cis* configuration. The CO dissociation process will therefore initially result in the *cis* configuration with the subsequent diffusion of the O to the *trans* position. The activation energy for the diffusion of O from the *cis*(C+O) to *trans*(C+O) configuration is 0.44 eV. The overall energy of reaction of -1.14 eV.

The activation energy of the CO dissociation process at $\theta_{CO} = 0.25$ ML was calculated at 1.25 eV (28.8 kcal/mol). This is slightly larger than the values reported for the same pathway in other calculated work [2, 3] and the experimental value of 26.2 kcal/mol [12]. This value does not change much when zero-point corrections are included. For the reverse reaction we obtained an overall activation energy of recombination of 2.39 eV.

At $\theta_{CO} = 0.50$ ML we considered the dissociation of one of the two CO molecules in the $p(2 \times 2)$ unit cell. This will give rise to a configuration in which atomic C and O atoms are in a *cis* configuration with regard to each other. The second CO molecule is *trans* towards the C atom. We found that this dissociation product is almost iso-energetic at -0.06 eV. This is slightly more stable than the same structure calculated by Bromfield et al. [2] (0.10 eV) with PW91. The activation energy of the CO dissociation process was calculated at 1.19 eV. For the reverse reaction we obtained an overall activation energy of recombination of 1.25 eV. Zero-point corrections do not change these values significantly.

6.3.2 'HCO' and 'COH' formation

To be able to consider H assisted CO dissociation we first have to consider the formation of species where H has bonded to the CO. The H atom can be added to either the

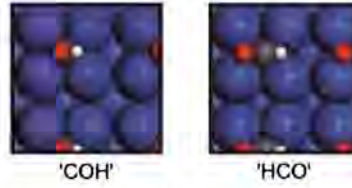
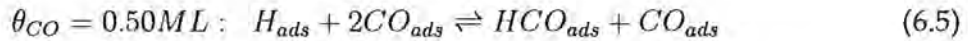
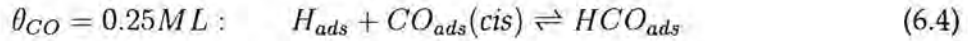


Figure 6.2: Structures of the 'COH' and 'HCO' species at $\theta = 0.25$ ML.

C or the O atoms, resulting in a 'HCO' or a 'COH' species on the surface (see Figure 6.2). In chapter 5 we showed that both these species are stable on the Fe(100) surface relative to the gas phase. The position of the CO bond in the 'HCO' is similar to that of the originally adsorbed CO. The 'COH' differs significantly since the OH group in the 'COH' is tilted away from the surface.

At $\theta_{CO} = 0.25$ ML the adsorption energies of 'HCO' and 'COH' relative to the CO and H₂ molecules were calculated to be -1.51 eV and -1.13 eV respectively. This results in a reaction energy for the formation step of these species of 0.66 eV and 1.04 eV. Both these reactions are endothermic with the formation of 'HCO' being energetically far more preferable. Since the minimum barrier for 'COH' formation should be at least higher than 1.04 eV, we will only consider the hydrogen assisted CO dissociation pathway from the 'HCO' species.

We calculated the activation energy of the formation of 'HCO' at both $\theta_{CO} = 0.5$ ML and 0.25 ML according to the following equations:



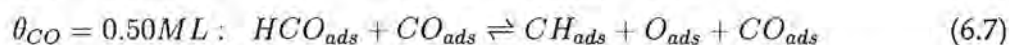
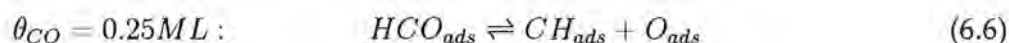
At $\theta_{CO} = 0.25$ ML the energy of the formation reaction is 0.66 eV. When we include the zero-point correction this becomes 0.72 eV. The activation energy for 'HCO' formation at $\theta_{CO} = 0.25$ ML is 0.83 eV. The subsequent backwards reaction activation energy is 0.17 eV. Upon inclusion of the zero-point energy corrections, the barrier for the forward reaction becomes 0.64 eV. This is smaller than the corrected energy of formation. It is therefore clear that the effective barrier for the forward reaction is the same as the zero-point corrected formation energy of 0.72 eV. Thus the effective backwards barrier becomes 0 eV.

At $\theta_{CO} = 0.5$ ML the heat of formation is 0.54 eV, which is slightly smaller than the same value at $\theta_{CO} = 0.25$ ML. We calculated the activation energy for 'HCO' formation at 0.55 eV and the backwards reaction at 0.01 eV. By including the zero-point energy corrections the barrier for the forward reaction increases slightly to 0.64 eV. It is clear that the effective barriers for H addition at both $\theta_{CO} = 0.25$ ML and $\theta_{CO} = 0.5$ ML can

be considered to be the same value as their respective heats of formation.

6.3.3 Hydrogen assisted CO dissociation

To be able to compare the H assisted CO dissociation barriers to those of CO dissociation, we calculated the activation energy for the dissociation of 'HCO' at $\theta_{CO} = 0.25$ ML and $\theta_{CO} = 0.5$ ML according to:



It is clear from the above equations that the products of 'HCO' dissociation differ from those of the pure CO dissociation. In the case of pure CO dissociation adsorbed C and O are the products, where in 'HCO' dissociation the products are coadsorbed CH and O.

At $\theta_{CO} = 0.25$ ML there are also two possible coadsorption configurations of CH and O. This will once again be referred to as the *cis* and *trans* positions (see Figure 6.3). We calculated these reaction products with the *trans* configuration being 0.69 eV more stable than the *cis* configuration. Similar to the CO dissociation, the 'HCO' dissociation process will initially result in the *cis* configuration with the subsequent diffusion of the O to give the *trans* configuration. The activation energy for the diffusion of O from the *cis*(CH+O) to the *trans*(CH+O) configuration is 0.43 eV. This gives an overall energy of reaction of -1.74 eV for equation 6.6. The activation energy of the 'HCO' dissociation reaction is 0.71 eV. Thus, the backwards reaction has an overall activation barrier of 2.25 eV. Upon inclusion of zero-point energy corrections the barrier of dissociation decreases slightly to 0.66 eV.

At $\theta_{CO} = 0.5$ ML the resulting product of the dissociation reaction has been calculated with an effective reaction energy of -0.67 eV. This change in energy is much smaller than at $\theta_{CO} = 0.25$ ML. At this initial CO coverage the activation energy barrier of 'HCO' dissociation is 0.69 eV. Upon inclusion of zero-point energy corrections the barrier of dissociation decreases to 0.52 eV.

6.4 Discussion

We can now compare the process of 'HCO' dissociation to that of pure CO dissociation. To do this, we compare the dissociation potential energy surface (PES) profiles of the full pathways at $\theta_{CO} = 0.25$ ML in Figure 6.4.

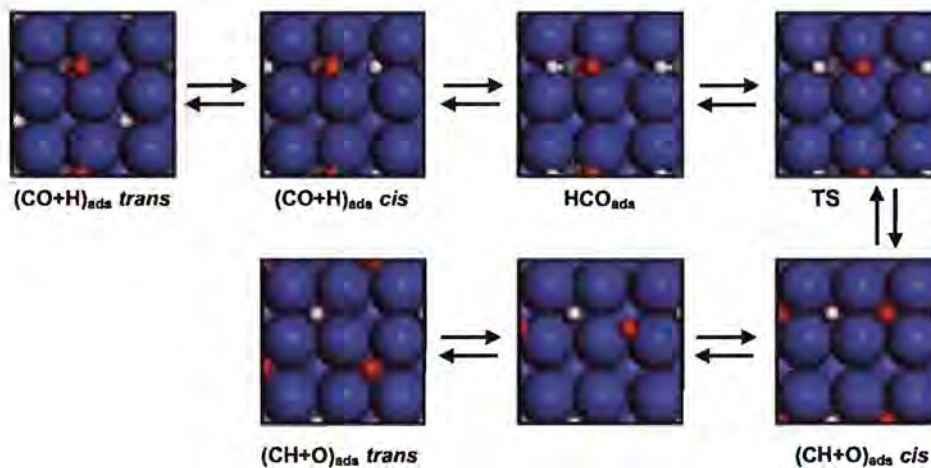


Figure 6.3: H assisted CO dissociation pathway on Fe(100) at $\theta_{CO} = 0.25$ ML, including the *cis* and *trans* H and CO coadsorption reagents, and the *cis* and *trans* product structures.

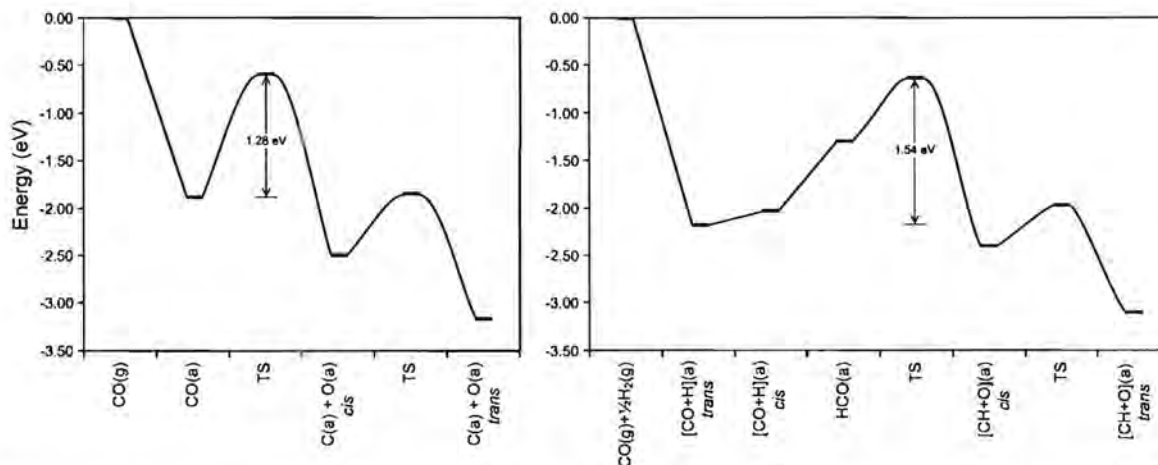


Figure 6.4: Comparison of PES of the zero-point corrected direct CO dissociation (left) and the 'HCO' dissociation (right) pathways at $\theta_{CO} = 0.25$ ML.

From Figure 6.4 it is clear that the overall ZPE corrected barrier for CO dissociation from the initial adsorbed $\theta_{CO} = 0.25$ ML state is 1.28 eV. If we compare this to that of the 'HCO' dissociation with the most stable coadsorbed state (1.54 eV) we find that the CO dissociation barrier is much smaller. It is quite easy to jump to the conclusion of discarding the HCO dissociation as non-competitive, but we have to keep in mind that the H surface coverage can have an effect on this analysis. Firstly we see this in the fact that when the H coverage increases, the hollow site corresponding to the *cis* $(CO+H)_{ads}$ configuration would be occupied. The energy difference in diffusion (going from *trans* $(CO+H)_{ads}$ to *cis* $(CO+H)_{ads}$) can be excluded in this case. The resulting overall barrier for 'HCO' dissociation now becomes 1.38 eV, which is only 0.1 eV larger than that of the CO dissociation.

We can now create a kinetic comparison of the initial rates of these two mechanism at $\theta_{CO} = 0.25$ ML by using transition state theory. We can set up very simple rate

equations if we consider both the 'CO' and 'HCO' dissociation mechanisms to be irreversible. For CO dissociation in the presence of H on the surface we can propose the following simple rate equation:

$$r_{CO} = k_{CO}\theta_{CO}\theta_*, \quad (6.8)$$

with

$$k_{CO} = \frac{k_B T}{h} \frac{pf^{TS}}{pf^{react}} e^{-E_{a,CO}/RT} \quad (6.9)$$

$$\theta_* = 1 - \theta_{CO} - \theta_H \quad (6.10)$$

where k_{CO} is the rate constant for CO dissociation, θ_{CO} , θ_H and θ_* is the respective CO, H and open hollow site coverages, k_B is the Boltzman constant, T is the temperature, h is the Planck constant, $E_{a,CO}$ is the CO dissociation activation barrier and R is the ideal gas constant. The temperature dependent partition function values for the reactant state and the transition state is given by pf^{react} and pf^{TS} . These can be approximated by the adsorbate vibrational partition function given by:

$$pf \approx \sum_i \frac{1}{1 - e^{-h\nu_i/k_B T}} \quad (6.11)$$

with ν_i as the vibrational frequencies.

In a similar way we can express the initial rate of HCO dissociation (r_{HCO}) as:

$$r_{HCO} = k_{HCO}\theta_{CO}\theta_H \quad (6.12)$$

with

$$k_{HCO} = \frac{k_B T}{h} \frac{pf^{TS}}{pf^{react}} e^{-E_{a,HCO}/RT} \quad (6.13)$$

where k_{HCO} is the rate constant for 'HCO' dissociation and $E_{a,HCO}$ is the overall 'HCO' dissociation activation barrier. In this equation lies the assumption that an open hollow site is not needed for 'HCO' dissociation, since in the first step of H addition an open site is created for the HCO to dissociate to.

We consider these two mechanisms as both being able to contribute to the total rate of the CO bond scission. This being the case, we need to know how much the hydrogen assisted pathway contributes to the total CO scission rate. The fractional contribution of the rate of the 'HCO' dissociation mechanism ($\frac{r_{HCO}}{r_{CO}+r_{HCO}}$) as a function of θ_H at a constant initial CO coverage of $\theta_{CO} = 0.25$ ML was calculated. The result of this comparison at a temperature of 300°C can be seen in Figure 6.5. In this figure we

consider the cases where H diffusion is excluded and where it plays an explicit role. This results in the two respective barriers of $E_a = 1.38$ and 1.54 eV mentioned above.

In both of these cases we showed that the hydrogen assisted barrier is larger than that of the direct CO dissociation mechanism. However, the H assisted pathway can still contribute to the scission of CO. In the case of $E_a = 1.54$ eV the hydrogen assisted mechanism only starts to play a significant role when the hydrogen coverage (θ_H) approaches 0.75 ML. If we consider the case where the thermodynamic effect of H diffusion is excluded ($E_a = 1.38$ eV) the contribution of the 'HCO' mechanism is at least 30% at $\theta_H = 0.5$ ML coverage. We expect the real case to lie somewhere in between these two limiting cases.

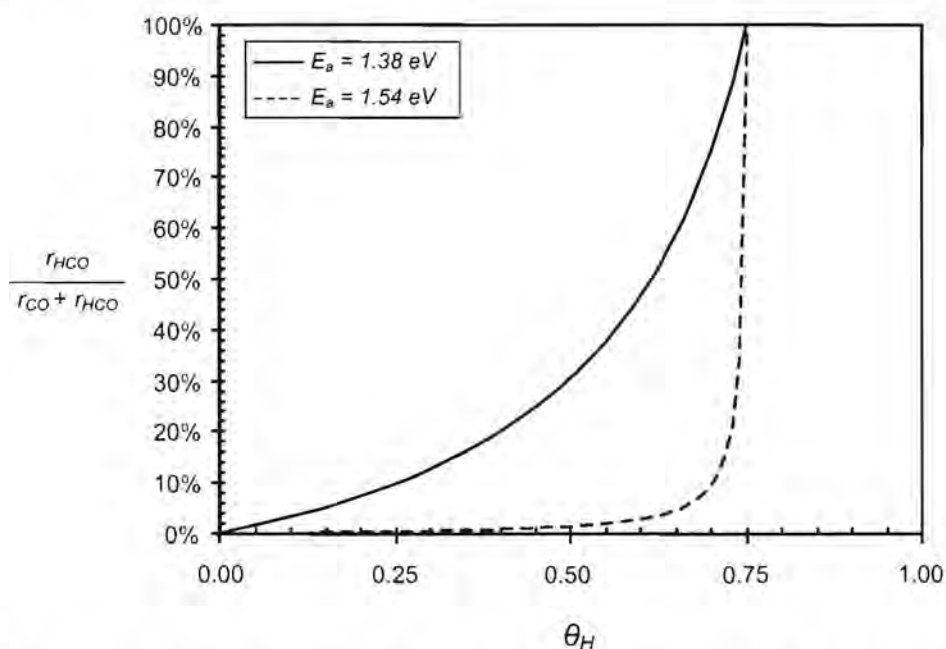


Figure 6.5: Percentage contribution of the 'HCO' dissociation mechanism to the total CO scission rate at 300°C with an initial $\theta_{\text{CO}} = 0.25$ ML.

We performed a similar analysis at an initial CO coverage of $\theta_{\text{CO}} = 0.5$ ML. The result of this comparison at a temperature of 300°C can be seen in Figure 6.6. In this case the effective H assisted barrier and the direct CO dissociation barrier is quite similar in height. It is clear that the H assisted dissociation pathway contribution increases monotonously with the initial H coverage θ_H . This shows that if the CO on the Fe(100) surface is near saturation coverage the CO bond scission can take place either by a direct CO dissociation or by H assisted mechanism, depending on the H coverage.

From these analysis it is clear that when both H and CO are present on this surface, H assisted CO scission is possible. The direct CO dissociation mechanism be the majority contribution at low H coverage, but as the empty hollow sites are filled by H atoms the 'HCO' mechanism will become more prominent.

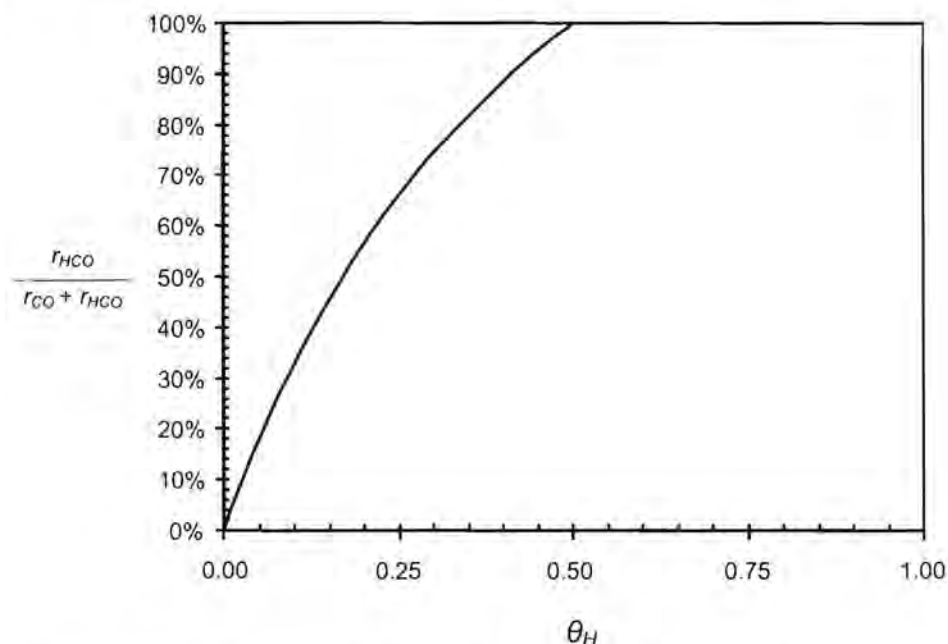


Figure 6.6: Percentage contribution of the 'HCO' dissociation mechanism to the total CO scission rate at 300°C with an initial $\theta_{CO} = 0.5$ ML.

6.5 Conclusions

We have calculated the structures and energies of the dissociation pathway of CO at initial CO coverages of $\theta_{CO} = 0.25$ ML and $\theta_{CO} = 0.5$ ML. This mechanism results in coadsorbed C and O dissociation products. Furthermore we presented the structures and energies of H addition to CO to form 'HCO' and 'COH' species. From the 'HCO' species we considered an H assisted CO dissociation pathway which results in coadsorbed CH and O products.

By comparing the initial rates of the CO and 'HCO' dissociation pathways we found that when both H and CO are adsorbed on the surface the direct CO dissociation mechanism will be the majority contributor to the effective CO scission rate at low initial H and CO coverages. As the empty hollow sites are filled by H atoms the H assisted mechanism will become more prominent and it will start to dominate when the hollow sites are almost fully filled. At $\theta_{CO} = 0.5$ ML both these mechanisms will contribute significantly to the CO scission rate. At this CO coverage the dominating mechanism will depend on the initial H coverage.

We propose that when both H and CO are present on the Fe(100) surface, hydrogen assisted CO dissociation is a possible CO scission pathway. The big difference between the two mechanisms lies in the respective dissociation products. At Fischer-Tropsch temperatures the scission of CO on the Fe(100) surface will probably take place via a combination of the direct CO dissociation and H assisted CO dissociation mechanisms,

producing a combination of C, CH and O surface species.

Bibliography

- [1] Dry, M. E. *Catalysis Today* **2002**, *71*, 227–241.
- [2] Bromfield, T. C.; Curulla Ferré, D.; Niemantsverdriet, J. W. *ChemPhysChem* **2005**, *6*, 254–260.
- [3] Sorescu, D. C.; Thompson, D. L.; Hurley, M. M.; Chabalowski, C. F. *Physical Review B* **2002**, *66*, 035416/1–035416/13.
- [4] Wang, S.-Y.; Moon, S. H.; Vannice, M. A. *Journal of Catalysis* **1981**, *71*, 167.
- [5] Shustorovich, E.; Bell, A. T. *Journal of Catalysis* **1988**, *113*(2), 341–352.
- [6] Bell, A. T. *Reaction Kinetics and Catalysis Letters* **1987**, *35*(1-2), 107–121.
- [7] Neurock, M. *Topics in Catalysis* **1999**, *9*, 135–152.
- [8] Gokhale, A. A.; Kandoi, S.; Greeley, J. P.; Mavrikakis, M.; Dumesic, J. A. *Chemical Engineering Science* **2004**, *59*, 4679–4691.
- [9] Nawdali, M.; Ahlafi, H.; Pajonk, G. M.; Bianchi, D. *Journal of Molecular Catalysis A: Chemical* **2000**, *162*, 247–256.
- [10] Andersson, M.; Abild-Pedersen, F.; Remediakis, I.; Bligaard, T.; Jones, G.; Engbæk, J.; Lytken, O.; Horch, S.; Nielsen, J.; Sehested, J.; Rostrup-Nielsen, J.; Nørskov, J.; Chorkendorff, I. *Journal of Catalysis* **2008**, *255*, 6–19.
- [11] Dai, X.; Yu, C. *Journal of Natural Gas Chemistry* **2008**, *17*, 17–23.
- [12] Moon, D. W.; Bernasek, S. L.; Lu, J.-P.; Glanda, J. L.; Dwyer, D. *Surface Science* **1987**, *184*, 90–108.
- [13] Cameron, S. D.; Dwyer, D. J. *Langmuir* **1988**, *4*, 282.
- [14] Burke, M. L.; Madix, R. J. *Surface Science* **1990**, *237*, 20–34.
- [15] Blyholder, G.; Lawless, M. *Progress in Surface Science* **1987**, *26*, 281–199.
- [16] Segall, M. D.; Lindan, P. J. D.; Probert, M. J.; Pickard, C. J.; Hasnip, P. J.; Clark, S. J.; Payne, M. C. *Journal of Physics: Condensed Matter* **2002**, *14*, 2717–2744.
- [17] Hammer, B.; Hansen, L. B.; Nørskov, J. K. *Physical Review B* **1999**, *59*(11), 7413–7421.
- [18] *MS Modeling 4*; Accelrys Software Inc., <http://www.accelrys.com>.
- [19] Monkhorst, H. J.; Pack, J. D. *Physical Review B* **1976**, *13*(12), 5188–5192.
- [20] Halgren, T. A.; Lipscomb, W. N. *Chemical Physics Letters* **1977**, *49*, 225–232.
- [21] Bell, S.; Crighton, J. S. *Journal of Chemical Physics* **1984**, *80*, 2464–2475.
- [22] Fischer, S.; Karplus, M. *Chemical Physics Letters* **1992**, *194*, 252–261.
- [23] Sinclair, J. E.; Fletcher, R. *Journal of Physics C: Solid State Physics* **1974**, *7*, 864–870.
- [24] Govind, N.; Petersen, M.; Fitzgerald, G.; King-Smith, R. D.; Andzelm, J. W. *Computational Materials Science* **2003**, *28*, 250–258.
- [25] Li, H.; Jensen, J. H. *Theoretical Chemistry Accounts* **2002**, *107*, 211–219.

Chapter 7

General Conclusions

*Still round the corner there may wait
A new road or a secret gate;
And though I oft have passed them by,
A day will come at last when I
Shall take the hidden paths that run
West of the Moon, East of the Sun.*

— J.R.R. TOLKIEN, LORD OF THE RINGS, BOOK VI, IX

AT the beginning of this thesis we proposed the broad question: What is the specific role of hydrogen in Fischer-Tropsch initiation? We proceeded to discuss this question by addressing the stated key questions in Chapter 1 by using density functional theory (DFT) calculations. This allowed us to probe into the molecular intricacies of the initiation steps of the Fischer-Tropsch reaction on Fe(100).

In this regard we showed that for both hydrogen and CO there will be a strong driving force to fill up the Fe(100) surface up to their respective saturation coverages at relevant Fischer-Tropsch conditions ($500 \text{ K} < T < 650 \text{ K}$ and $P > 1 \text{ bar}$). These correspond to a hydrogen saturation coverage of around $\theta_H = 1.00 \text{ ML}$ and a CO saturation coverage which lies between 0.5 and 0.65 ML. This shows that upon the adsorption of CO on Fe(100) at high pressures and temperatures, almost half of the hollow sites will still be open.

It was also shown that the dissociation of H_2 on a clean Fe(100) surface proceeds with relatively low barriers. These low values change when H_2 dissociation takes place on CO and C precovered Fe(100) surfaces. It is clear that the presence of CO and C will block several sites for hydrogen adsorption, as well as increase the various hydrogen dissociation barriers. Up to coverages of 0.25 ML of both CO and C the main

contributors to the barrier increases are the CO-H and C-H repulsions. These repulsions ensure that the proposed *off-symmetry* sites will play the dominant role in the H₂ dissociation. At the higher coverages of CO and C (around 0.5 ML) we showed that the dissociation barriers increased to at least three times larger barrier values than that of the clean surface. At these coverages adsorption site blocking also occurs. The increase of the dissociation barriers is mainly due to the change in the local electronic environment the H₂ molecule experiences as it approaches the surface. This can be seen in the relation between the change in the system's Fermi level and the increase in the dissociation barriers. Following this relation, we predict that adsorbates or promoters that increase the Fermi level of the catalyst surface could decrease the dissociation barrier.

A significant decrease in the rate constant of the dissociative adsorption process would result from the blocking of adsorption sites and the very large increases in the dissociation barriers on a highly covered C or CO surface. With an already low pre-exponential factor this process may become a very slow reaction step and can, in the case of a very highly CO or C covered Fe(100) surface, be rate limiting. This will surely affect the availability of the hydrogen atoms that are necessary for the rest of the steps in the Fischer-Tropsch reaction.

Despite the increase of these H₂ dissociation barriers we showed that the dissociated hydrogen can coadsorb with the molecular CO on this surface. We showed that electrostatic repulsive interactions exist between the adsorbed CO and H, since both are negatively charged on the surface. An electronic interaction between the adsorbed CO and H orbitals also play a role when these species are coadsorbed. This electronic interaction is essentially a 'through-surface' effect and it can be a stabilising effect for certain coadsorption geometries. A number of these coadsorption geometries at both $\theta_{CO} = 0.25$ ML and $\theta_{CO} = 0.5$ ML are stable in a mixed coadsorbed state and will not likely form islands at Fischer-Tropsch temperatures. This mixing of H and CO on Fe(100) has its origins in the relative instability of the corresponding compressed CO and H islands. For these mixed states the optimal surface H:CO ratios for $\theta_{CO} = 0.5$ ML was shown to be 1, while the at $\theta_{CO} = 0.25$ ML it is 3. This mixed coadsorption is necessary if reactions between H and CO can take place.

One of these reactions is the hydrogenation of molecular CO. We showed that the addition of H to CO to form 'HCO' and 'COH' species is possible, although both are endothermic reactions. The 'HCO' species is the most stable of the two and we showed that this species can dissociate to form coadsorbed CH and O products.

Comparing this H assisted CO dissociation to normal direct CO dissociation we showed that when both H and CO are adsorbed on this surface H assisted CO dissociation does play an important role. The direct CO dissociation mechanism will

be the majority contributor to the effective CO scission rate at low initial H and CO coverages. If the H coverage increases the H assisted mechanism will become more prominent. At $\theta_{CO} = 0.5$ ML both these mechanisms will contribute significantly to the CO scission rate. The dominant CO scission mechanism depends strongly on the initial H coverage. We therefore proposed that H assisted CO dissociation is a possible CO scission pathway on Fe(100). At Fischer-Tropsch temperatures the scission of CO on the Fe(100) surface will probably take place via a combination of the direct CO dissociation and the H assisted CO dissociation mechanisms. Together they produce a mix of C, CH and O surface species.

Considering these results it is clear that the initial steps that involve hydrogen are much more intricate than supposed by the simple mechanistical representations discussed in sections 1.1.1.1 – 1.1.1.4. It is clear that on this surface the CO and H can be mixed, but that the same CO (or C from CO dissociation) can inhibit the H₂ dissociation that provides the surface H atoms. This is essential since the feasibility of mechanisms such as the H assisted CO dissociation depends on the surface H coverage. It is therefore quite clear that the H surface coverage is of high importance to the Fischer-Tropsch reaction.

If we consider the fact that the presence of hydrogen on the Fe(100) surface does not exclude CO dissociation, but can offer an alternative pathway, it is clear that CO dissociation will take place on the Fe(100) surface under Fischer-Tropsch conditions, irrespective of the H concentration. Furthermore we showed that the formation of both the 'HCO' and 'COH' species are endothermic and that the dissociation products for CO and 'HCO' are mostly exothermic. We therefore do not expect 'HCO' (or 'COH') to be present in large enough surface concentrations to undergo further significant hydrogenation. This seems to favour the 'alkyl' (section 1.1.1.1) and 'alkenyl' (section 1.1.1.2) mechanisms in which CO first needs to dissociate to be able to form the chain growth initiators and monomers.

We must always be careful when projecting the results obtained on a model surface to the real Fischer-Tropsch catalysts. One obvious way to overcome this is to apply an approach similar to the one in this thesis to other relevant Fe surfaces, like the Fe(110) surface. The Fe(110) surface is denser than the Fe(100) and has a different geometry. These will obviously alter the chemistry of the processes corresponding to those described in this thesis. Processes such as coadsorption and H assisted dissociation, will therefore be slightly different. Another point to keep in mind is the fact that we make these conclusions for a ideal surface of an α -Fe bulk structure. The industrially applied Fischer-Tropsch catalysts usually has a range of structural and chemical promoters. These added chemical species can reside in the bulk of the Fe or as ad-

layers on the surface. This will effectively change the electronics of the metal surface, which will, in turn, change the adsorption behaviour of the hydrogen and CO gases, their dissociation rates and the H and CO surface interactions. We showed that the electronic character of the surface can affect steps such as the H₂ dissociation process. Bulk phase changes, such as carbiding, can have similar effects.

Despite these limitations, we have used the model Fe(100) surface to lift the veil on the mysterious hydrogen in the Fischer-Tropsch reaction. Much more fundamental research is necessary if we would like to understand this problem to the full extent. These include areas such as the role of H in the formation of OH and H₂O, the role it plays in the Fischer-Tropsch methane selectivity and, obviously, the effect that promoters have on the availability of H on the surface.

Appendix A

Glossary

To be conscious that you are ignorant is a great step to knowledge.

— BENJAMIN DISRAELI (1804 - 1881), SYBIL, 1845

<i>Ab initio</i> methods	Literal meaning: From the beginning. This is usually used to describe theoretical methods using no experimental inputs.
Back-donation	Refers to the movement of electrons from an orbital or a band on one species to a π anti-bonding orbital of another species.
Band theory	A condensed state materials theory where the available electronic energy levels are spread into groups of energy levels called "energy bands."
Brillouin zone	The first Brillouin zone is the simplest representative cell in the reciprocal space of a periodic medium in which the wavefunction solutions can be completely described.
CASTEP	Cambridge Sequential Total Energy Package.
Chemisorption	The chemical bonding of a gas-phase species to an adsorbing medium.
Cluster	A model with a finite number of atoms representing either a very small crystal or part of a larger crystal surface.
Coadsorption	Simultaneous adsorption of two species.
Cutoff energy	The numerical basis sets that are used to calculate the wavefunctions can be truncated to include only plane waves that have kinetic energies that are smaller than a specified cutoff energy.
Density of states (DOS)	DOS is a property of a system that quantifies how closely the electronic energy levels are packed.
EELS	Electron Energy Loss Spectroscopy.

Embedded cluster	A cluster that represents a specific site on a crystal. The rest of the crystal is approximated by an applied potential.
Exchange-correlation	The exchange-correlation functional is a functional that describes the exchange and correlation interactions of electrons in a high density of electrons. The first used set of these functionals is called the local density approximation (LDA), but to include non-local effects the generalised gradient approximation (GGA) was developed.
Fermi energy/level	A system's Fermi energy is the smallest possible increase in the ground state energy when exactly one electron is added to the system. The Fermi level is an electron energy level with energy equal to the Fermi energy.
HOMO	Highest Occupied Molecular Orbital.
HREELS	High Resolution Electron Energy Loss Spectroscopy.
k-points	Selected special points in the Brillouin zone where the periodic wave functions are evaluated.
LEED	Low Energy Electron Diffraction.
LUMO	Lowest Unoccupied Molecular Orbital.
MINDO	Modified Intermediate Neglect of Differential Overlap.
Modelling software	A software package that applies code that calculate properties of materials. These include quantum mechanical, semi-empirical and molecular mechanics codes.
PDOS	Partial Density of States (See Density of States).
Periodic slab	A model that represents a crystal surface by a periodic repetition of a surface representing unit cell.
Potential energy surface	A plot of the relative potential energy of a system with regard to the geometry. This may be a surface in a multi-dimensional space. Abbreviated to PES.
Pseudopotential	The pseudopotential is an effective potential that is used to replace the complicated motion effects of the core electrons of an atom and its nucleus. Using this, the Schrödinger equation will contain a modified potential term.
Self-consistent field	In the iterative procedure to calculate the ground state electronic configuration. The procedure is ended when the change in total electronic energy between two iterations is negligible and the electronic field therefore self-consistent.
Semi-empirical	A quantum mechanical method which uses experimental parameters as part of the input.

Spin polarisation	Spin refers to the angular momentum intrinsic to an electron, resulting in a magnetic field. In spin polarized calculations, up and down spin electrons are not degenerate and are calculated separately and could result in a magnetised system.
Surface reconstruction	The change in geometric position of the surface atoms in order to minimise the total energy of the system. Surface reconstruction refers to the movement in the surface plane and surface relaxation refers to movement perpendicular to the surface.
TPD	Temperature Programmed Desorption.
Vacuum space	The separation between surface slabs in a unit cell.
VASP	Vienna Ab initio Simulation Package.
Vibrational analysis	The process of finding the vibrational frequencies of a system. This is done by finding the eigenvalues of a mass weighed force constant matrix.
Wave function	A wavefunction is a function that describes the properties of a wave according to quantum mechanics. They arise as solutions to the Schrödinger equation.
XPS	X-ray Photo-electron Spectroscopy.

Appendix B

Derivation of CO adsorption equilibrium conditions

Since the critical temperature (T_c) and pressure (P_c) of CO is 132.85 K and 34.987 bar respectively [1], we can also consider CO to behave like an ideal gas above $2T_c$ and up to $5P_c$. Typical Fischer-Tropsch conditions fall within this range. In this derivation we consider CO to behave like an ideal gas. We can now construct an equilibrium coverage model for CO in a similar way Faglioni and Goddard [2] did for hydrogen (see Chapter 3). In their work there is a detailed description of their derivation. We apply the same assumptions as those used for hydrogen. In the next sections we will highlight certain steps in the derivation of the CO adsorption equilibrium conditions.

B.1 Gas phase description

For an ideal CO gas the molecular partition function is given by:

$$q_g = V \frac{(2\pi m_{CO} k_B T)^{3/2}}{h^3} \frac{1}{1 - e^{-h\nu/k_B T}} \frac{8\pi^2 I k_B T}{h^2} \quad (\text{B.1})$$

where ν is the vibrational frequency of molecular CO, I is the moment of inertia of CO, m_{CO} is the CO molecular mass, T is the absolute temperature, k_B is the Boltzmann constant and h is the Planck constant. The resulting gas phase chemical potential (μ_g) is given by:

$$\mu_g = -RT \ln(q_g/N_g) \quad (\text{B.2})$$

where R is the ideal gas constant and N_g is the number of CO molecules.

B.2 Adsorbed phase description

To describe the adsorbed CO we adopt a formalism which is similar to that proposed by Faglioni and Goddard [2]. N_a is the number of adsorbed CO molecules; A is the surface area; $\rho = (N_a/A)$ is the surface density; q_a is the molecule partition function for one adsorbed CO molecule; $[N_a]$ equals the moles of adsorbed atoms per unit area; N_s is the number of surface metal atoms; $[N_s]$ is the moles of surface metal atoms per unit area; ν_s is the surface vibrational frequency; θ is the surface CO coverage; θ_M is the maximum possible value of θ ; $E(\theta)$ is the absolute value of 1 mol of the adsorption energy relative to gas phase CO, μ_a is the chemical potential of the adsorbed state and

$$F(\theta) = E(\theta) + \theta \frac{dE(\theta)}{d\theta} \quad (\text{B.3})$$

We also have the adsorbed molecule vibrational partition function (q_ν) and the De Broglie thermal wavelength as

$$q_\nu = \frac{1}{1 - e^{h\nu/k_B T}} \quad (\text{B.4})$$

and

$$\Lambda = h/(2\pi m_{CO} k_B T)^{1/2} \quad (\text{B.5})$$

For the statistical surface description to be meaningful a quantum correction needs to be included. This is done by considering surface gas limits.

Similar to the work by Faglioni and Goddard, the classical limit chemical potential (μ_a^{cl}) and the degenerate surface gas limit chemical potential (μ_a) is respectively given by

$$\mu_a^{cl} = -RT \left(\frac{\delta \ln(Q_a)}{\delta N_a} \right)_{A,T} = RT \ln(\rho \Lambda^2) - E \quad (\text{B.6})$$

and

$$\mu_a = RT \ln(e^{\rho \Lambda^2} - 1) - E \quad (\text{B.7})$$

resulting in a quantum correction of $\mu_a - \mu_a^{cl} = RT \ln\left(\frac{e^{\rho \Lambda^2} - 1}{\rho \Lambda^2}\right)$.

B.2.1 Ideal surface gas model

If we assume a small barrier for surface diffusion, we can consider the adsorbed CO as a 2D ideal surface gas. This model will only be valid in the low CO coverages and high temperature limits. The molecular surface partition function of a surface gas is

$$q_a = A \frac{2\pi m_{CO} k_B T}{h^2} \frac{1}{1 - e^{h\nu/k_B T}} = \frac{A q_\nu}{\Lambda^2} \quad (\text{B.8})$$

The classical chemical potential of this 2D ideal surface gas is accordingly

$$\mu_a^{cl} = RT \ln(\rho \Lambda^2) - E(\theta) - \theta \frac{dE(\theta)}{d\theta} = RT \ln(\rho \Lambda^2) - F(\theta) \quad (\text{B.9})$$

After the quantum correction we find the chemical potential to be

$$\mu_a = RT \ln \left(\frac{e^{\rho \Lambda^2} - 1}{q_\nu} \right) - F(\theta) \quad (\text{B.10})$$

For equilibrium we have $\mu_g = \mu_a$ and after rearrangement we have

$$\frac{N_g}{V} = \left(\frac{q_g}{V} \right) \left(\frac{e^{[N_s] \theta \Lambda^2} - 1}{q_\nu} \right) e^{-F(\theta)/RT} \quad (\text{B.11})$$

Since we assumed that CO is an ideal gas we can write the equilibrium CO pressure as

$$P_{CO}^{ideal} = \frac{k_B T N_g}{V} = k_B T \left(\frac{q_g}{V} \right) \left(\frac{e^{[N_s] \theta \Lambda^2} - 1}{q_\nu} \right) e^{-F(\theta)/RT} \quad (\text{B.12})$$

As can be seen from equation B.12 there is no upper limit to θ in this model. Another restriction is the fact that θ is only valid within the fitting range of θ .

B.2.2 Hard-disk surface gas model

Faglioni and Goddard notes that the ideal surface gas model is not valid near saturation coverage. Since we need to be able to consider highly covered surfaces, we need to take into account saturation coverage effects. The big difference between the model under consideration and the previous model, is that we define a certain fixed area to each adsorbed CO molecule. This results in an adsorbed molecular partition function of

$$q_a = \frac{(A - bN_a)q_\nu}{\Lambda^2} \quad (\text{B.13})$$

with $b = A/(N_s \theta_M)$. We can also consider it as $b\rho = \theta/\theta_M$

In a similar manner as for the ideal surface gas model we calculate the classical limit chemical potential as

$$\mu_a^{cl} = RT \ln \left(\frac{\rho \Lambda^2}{q_\nu} \right) - F(\theta) - RT \ln(1 - \theta/\theta_M) + RT \left(\frac{\theta/\theta_M}{1 - \theta/\theta_M} \right) \quad (\text{B.14})$$

which, after the quantum correction, is

$$\mu_a = RT \ln \left(\frac{e^{\rho \Lambda^2} - 1}{q_\nu} \right) - F(\theta) - RT \ln(1 - \theta/\theta_M) + RT \left(\frac{\theta/\theta_M}{1 - \theta/\theta_M} \right) \quad (\text{B.15})$$

Applying the equilibrium condition ($\mu_g = \mu_a$), we obtained the equilibrium CO gas pressure as

$$P_{CO}^{hard} = \frac{k_B T N_g}{V} = k_B T \left(\frac{q_g}{V} \right) \left(\frac{e^{|N_s| \theta \Lambda^2} - 1}{q_\nu} \right) \left(\frac{e^{\theta / (\theta_M - \theta)}}{1 - \theta / \theta_M} \right) e^{-F(\theta) / RT} \quad (B.16)$$

This equates to the simpler form of

$$P_{CO}^{hard} = P_{CO}^{ideal} \left(\frac{e^{\theta / (\theta_M - \theta)}}{1 - \theta / \theta_M} \right) \quad (B.17)$$

B.2.3 Anchored model

Another limiting case for CO adsorption is when CO can be considered to be anchored to a specific site. On the Fe(100) surface there is one possible hollow site for adsorption per metal atom with an area of $A/N_s \theta_M$. This limit is valid when temperatures are low.

The obtained adsorbed partition function is

$$q_a = \frac{A q_\nu}{N_s \theta_M \Lambda^2} = \frac{\theta q_\nu}{\rho \theta_M \Lambda^2} \quad (B.18)$$

giving a classical limit chemical potential of

$$\mu_a^{cl} = RT \ln \left(\frac{\rho \Lambda^2}{q_\nu} \right) - F(\theta) - RT \ln(1 - \theta / \theta_M) \quad (B.19)$$

and after the quantum correction this is

$$\mu_a = RT \ln \left(\frac{e^{\rho \Lambda^2} - 1}{q_\nu} \right) - F(\theta) - RT \ln(1 - \theta / \theta_M) \quad (B.20)$$

Applying the equilibrium condition ($\mu_g = \mu_a$) we obtain the equilibrium CO gas pressure as

$$P_{CO}^{anch} = \frac{k_B T N_g}{V} = k_B T \left(\frac{q_g}{V} \right) \left(\frac{e^{|N_s| \theta \Lambda^2} - 1}{q_\nu} \right) \left(\frac{1}{1 - \theta / \theta_M} \right) e^{-F(\theta) / RT} \quad (B.21)$$

The simpler form of this is

$$P_{CO}^{anch} = P_{CO}^{ideal} \left(\frac{1}{1 - \theta / \theta_M} \right) \quad (B.22)$$

Bibliography

- [1] Lide, D. R., Kehiaian, H. V., Eds. *CRC Handbook of Thermophysical and Thermochemical Data*; CRC Press: Boca Raton, FL, 1994.
- [2] Faglioni, F.; Goddard III, W. A. *Journal of Chemical Physics* **2005**, *122*, 014704.

Appendix C

Localised Thermodynamics

In this appendix we will discuss the concept of localised thermodynamics. We will show that by using the partial Hessian vibrational analysis (PHVA) we can estimate the thermodynamic properties of surface reactions.

Vibrational energy and entropy contributions to the reaction free energy are some of the most computationally demanding aspects of calculating reaction free energies. The computational expense is incurred by the calculation of the matrix of second energy-derivatives (harmonic force constant matrix/Hessian matrix). After diagonalisation of this matrix the square roots of the resulting eigenvalues yields the harmonically approximated vibrational frequencies. This computation of the Hessian requires a minimum of $6N+1$ energy and gradient evaluations (where N is the number of atoms). The computation of the Hessian can become computationally intractable if the system has too many atoms.

This problem can be overcome if there is only an interest in the chemical reactivity in a localised area of the chemical system. This can be done by constructing and diagonalising the appropriate subblock of the Hessian matrix. This approach is referred to as PHVA. Head et al. [1–5] demonstrated the use of this method for the study of surface chemistry. PHVA can be used in modelling surface adsorbates to determine the type of stable point an adsorbate occupies on the potential energy surface (PES). In this analysis the frequencies of only a part of a chemical system of interest (the adsorbate molecule) is calculated. They suggested that by using the PHVA, entropy and enthalpy corrections to reaction energies can be estimated. This assumption is valid provided that the chemical change is very localised and that there is no significant vibrational coupling between considered and non-considered subsections of the full Hessian matrix. In studying coadsorption (as in chapter 5) and the subsequent surface reactions (seen in Chapter 6), the largest geometric changes are usually those of the adsorbates. This is only a valid approach if surface reconstruction does not take

place. Ciobîcă et al. [6] shows an example of the fact that adsorbate induce surface reconstruction can take place in certain cases. When adsorbate induced surface reconstruction or other possible surface altering effects are not applicable, the geometrical changes of the metal surface are usually small compared to those of the adsorbates.

Applying statistical thermodynamics to the resulting subset of frequencies from a PHVA can give an estimate of the changes in entropy and enthalpy of the reacting system as a function of temperature. An advantage of applying this method is the fact that it provides a way of bridging the 0 K to finite temperature gap that is usually a problem in DFT calculations. This provides us with the ability to predict whether a fundamental surface reaction would take place at the reaction temperature.

Li and Jensen [7] have shown that by using PHVA and the subsequent application of the thermodynamic corrections on a deprotonation reaction they could reproduce the full Hessian values to within 0.4 – 1.6 kJ/mol.

Hirano [8] proposed the following temperature dependent vibrational corrections:

$$H_{vib} = \sum_i \left[\frac{h\nu_i}{2} + \frac{h\nu_i e^{(-h\nu_i/kT)}}{1 - e^{(-h\nu_i/kT)}} \right] \quad (C.1)$$

and

$$S_{vib} = \sum_i \left[\frac{(h\nu_i/kT)e^{(-h\nu_i/kT)}}{1 - e^{(-h\nu_i/kT)}} - \ln(1 - e^{(-h\nu_i/kT)}) \right] \quad (C.2)$$

where h is Planck's constant, ν is the vibrational frequency, k is the Boltzmann constant, and T is the temperature. The first term in H_{vib} is the contribution of the zero-point vibrational energy and the second part is the change of H_{vib} with temperature.

In an ideal gas system the Gibbs free energy is give by:

$$G = E_{ads} + (H_{vib} + H_{trans} + H_{rot}) - T(S_{vib} + S_{trans} + S_{rot} - kT \ln \left(\frac{P}{P_0} \right)) \quad (C.3)$$

When one considers the surface species, the change in rotation and translation partition functions become very small. This differs from the ideal gas where these are the main entropic contributions. With a very small influence on the entropy and enthalpy corrections, the effect of H_{trans} , H_{rot} , S_{trans} and S_{rot} terms become negligible. Since we are only considering the reaction on the surface and not that of the equilibrium with the gas phase, the last term also falls away. The Gibbs free energy for a surface reaction is now simplified to:

$$G \approx E_{ads} + H_{vib} - TS_{vib} \quad (C.4)$$

By calculating this value for the species involved in a surface reaction, the ΔG_r value for the reaction can be estimated.

There are two sources for error in this approximation. There is an inherent numerical error that is related to the convergence of ΔG_r with the calculational parameters. A well converged k-point set and a sufficient size of the plane wave basis set will minimize this error. The second error is due to the choice of functional. This extent of this error is much harder to estimate. Loffreda [9] showed that changing the Functional from PW91 to RPBE can show significant changes in the adsorption energies of various species on gold and platinum.

An important limitation of this model is the fact that configurational entropy is neglected. This contribution can be estimated [10]. For a surface such as Fe(100) this contribution should amount to less than 6 meV/Å² at all temperatures lower than 1000 K.

Loffreda [9] used a similar method as [8], but in stead of explicitly calculating the contribution to H and S he directly calculates the reduced change in entropy from the reduced partition functions. It is therefore easy to calculate ΔG_r for 1 mol directly from the two sets of vibrational frequencies by:

$$Q_{vib} = \prod_i \frac{1}{1 - e^{(-h\nu_i/kT)}} \quad (C.5)$$

$$\Delta S_{vib} = -R \ln \left(\frac{Q_{product}^{vib}}{Q_{reactant}^{vib}} \right) \quad (C.6)$$

$$\Delta G_r \approx \Delta E_r + \Delta E_{ZPE} - T \Delta S_{vib} \quad (C.7)$$

where Q_{vib} is the reduced partition function, R is the molar gas constant, ΔE_r is the change in energy from the DFT results and ΔE_{ZPE} is the change in zero-point vibrational energies.

From the results it is easy to calculate the equilibrium constant K by:

$$K = \left(\frac{Q_{product}^{vib}}{Q_{reactant}^{vib}} \right) e^{\Delta E_r/RT} = e^{\Delta G_r/RT} \quad (C.8)$$

These PHVA and statistical thermodynamic methods can be applied to various surface reactions. An example of this can be seen in our calculation of the heats of mixing for the coadsorbed H and CO on Fe(100) (Chapter 5).

Bibliography

- [1] Jin, S.; Head, J. D. *Surface Science* **1994**, *318*, 204.
- [2] Calvin, M. D.; Head, J. D.; Jin, S. *Surface Science* **1996**, *345*, 161.

- [3] Head, J. D. *International Journal of Quantum Chemistry* **1997**, *65*, 827—838.
- [4] Head, J. D.; Shi, Y. *International Journal of Quantum Chemistry* **1999**, *75*, 815—820.
- [5] Head, J. D. *International Journal of Quantum Chemistry* **2000**, *77*, 350–357.
- [6] Ciobîcă, I. M.; Van Santen, R. A.; Van Berge, P. J.; Van de Loosdrecht, J. *Surface Science* **2008**, *602*, 17–27.
- [7] Li, H.; Jensen, J. H. *Theoretical Chemistry Accounts* **2002**, *107*, 211–219.
- [8] Hirano, T. In *MOPAC Manual*; Stewart, J. J. P., Ed.; Stewart Computational Chemistry, 7 ed., 1993.
- [9] Loffreda, D. *Surface Science* **2006**, *600*, 2103–2112.
- [10] Reuter, K.; Scheffler, M. *Physical Review B* **2003**, *68*, 045407.

Appendix D

Intermediates for CO hydrogenation on Fe(100)

D.1 Introduction

A number of studies, both experimental and theoretical, have been conducted to understand the mechanism of the methanation reaction on a variety of Fischer-Tropsch catalyst surfaces [1–6]. Although methane formation is undesirable during the Fischer-Tropsch synthesis, it is useful to study methane formation pathways to understand the Fischer-Tropsch mechanism.

In this appendix we investigate the intermediates in the formation of methane and methanol from CO and H₂ on the Fe(100) surface by using a spin polarized, periodic DFT approach. We consider the stability of various reaction intermediates which are formed upon the sequential addition of H atoms to the adsorbed CO. This gives rise to partially hydrogenated molecular fragments on the surface. The energetics of these intermediate species are used to construct various H-addition pathway profiles.

D.2 Method and models

D.2.1 Computational method

The quantum chemical calculations were performed using the CASTEP [7] DFT code, utilising a plane wave basis set and the pseudopotentials included in the CASTEP suite [8]. The RPBE functional [9] was used to calculate the electron-electron interactions. A Gaussian smearing method was applied to the electron distribution at the Fermi level with $\sigma = 0.1$ eV.

A $p(2 \times 2)$ seven-layer slab was used to represent the Fe(100) surface. An optimised

10 Å vacuum spacing was used and adsorption was performed on both sides of the slab. The k-point sampling was generated by following the Monkhorst-Pack [10] procedure with a $5 \times 5 \times 1$ mesh. The cutoff energy was set at 400.0 eV. The coordinates of all atoms were fully optimized. All of the setup parameters were optimised.

D.2.2 Method of sequential H addition

Generally a pathway similar to the initiation section of the 'alkyl'-mechanism of the Fischer-Tropsch synthesis (see section 1.1.1.1) is considered when the formation of methane is studied. In this mechanism the CO dissociates to form coadsorbed C and O. Both of these can be subsequently hydrogenated via a Langmuir-Hinshelwood type mechanism: O to form H_2O and C to form the CH_x species necessary for the formation of methane or higher hydrocarbons. We expand this mechanism by assuming that the CO does not necessarily dissociate, but that the adsorbed CO can also be directly hydrogenated.

We calculated the adsorption structures of the surface species that result from the sequential addition of H to both the C and the O atoms of the adsorbed CO. To simplify the model we only considered the addition of H to the tilted CO in the four-fold hollow site. This can be done since this geometry is the only local minimum at $\theta_{CO} = 0.25$ ML [3]. The titled CO is also the most stable geometry at both $\theta_{CO} = 0.25$ ML and $\theta_{CO} = 0.5$ ML. To include the effect of coverage, the addition of H to CO was considered on one CO per unit cell surface at initial CO coverages of $\theta_{CO} = 0.25$ ML and $\theta_{CO} = 0.5$ ML. The reported adsorption and formation energies are relative to H_2 and CO in the gas phase. For $\theta_{CO} = 0.25$ ML the formation energy is calculated by:

$$E_{form} = \frac{E_{(CO+nH)} - E_{slab}}{2} - 1/2nE_{H_2} - E_{CO} \quad (D.1)$$

and for $\theta_{CO} = 0.5$ ML the formation energy is calculated by:

$$E_{form} = \frac{E_{(CO+nH)} - E_{slab}}{2} - 1/2nE_{H_2} - E_{CO} - E_{ads,CO} \quad (D.2)$$

where E_{form} is the energy of formation of the species relative to the gas molecules, $E_{(CO+nH)}$ is the calculated energy of the specific adsorbed species, E_{slab} is the calculated energy of the clean Fe(100) slab, E_{H_2} and E_{CO} is the calculated energies of the gas phase species H_2 and CO, and n is the number of H atoms in the specific adsorbate under consideration. $E_{ads,CO}$ is the heat of adsorption of a CO molecule at $\theta_{CO} = 0.5$ ML. This term is subtracted at $\theta_{CO} = 0.5$ ML, because the addition of H to CO is only considered on one of the two CO molecules per $p(2 \times 2)$ surface. The energy of

formation values presented in here do not include zero-point energy corrections.

D.2.3 Graphical Representation

In this appendix adsorbate structures will be represented graphically by a space-filling model viewed along the surface normal (unless otherwise indicated). To avoid confusion the following colours are used to identify various atoms : Fe = purple, C = grey, O = red and H = white.

D.3 Results

The separate adsorption energies of H and CO at various surface coverages have been considered in Chapter 3.

D.3.1 Sequential addition of H to CO

We have calculated the optimised geometries and energies of formation for the various products resulting from the sequential addition of H to the adsorbed CO. The results can be seen in Figure D.1. The reference value used for comparison of the various species is CO and H₂ in the gas phase. At $\theta_{CO} = 0.5$ ML the sequential addition of H proceeds only on one of the CO molecules per surface per unit cell.

If we consider the whole of Figure D.1 at a first glance, it is clear that all the considered optimised structures are stable with regard to the gas phase. There are also multiple possible pathways to arrive at CH₄ by the addition of H to the adsorbed CO. A possible pathway toward the formation of CH₃OH is also visible. It is clear that, for most of the structures, there are no real significant difference in stability of the adsorbed species at $\theta_{CO} = 0.5$ ML and $\theta_{CO} = 0.25$ ML. The small differences that occur can be ascribed to the sizes of the adsorbed species. For the smaller adsorbates, like -C (*J*) and -CH (*K*), the $\theta_{CO} = 0.5$ ML structures are the most stable. The larger adsorbates, like -CH₃ (*M*) and -OCH₃ (*D*), are more favoured at $\theta_{CO} = 0.25$ ML, because the surface is less crowded, having only one adsorbate for every four hollow sites.

Structure *G* is an exception, since the structures at $\theta_{CO} = 0.5$ and 0.25 ML differ significantly. At $\theta_{CO} = 0.5$ ML structure *G* is still intact, but during optimisation of the structure at $\theta = 0.25$ ML the OH group detached and moved to a bridge position leaving a -CH₂ group behind (shown in Figure D.1 *G*). This dissociation of this structure after addition of H is not observed at $\theta_{CO} = 0.5$ ML due to the fact that there is another CO molecule located next to the bridge site, restricting the detachment of the

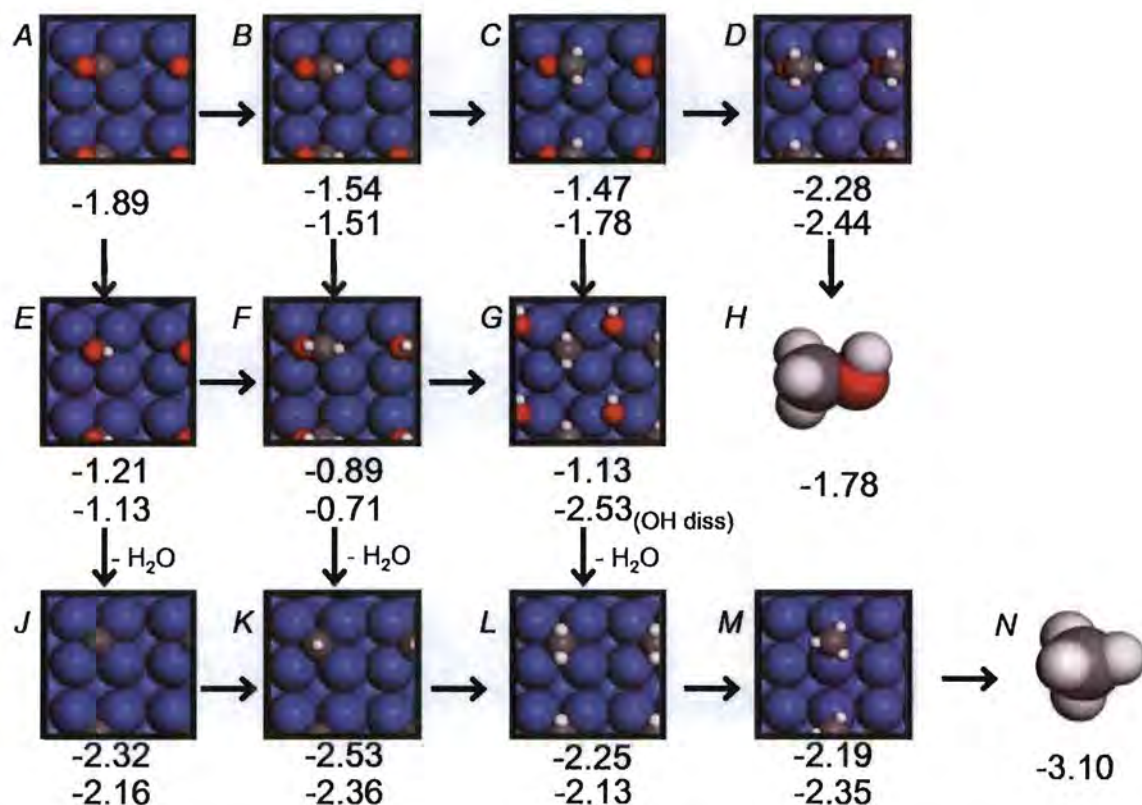


Figure D.1: Formation energies (in eV) for species formed by sequential addition of H. Most structures have two energy values: Upper - $\theta_{CO} = 0.5$ ML. Lower - $\theta_{CO} = 0.25$ ML. Arrows indicate an addition of H: Right - Addition to C; Down - Addition to O (Graphical representation is of the structures at $\theta_{CO} = 0.25$ ML).

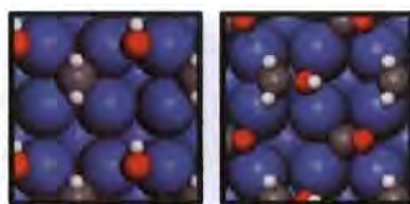


Figure D.2: Comparison of structure *G* at $\theta_{CO} = 0.25$ ML (left) and $\theta_{CO} = 0.5$ ML (right).

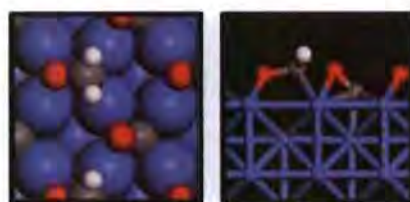


Figure D.3: Top view (left) and side view (right) of the structure of *C* at $\theta_{CO} = 0.5$ ML. Ball and stick model (right) used for clarity.

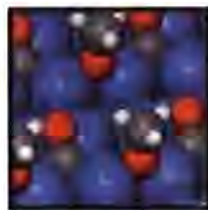


Figure D.4: The structure of the adsorbed methoxy group at an initial $\theta_{CO} = 0.5$ ML. (Point of view tilted away from the surface normal.)

OH fragment. This dissociation of the OH group at $\theta_{CO} = 0.25$ ML gives rise to a stability difference of 1.4 eV with regard to $\theta_{CO} = 0.5$ ML. At $\theta_{CO} = 0.5$ ML the CO bond is highly activated with a bond length of 1.490 Å (0.182 Å longer than pure adsorbed CO). The two structures for *G* at $\theta_{CO} = 0.5$ and 0.25 ML can be seen in Figure D.2.

After addition of an H atom to the adsorbed CO (*A*), two structures (*B* and *E*) can be obtained. Structure *B* corresponds to the structure that Blyholder and Lawless [11] proposed for hydrogen assisted CO dissociation (see Chapter 6). Structure *E* resulted in a structure where there is a -OH group dangling from the surface carbon. The addition of the H atom to the C of the CO adsorbate results in a more favourable intermediate than the addition of H to the O atom by 0.38 eV and 0.33 eV for the $\theta_{CO} = 0.25$ ML and 0.5 ML coverages respectively. The addition of an H atom to the C of the CO would be the preferred path. By having the OH group in *E* tilted away from the surface, the O atom could only have a limited interaction with additional H atoms on the surface.

The addition of another H to the C atom in *B* gives rise to structure *C*. In this structure the C atom is pulled out of the hollow site and the CO bond is now almost parallel to the surface plane (Figure D.3). There is a difference of 0.31 eV in the energies of structure *C* at $\theta_{CO} = 0.5$ and 0.25 ML. This could be due to the large size of the CH₂O group. The H atoms on the C atom are not in line with the CO bond any more and the C atom is nearly fully exposed above the surface and not hidden away in the hollow site any more. The most stable species would be at $\theta_{CO} = 0.25$ ML where this bulky adsorbate experiences less sterical hindrance.

After a further addition of an H atom on the C atom of structure *C* an interesting structure is found (*D*) which can be seen in Figure D.4. It is a methoxy group adsorbed on a bridge site. The -CH₃ end of the methoxy group tilts away from the surface and the C atom has no interaction with the surface any more. This methoxy adsorbate is quite stable compared to the adsorbed pure CO (*A*). If another H should attach to the O atom in structure *D*, CH₃OH (*H*) can be formed and dissociated from the surface. This addition and desorption is in total a highly endothermic reaction.

The addition of an H atom to either *B* or *E* gives rise to structure *F*. The structures

of F at both $\theta_{CO} = 0.25$ ML and $\theta_{CO} = 0.5$ ML are the least stable of all the considered adsorbed geometries compared to the gas phase molecules. When going from B to F at $\theta_{CO} = 0.25$ and 0.5 ML the changes in energy are 0.80 eV and 0.65 eV respectively. Although F is still more stable than gas phase CO and H₂ at both the considered coverages, it is highly unlikely that these structures would form due to their relative instability compared to the other adsorbed species. This seems to disfavour the ‘enol’ mechanism on Fe(100) (see section 1.1.1.4), since in this mechanism F corresponds to one of the proposed active chain growth intermediates.

When an H atom is added to the O atom in structure E the resulting system spontaneously dissociates a water molecule upon optimisation, giving rise to a C atom adsorbed on the surface (structure J). As expected, structure J is quite stable at both $\theta_{CO} = 0.5$ and 0.25 ML coverages. Following the pathway $A \rightarrow E \rightarrow J$ it can be seen that the O atom has been removed from the CO, forming a water molecule and a surface carbon. If the O in structure J can be hydrogenated, this pathway can be viewed as another alternative to the generally regarded CO dissociation pathway.

In a similar manner water is spontaneously removed upon optimisation after the addition of an H atom to structures F and G . The resulting structures are K and L respectively. At a $\theta_{CO} = 0.25$ ML coverage the step from G to L might be quite easy since the OH group has already dissociated, needing only another H atom to form the adsorbed water molecule.

D.4 Pathways for CO hydrogenation

Considering the profile in Figure D.1, we see a diverse range of possible reaction intermediates. Using these energy values, along with the adsorption energies of H (four-fold hollow site), we can construct H-balanced thermodynamic reaction profiles for the intermediates in various catalytic reaction pathways. This is done by adding the calculated heat of adsorption per H atom to the various steps under consideration to give the correct molar balance for the considered reaction pathway. This addition corresponds to an idealised, infinitely separated coadsorption and therefore coadsorption effects are not included. Following this procedure we constructed a number of energy profiles for the formation of CH₄ and CH₃OH.

D.4.1 ‘Alkyl-type’ methanation mechanism

The sequential addition of H atoms to form methane by following the path $J \rightarrow K \rightarrow L \rightarrow M \rightarrow N$ is part of the initiation steps of the well known ‘alkyl’ mechanism

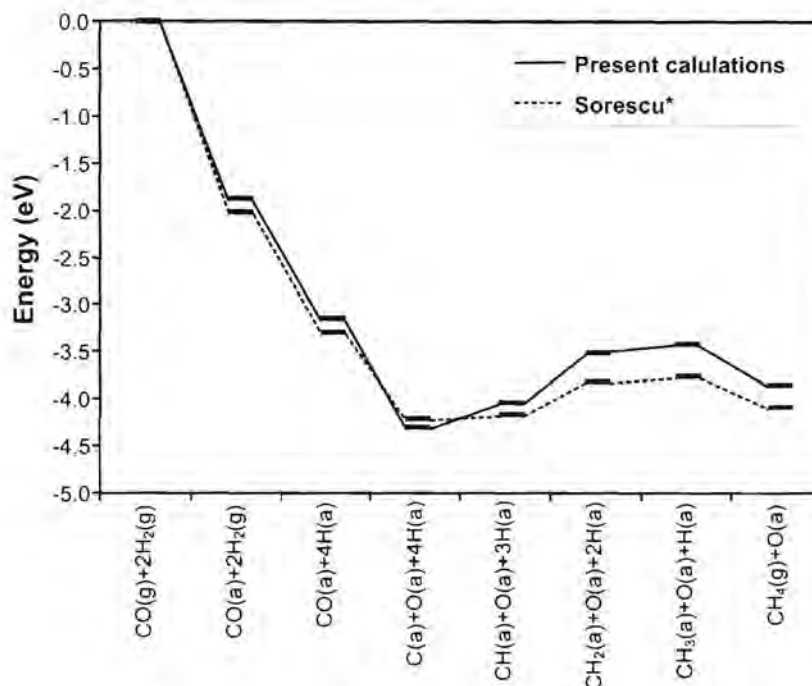


Figure D.5: Comparison of the energy values of intermediates in the 'alkyl' mechanism for CH₄ formation at an initial $\theta_{CO} = 0.25$ ML in the present work to literature values (*Sorescu [5]). In all cases O remains on the surface.

(see section 1.1.1.1). The comparison of the energies of the intermediates at $\theta_{CO} = 0.25$ ML in this 'alkyl-type' mechanism to the values calculated by Sorescu [5] can be seen in Figure D.5. Here we included the energies we calculated at an initial $\theta_{CO} = 0.25$ ML for the products of CO dissociation (see Chapter 6), which is similar to those described by Bromfield et al. [3]. In the calculations by Sorescu [5], the O atom was not removed from the surface as a water molecule. We adapted our profile to be able to draw a comparison to it. In Figure D.5 the sum of the energies for the isolated slab and of that of CO and 2H₂ molecules in gas phase were taken as the reference. It is clear that the trends for the pathways in Figure D.5 are similar. The main differences are introduced by the use of different exchange-correlation functionals to describe the electron-electron interactions (which can significantly change on the adsorption energy of adsorbates [12, 13]). In this study the RPBE functional is used, while Sorescu [5] used the PW91 functional. In both cases it is clear that the adsorption of CO and H, as well as the dissociation of CO are exo-energetic processes. In both energy profiles C(a)+O(a)+4H(a) correspond to the most stable configuration in the pathway. Although the rest of the profiles are mostly similar, the energy change we calculated for the second hydrogenation step (CH(a)+H(a) → CH₂(a)) is much larger than the corresponding step in Sorescu's work. In general it can be concluded that our calculations give similar results with regard to the trends in an 'alkyl-type' mechanism.

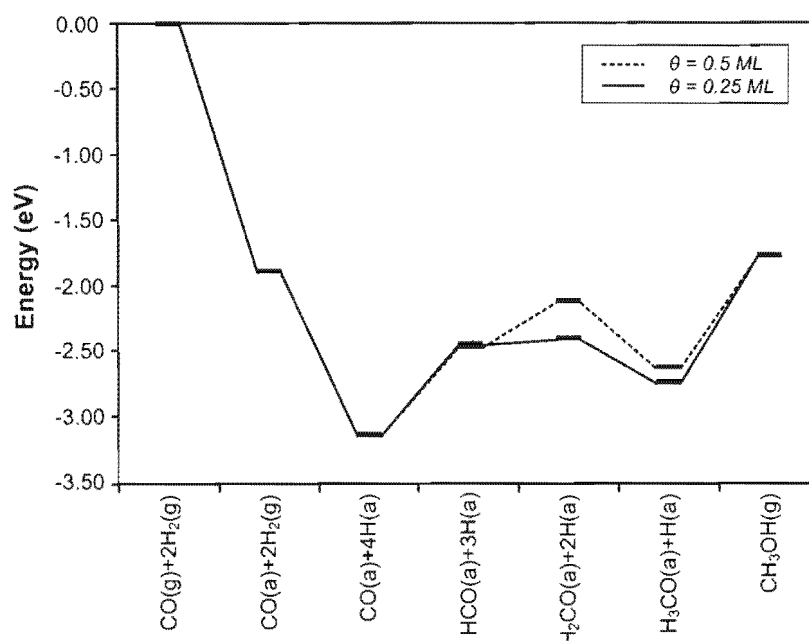


Figure D.6: Energy values of the intermediates in the CH₃OH formation pathway.

D.4.2 Pathway for CH₃OH formation

The sequential addition of H atoms to form methanol (CH₃OH) can be constructed by following the intermediates $A \rightarrow B \rightarrow C \rightarrow D \rightarrow H$. The energetic profiles for this pathway at both $\theta_{CO} = 0.25 \text{ ML}$ and $\theta_{CO} = 0.5 \text{ ML}$ can be seen in Figure D.6. After the adsorption of both CO and atomic H, the CO can be endothermically hydrogenated to 'HCO'. Up to this point the effect of coverage is limited. In the following endothermic step (H₂CO(a)+2H) the coverage destabilises the intermediate at $\theta_{CO} = 0.5 \text{ ML}$ somewhat compared to $\theta_{CO} = 0.25 \text{ ML}$. The following hydrogenation step is exothermic and results in the relatively stable methoxy species. The last hydrogenation and subsequent desorption of CH₃OH is almost 1 eV exothermic. When considering the pathways in this process at these two coverages it is clear that only the (H₂CO(a)+2H) intermediate differs significantly. If this process can take place it would probably be favoured at $\theta_{CO} = 0.25 \text{ ML}$. The last large endothermic step results in the CH₃OH molecule, which is thermodynamically significantly less stable than CH₄.

D.4.3 Lowest energy pathway for direct hydrogenation to CH₄

The lowest energy pathway to form methane by the sequential addition of H atoms, without the dissociation of CO, can be constructed by following the intermediates $A \rightarrow B \rightarrow C \rightarrow G \rightarrow L \rightarrow M \rightarrow N$. The resulting profiles can be seen in Figure D.7, while a comparison of this pathway to that of the pure CO dissociation pathway at $\theta_{CO} = 0.25 \text{ ML}$ can be seen in Figure D.8. This lowest energy direct hydrogenation

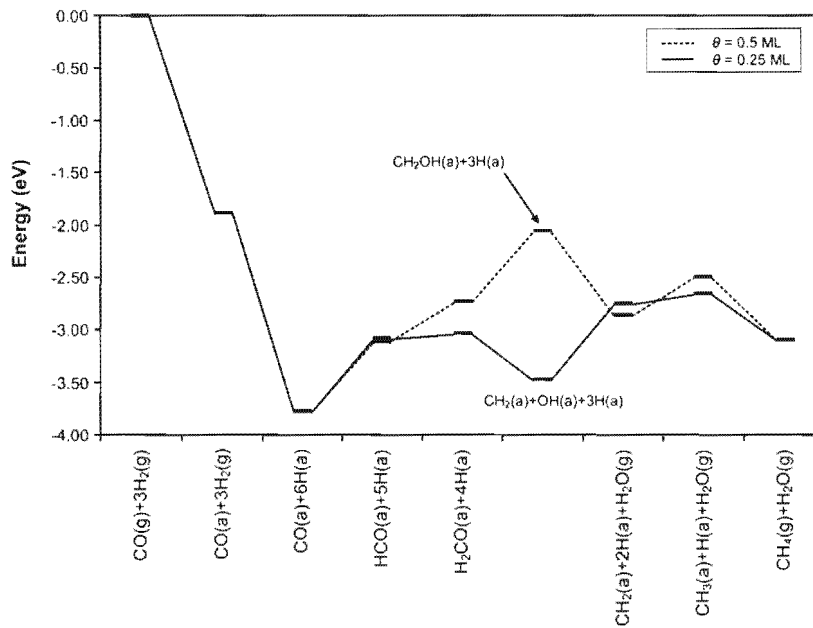


Figure D.7: Comparison of the lowest energy direct hydrogenation pathways at an initial $\theta_{CO} = 0.25$ ML and $\theta_{CO} = 0.5$ ML. Oxygen is removed as gas phase water.

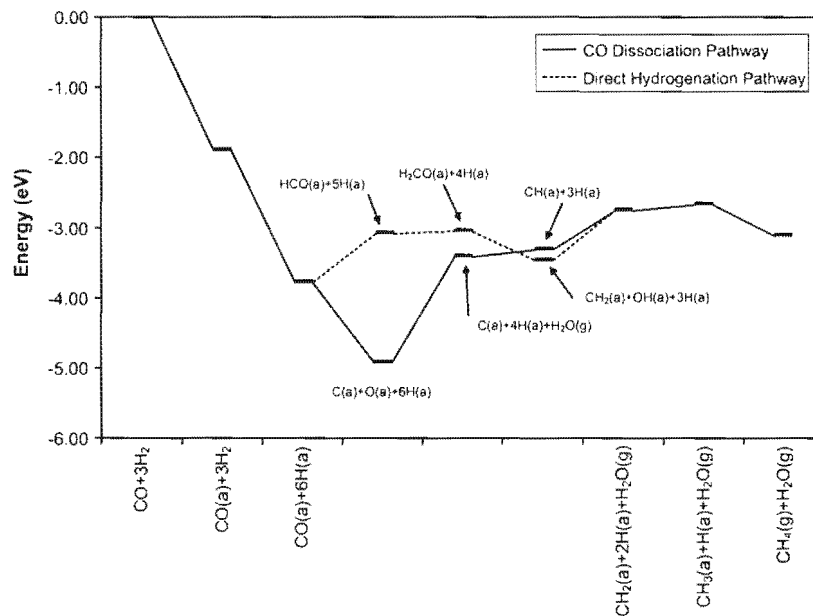


Figure D.8: Comparison of the direct CO dissociation pathway to the lowest energy direct hydrogenation pathways at an initial $\theta_{CO} = 0.25$ ML.

pathway could be considered as describing the initiation steps of the 'CO-insertion' mechanism described in section 1.1.1.3. It is clear that the initial CO coverage plays a large role in these pathways. The big difference in the pathways at the two coverages lies at intermediates that are created after the fifth step. At $\theta_{CO} = 0.25$ ML this step is exothermic, while at $\theta_{CO} = 0.5$ ML this step is strongly endothermic. The expected initial CO coverage at the relevant Fischer-Tropsch temperatures and pressures is $\theta_{CO} \approx 0.5$ ML (see Chapter 3). The resulting intermediate at $\theta_{CO} = 0.5$ ML has an energy that is 1.69 eV higher than the purely adsorbed CO and H. This value is at least 0.4 eV larger than the calculated CO dissociation barrier (see Chapter 6, indicating that the CO dissociation mechanism is favoured at this coverage and that the formation of methane via this mechanism is not likely. At $\theta_{CO} = 0.25$ ML the corresponding intermediate is quite stable, resulting in the coadsorption of CH₂ and OH. After removal of the OH as gas phase water the rest of the pathway corresponds to the steps of the 'alkyl-type' mechanism.

If we consider the comparison of this pathway to that of the pure CO dissociation pathway at $\theta_{CO} = 0.25$ ML we see that these pathways differ significantly until both coincide at structure *L*. The big difference lies in the endothermic formation of 'HCO' compared to the exothermic direct dissociation of CO. For the direct hydrogenation pathway to be followed (as well as the CH₃OH formation pathway), the 'HCO' intermediate has to be hydrogenated. It has to be kept in mind that the 'HCO' intermediate was shown to be able to dissociate with a barrier of 0.71 eV to form coadsorbed CH + O, which might be more favourable than the further hydrogenation pathway. Considering the fact that both adsorbed CO and 'HCO' can dissociate to form more stable products, whereas the hydrogenation of the 'HCO' results in an almost iso-energetic structure we do not expect the further hydrogenation pathway to be able to significantly contribute to the methanation reaction on Fe(100).

D.5 Conclusions

We have calculated the structures and energies of the direct hydrogenation products of CO on Fe(100) at initial CO coverages of $\theta_{CO} = 0.25$ ML and $\theta_{CO} = 0.5$ ML.

We constructed a number of H balanced methanation pathway energy profiles. From these profiles presented above it is clear that the CO dissociation pathway may not be the only accessible pathway in the methanation reaction. The sequential addition of hydrogen atoms may lead to an alternative pathway of producing the relevant species that are necessary for chain growth according to various Fischer-Tropsch mechanisms. In our opinion these results (although no reaction transition state bar-

riers have been calculated) seem to thermodynamically favour the Fischer-Tropsch mechanisms in which the CO is somehow dissociated. This is due to the fact that many of the partially hydrogenated CO structures are significantly less stable than both the CO and HCO dissociation products. Although these pathway profiles show that the alternative pathways are possible, further studies on the reaction barriers and the subsequent analysis of the kinetics are needed to be able to fully compare these pathways.

Bibliography

- [1] Nayak, S. K.; Noolijen, M.; Bernasek, S. L.; Blaha, P. *The Journal of Physical Chemistry B* **2001**, *105*, 164–172.
- [2] Sorescu, D. C.; Thompson, D. L.; Hurley, M. M.; Chabalowski, C. F. *Physical Review B* **2002**, *66*, 035416/1–035416/13.
- [3] Bromfield, T. C.; Curulla Ferré, D.; Niemantsverdriet, J. W. *ChemPhysChem* **2005**, *6*, 254–260.
- [4] Jiang, D. E.; Carter, E. A. *Physical Review B* **2005**, *71*, 045402.
- [5] Sorescu, D. C. *Physical Review B* **2006**, *73*, 155420.
- [6] Ciobica, I. M. *The Molecular Basis of the Fischer-Tropsch Reaction* PhD thesis, Technische Universiteit Eindhoven, Eindhoven, **2002**.
- [7] Segall, M. D.; Lindan, P. J. D.; Probert, M. J.; Pickard, C. J.; Hasnip, P. J.; Clark, S. J.; Payne, M. C. *Journal of Physics: Condensed Matter* **2002**, *14*, 2717–2744.
- [8] *MS Modeling 4*; Accelrys Software Inc., <http://www.accelrys.com>.
- [9] Hammer, B.; Hansen, L. B.; Nørskov, J. K. *Physical Review B* **1999**, *59*(11), 7413–7421.
- [10] Monkhorst, H. J.; Pack, J. D. *Physical Review B* **1976**, *13*(12), 5188–5192.
- [11] Blyholder, G.; Lawless, M. *Langmuir* **1991**, *7*, 140–141.
- [12] Jiang, D. E.; Carter, E. A. *Surface Science* **2003**, *547*, 85–98.
- [13] Sorescu, D. C. *Catalysis Today* **2005**, *105*, 44–65.

List of Publications

1. Rousseau, M.; Oosthuizen, S.; van Helden, P.; van Sittert, C.G.C.E.; Vosloo, H.C.M., "Molekuulmodellering van die metatiese van alkene met Ru-karbeenkomplekse." *SA Tydskrif vir Natuurwetenskap en Tegnologie*, **2005**, 24 pp. 34-36.
2. Jordaan, M.; van Helden, P.; van Sittert, C.G.C.E.; Vosloo, H.C.M. "Experimental and DFT investigation of the 1-octene metathesis reaction mechanism with the Grubbs 1 precatalyst." *Journal of Molecular Catalysis A*, **2006**, 254 pp. 145-154.
3. Swart, J.C.W.; Van Helden, P.; Van Steen, E. "Surface energy estimation of catalytically relevant fcc transition metals using DFT calculations on nano-rods." *The Journal of Physical Chemistry C.*, **2007**, 111, pp. 4998-5005.
4. Van Helden, P.; Van Steen, E. "Die ko-adsorpsie van H en CO op 'n model-ysteroppervlak." *SA Tydskrif vir Natuurwetenskap en Tegnologie*, **2008**, 27 pp. 163-164.
5. Van Helden, P.; Van Steen, E. "Coadsorption of CO and H on Fe(100)." *The Journal of Physical Chemistry C.*, **2008**, 112, pp. 16505-16513.
6. Van Helden, P.; Van Santen, R. A.; Van Steen, E. "Nanorod calculations on bcc iron: A method for estimation of size-dependent surface energies of metal nanocrystals." *The Journal of Physical Chemistry C.*, in press.

University of Cape Town

Acknowledgements

*Thou art my master, and my author thou,
Thou art alone the one from whom I took
The beautiful style that has done honour to me.*

— DANTE ALIGHIERI, THE DIVINE COMEDY: INFERNO,
CANTO I

On the long journey towards writing this thesis, many people crossed my path who had a profound influence on the development of my ideas, and who had made the journey a joyous experience. Although this list is not at all exhaustive, it gives me great pleasure to specially thank a few specific people.

I would like to start off by expressing my immense thanks and love to my travel mate and wife, Maureen, who has been the inspiration at my side the whole journey. *Te amo.*

To my parents, Maarten and Phia, I would like to give thanks for sowing the seeds, and nurturing my love of nature and knowledge. I would also like to thank them for all their efforts in starting me off on this wondrous journey.

I would like to express my profound thanks to my promoter, prof. Eric van Steen. I am grateful for all the long and intriguing discussions and the invaluable criticism of my work. He gave me the freedom to explore a wide range of topics (including some very odd ideas), whilst always carefully guiding me to make wise decisions. His knowledge of the field of Fischer-Tropsch, his patience and creative ideas has been immensely helpful, as well as being a strong motivational force throughout my studies.

I am furthermore thankful towards all the other teachers who gave me good directions on this journey. In this regard I would like to specially thank prof. Manie Vosloo for introducing me to the field of computational chemistry. Another very special word of thanks goes to prof. Carols Reinecke for his wisdom and guidance in my early studies. I am immensely grateful for all the advice and the opportunities he created for me.

My heartfelt thanks goes to prof. Rutger van Santen for giving me the opportunity to work in his group in Eindhoven. His wide knowledge and insights was truly inspiring and I am grateful for our successful collaboration. Staying in Eindhoven was a wonderful experience and in this regard I would also like to thank Ionel and Sorinella Ciobîcă, as well as Calum en Sheila MacLeod. My wife and I will always remember their warm hospitality and we cherish their friendship.

To dr. Tracy Bromfield I owe a debt of gratitude for giving me the opportunity to be involved with the SASOL HTFT Modelling study team and for being a great mentor. I would also like to thank the members of this team, dr. Werner Janse van Rensburg, dr. Petrie Steynberg, dr. Melissa Peterson, prof. Hans Niemandsverdriet and dr. Ionel Ciobîcă for the fruitful and interesting discussions we had. To dr. Jan van den Berg I am deeply grateful for all the the in-depth discussions, as well as for his immense help in setting up the partial vibrational analysis code for CASTEP.

To all my fellow students at PU for CHE, UCT, en TU/e a word of thanks: you made my journey a fun-filled, enriching experience. These include Gavin Deas, Gerbrand Breed, James Brown, Carl Preiß, Tjaart van der Walt and many others who helped me hone my unwanted procrastination skills with enticing sports, such as office cricket or pre-exam-midnight-chess. To Karl Meissner-Rollof I would like to express my thanks for being such a dear friend through all of these years. A special mention goes to Jurie Swart, my fellow UCT modeller. All the great discussions (both scientific and not), along with his calm criticism and dry humour was always greatly appreciated.

I would also like to thank Andries en Alet Louw for their friendship and all the interesting hikes on Table Mountain during the time I stayed with them in Oranjezicht in Cape Town.

A lot of computational power was needed to be able to do my research. I am very thankful for all the efforts of Alvin Chang and Graham Inggs in maintaining our computational resources and for putting up with all my requests.

These acknowledgements would be incomplete without mentioning the financial support of SASOL who funded my work from the very beginning.

And finally, in the words of the Apostle (Romans 11:33–36):

*O altitudo divitiarum sapientiae et scientiae Dei
quam inconprehensibilia sunt iudicia eius et investigabiles viae eius
Quis enim cognovit sensum Domini aut quis consiliarius eius fuit
Aut quis prior dedit illi et retribuetur ei
Quoniam ex ipso et per ipsum et in ipso omnia ipsi gloria in saecula
Amen.*

– Pieter van Helden

Curriculum Vitae

Pieter van Helden was born on the 30th of January 1982 in Johannesburg, South Africa. After finishing his schooling at Hoërskool Centurion in 2000, he attended the School for Chemistry and Biochemistry at the Potchefstroom University for Christian Higher Education (PU for CHE). He completed his B.Sc. degree in 2003. At this stage he was appointed as a lecturer in Philosophy of Science from 2003-2004 at this university. He subsequently attended the B.Sc.(Hons.) program at the North-West University (previously PU for CHE). He graduated *cum laude* with a project thesis titled "*A computational study on the ligand effects in olefin cross metathesis.*" In 2005 he moved to Cape Town where he started his masters study at the Department of Chemical Engineering at the University of Cape Town. Early in 2006 the project was upgraded to Ph.D. status. His Ph.D. thesis is titled: "*Initial steps of the Fischer-Tropsch synthesis on Fe(100): The role of hydrogen.*" He received various awards including the CATSA silver medal (2004), the MERCK Medal (2004) and SASOL Postgraduate Scholarship (2005), and he has various publications in international journals.

